Department of Physics and Astronomy

University of Heidelberg

Master thesis

in Physics

submitted by

Simon Johannes Angstenberger

born in Ellwangen an der Jagst

2021

Design of a setup for flexible, dispersion-compensated nonlinear femtosecond laser pulse compression adapted to an extreme ultraviolet frequency comb

This Master thesis has been carried out by

Simon Johannes Angstenberger

at the

Max-Planck-Institut für Kernphysik

under the supervision of

apl. Prof. Dr. José R. Crespo López-Urrutia

Entwurf eines Aufbaus zur flexiblen dispersionskompensierten nichtlinearen Kompression von Femtosekunden-Laserpulsen an einem ultravioletten Frequenzkamm

Die vorliegende Arbeit präsentiert einen konzeptionell neuen Ansatz für nichtlineare Pulskompression in einer Multipasszelle für einen Frequenzkamm im ultravioletten Spektralbereich, der zukünftig für Quantenlogik-Spektroskopie an hochgeladenen Ionen verwendet werden wird. Dabei wird die Dispersion nicht wie herkömmlich durch dispersive Spiegel kompensiert. Stattdessen wird mit einem im Spektralbereich des Lasersystems um 1030 nm anomal dispersiven Kaliumdiphosphat-Kristall als nichtlinearem Material die Dispersionskompensation durch Einstellen des umgebenden Gasdrucks im Multipass-Aufbau ermöglicht. Dadurch kann die Pulskompression durch Anzahl der Durchgänge durch die Zelle angepasst werden. Das vorliegende Konzept wird durch numerische Simulationen der nichtlinearen und dispersiven Phänomene validiert.

Zur Quantifizierung der Pulskompression befasst sich diese Arbeit im Weiteren mit dem Aufbau eines Systems zur Pulscharakterisiung durch intensitätsbasierte und interferometrische Autokorrelation sowie frequency-resolved optical gating.

Design of a setup for flexible, dispersion-compensated nonlinear femtosecond laser-pulse compression adapted to an extreme ultraviolet frequency comb

This work presents a novel approach for nonlinear pulse compression in a multipass cell for an extreme ultraviolet frequency comb which will be employed for quantum logic spectroscopy of highly charged ions. The nonlinear crystal used is potassium pyrophosphate (KDP) which exhibits anomalous dispersion around the central wavelength 1030 nm of the seed laser. This enables tuning of the dispersion by adjusting the pressure of a normal dispersive gas which fills the multipass cell. Chirped mirrors are thus not necessary and pulse compression becomes flexible by adjusting the number of passes in the cell. This proposal is supported by numerical simulations.

For analysis of the pulse compression, a pulse characterization system for intensity-based and interferometric autocorrelation and frequency-resolved optical gating is set up.

Contents

1 Introduction

This chapter motivates the bigger picture of the overall experimental setup under which the work of this thesis was performed. The open question of variation of fundamental constants is introduced and a method of probing these variations using highly charged ions (HCI) and a frequency comb in the extreme ultraviolet (XUV) is presented. This motivates the goal of this thesis, an improvement of the XUV frequency comb by pulse compression and spectral broadening.

1.1 Variation of Fundamental Constants

The standard model of particle physics is a theory that describes the strong, weak and electromagnetic interaction between matter with astonishing accuracy [1]. However, the standard model falls short of an explanation for the existence of dark matter and the matter-antimatter asymmetry. It has also not yet been unified with general relativity [2], yielding a theory that connects the four fundamental forces. Thus, the standard model is subject to intense research.

Extensions to the standard model with a variation in space and time of the fundamental constant that describes the coupling between photons and charged particles, the fine structure constant α, are motivated by the high dimensionalities of string theories [3]. The fine structure constant can be expressed via vacuum permittivity ϵ_0, elementary charge e, the Planck constant $\hbar$ and the speed of light c as

$$\alpha = \frac{1}{4\pi\epsilon_0}\frac{e^2}{\hbar c}. \tag{1.1}$$

Searching for variations in this constant over time could support this approach of varying fundamental constants in space or time. A first experimental piece of evidence of a dynamical fine structure constant was brought up by measurements with the Very Large Telescope suggesting a change of α in the redshifted spectra of distant quasars [4].

The abundance of the fine structure constant in atomic physics formulae hints that a fruitful measurement environment on α-variations lies within atomic spectroscopy. The influence of an α-variation on the hydrogen-like energy levels $E_{n,j}$ of a single electron bound to an point-like nucleus with infinite mass with principle quantum numbers n and j in the Dirac theory is given by

$$E(\alpha) = E_0 + q\left(\left(\frac{\alpha}{\alpha_0}\right)^2 - 1\right). \tag{1.2}$$

The current, constant value of the fine structure constant is α_0 and q is a parametrization for the energy level [5]. This can be connected to a variation in the transition frequency $f = \Delta E/\hbar$ between two energy levels with an energy difference ΔE as

$$\frac{\dot{f}}{f_0} = \frac{2q}{f_0}\frac{\dot{\alpha}}{\alpha_0} = K\frac{\dot{\alpha}}{\alpha_0}, \tag{1.3}$$

where $K = 2q/f_0$ is a dimensionless sensitivity factor mainly depending on the relativistic contributions in each of the two involved energy levels. Hence, the variation of α can be detected by a measurement of frequency variations of two frequencies with differing K without knowledge of the absolute value.
At presence, the upper limit of an α-variation is given by [6]

$$\frac{\dot{\alpha}}{\alpha_0} = (-2.0 \pm 2.0) \cdot 10^{-17}\mathrm{yr}^{-1}. \tag{1.4}$$

Fig.1.1 shows the increased accuracy of precise frequency measurements over time. The implementation of optical clocks has surpassed the accuracy of traditional Caesium clocks in the last decade [8]. With the increased accuracy, this provides a feasible approach to test α on temporal variations.

1.2 Highly Charged Ions

A suitable choice for spectroscopy to improve the limits on possible alpha variations are HCIs, i.e. ions that have been stripped of many of their valence electrons, as their sensitivity to an α-variation scales according to [9]

$$K \propto 2\alpha^2 Z^2 (Q+1)^2, \tag{1.5}$$

with the ionization charge Q. Furthermore, the high binding energy of the remaining electrons in the ion makes HCIs less sensitive to external perturbations such as the earth

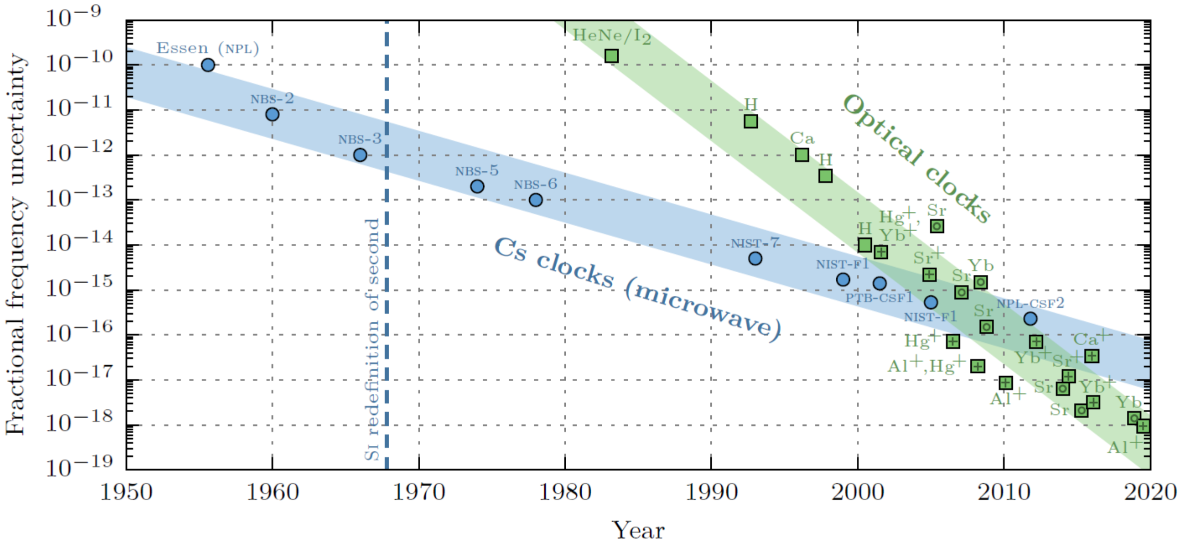

Figure 1.1: Advance of precision spectroscopy. The accuracy of optical clocks has recently surpassed the accuracy of Cesium clocks. Taken from [7].

magnetic field. Minimization of these external perturbations is crucial for experiments with unprecedented accuracy [9].

These ions can be produced in an electron beam ion trap (EBIT) [10]. As the electron temperature in an EBIT is very high, the ions need to be cooled. This is achieved by sympathetic cooling in a cryogenic Paul trap where the ions are trapped together with beryllium ions. The ions are laser-cooled and by thermalization, the HCIs can be employed for precision spectroscopy [11, 12].

With a coherent light source, quantum logic spectroscopy is possible with HCIs by reading out the co-trapped ion's state [13]. This might also enable quantum computing with long coherence times of the qubits as the HCIs are insensitive to external perturbations. A missing link is the availability of coherent light sources with linewidths that give access to the strongly forbidden, very narrow transitions of HCIs in the XUV.

1.3 XUV Frequency Combs

A laser is such a coherent light source, demonstrated for the first time in 1960 [14–16]. It has a wide range of technical applications [17]. A special kind of laser is the *frequency comb* which has a fixed phase relation between emitted laser pulses [18, 19]. Special locking electronics guarantee this phase relation, which might else smear out due to noise. Thus, the frequencies of this laser have a comb-like discrete spacing. The lines

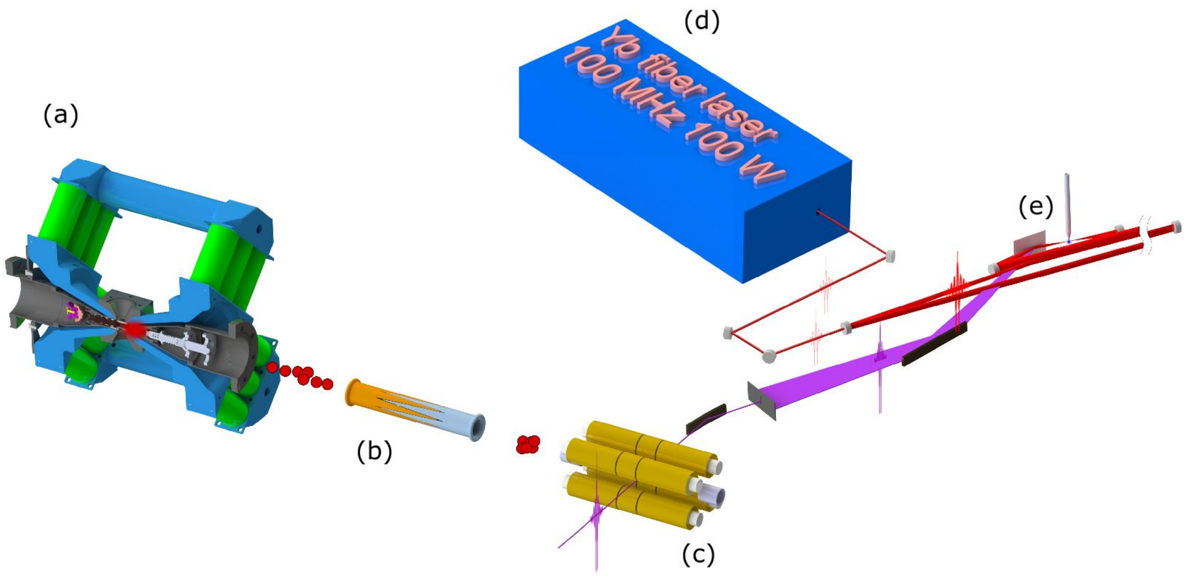

Figure 1.2: Planned overall experimental setup. (a) The HCI are produced in an EBIT, (b) slowed down and injected (c) in a linear Paul trap. (d) The fiber frequency comb which (e) is coupled into an enhancement cavity for XUV generation. These XUV pulses are sent to the Paul trap. Figure from [25].

are separated by the repetition rate f_{rep} with an offset f_{CEO}. The n-th frequency is then given by

$$f_n = f_{\text{CEO}} + n f_{\text{rep}}, \tag{1.6}$$

allowing to operate the laser as a "frequency ruler" reference for hihg precision spectroscopic studies.

However, the frequency range of this system is limited by the availability of lasing sources and their respective wavelength ranges. A frequency comb in the XUV for coherent spectroscopy on HCIs is not readily available. Tuning to the XUV needs frequency conversion by high-harmonic generation (HHG) [20]. This phenomenon generates light at odd multiple integers of the original frequency when shining intense light onto a gas target. This allows transferring the comb structure to the XUV, shown in 2005 for the first time [21] with rapid improvements to date [22–24].

This first experiment of XUV spectroscopy on HCIs is currently being set up at the Max-Planck-Institut für Kernphysik. An overview of the planned experimental setup is given in Fig. 1.2. The HCIs are produced in a compact EBIT and injected into a Paul trap where they are cooled and stored. An XUV frequency comb with a repetition rate of 100 MHz was set up for spectroscopy of these ions [25, 26]. Laser pulses in the near infrared (nIR) from a commercial fiber laser are amplified and compressed in a home-built laser system . Subsequently, the pulses are sent into a passive enhancement cavity in vacuum, which allows further resonant amplification of the pulses as the roundtrip time in the cavity is matched to the repetition rate of the incoming pulses. Eventually, focusing of the enhanced pulses on a gas target generates the desired high coherence XUV light.

The characterization and improvement of the seeding nIR laser pulses are subject to this thesis. To improve the understanding of the interactions in the enhancement cavity used for XUV generation, different pulse characterization systems are set up and evaluated. High intensities in the XUV are neccessary to drive the strongly forbidden transitions of HCIs in the XUV.

The efficiency of high harmonic generation can be estimated with the Keldysh parameter γ_k [27]. It scales inversely proportional to the square root of the peak laser intensity I_{peak} that generates the harmonics as

$$\gamma_k \propto \frac{1}{\sqrt{I_{\text{peak}}}}. \tag{1.7}$$

A lower Keldysh parameter allows higher efficiency of the process. In addition, the cutoff energy E_{cutoff} that determines the highest frequency producible in the high harmonic process also increases with I_{peak}.

The average power of the fiber frequency comb is already amplified from 10 W to over 80 W and dispersion-compensated in a home-built system; peak powers are further increased in the passive enhancement cavities. It is therefore the second objective of this work to compress the laser pulses from the infrared frequency comb and in this manner increasing the laser peak intensity. Furthermore, shorter pulses increase the HHG efficiency as less cycles of the electric field ionize the gas prior to the strongest oscillation cycles. As dispersion is nearly compensated in a grating compressor, further temporal compression can only be obtained by broader spectra. For this, a novel design of a flexible continuously dispersion-compensated multipass cell for spectral broadening and nonlinear pulse compression is presented. Multipass cells operating with bulk material for pulse compression have recently been set up [28–31] and the presented concept expands the concept with greater flexibility.

Nonlinear pulse compression is based on spectral broadening by nonlinear interactions between the laser pulses and a material. The broader spectra can, on top of shorter pulses, also be employed in an additional application of the frequency comb. A second enhancement cavity is seeded by the same fiber frequency comb. It is in use for velocity map imaging (VMI) [32, 33]. A prospect research topic is the spectroscopy on the thorium isomer ^{229}Th at the seventh harmonic of the XUV frequency comb [34–36]. As the transition region is not known accurately, a broader spectrum allows more flexibility in reaching this transition.

After some theoretical groundwork in Chapter 2, this thesis will present the pulse characterization system in Chapter 3 and a novel design for pulse compression and spectral broadening in Chapter 4, concluding with a summary of the presented work in Chapter 5.

2 Theoretical Background

This chapter will introduce the reader to the theoretical concepts that describe ultrashort laser pulses. As the underlying light source of the work described in this thesis is a frequency comb, the distinct features of pulsed laser light will be covered in more detail. A particular focus will be put on the interaction of laser pulses with matter, such as dispersion and nonlinear optics. With this groundwork at hand, we can then explore the concepts of nonlinear pulse compression. An overview over different compression schemes will be given. Furthermore, the last chapter will introduce the ABCD matrix formalism and the propagation of Gaussian beams for the geometric design of the pulse compression multipass cell.

2.1 Ultrashort Laser Pulses

Light follows Maxwell's equations for classical electrodynamics [37]. This introduction starts from the curl equation for the electric field $\vec{E}$ which reads

$$\vec{\nabla} \times \vec{E} = -\frac{\partial \vec{B}}{\partial t}, \tag{2.1}$$

with a magnetic field $\vec{B}$. Assuming no free currents ($\vec{j} = 0$), one can take the curl on both sides and plug in the curl equation for the magnetic field

$$\vec{\nabla} \times \vec{B} = \frac{1}{c^2}\frac{\partial \vec{E}}{\partial t}, \tag{2.2}$$

with $c = 299792458\,\mathrm{m\,s^{-1}}$ [38] as the speed of light in vacuum as a fundamental constant. Using vector identities, assuming no free charges ($q = 0$) and using the Maxwell equation

$$\vec{\nabla} \cdot \vec{E} = 0, \tag{2.3}$$

one can deduce the *wave equation* for an electric field in vacuum and charge-free space as $\vec{E}$

$$\nabla^2 \vec{E} - \frac{1}{c^2} \partial_t^2 \vec{E} = 0. \tag{2.4}$$

From here, the description is adapted from Diels and Rudolph [39]. A solution of this differential equation is the *plane wave*

$$\vec{E}(\vec{x}, t) = \vec{E_0} \exp\left(i\left(\vec{k} \cdot \vec{x} - \omega t\right)\right), \tag{2.5}$$

which will for simplicity and without loss of generality, be restricted to one dimension z along which the wave propagates. The wave equation then reads

$$E(z, t) = E_0 \exp(i(kz - \omega t)), \tag{2.6}$$

restricting the field to linearly polarized light with an amplitude of E_0. Wave number k and angular frequency ω are related by the photonic dispersion relation

$$k = \frac{\omega}{c}. \tag{2.7}$$

Such a monochromatic wave with a single frequency can, up to a certain linewidth Δk [15], be achieved by a continuous-wave laser in single-frequency operation. This small spectral bandwidth, i.e. the high coherence of the laser as a light source, is attained through stimulated emission and a gain bandwidth that is smaller than the spacing between the resonator modes of the system [40]. Stimulated emission describes an incoming photon that triggers emission of a photon with the same phase, direction and frequency in the gain medium of the laser [14]. As opposed to a monochromatic continuous-wave laser, a description of the emitted light by means of a single frequency is not sufficient for pulsed lasers: Multiple frequency components around a central frequency given by the resonator condition in the laser system contribute to the overall electric field as shown in the top rows of Fig. 2.1. These different propagating frequencies can obey a fixed phase relation, which is called mode-locking. Mode-locking can be achieved via an intensity-dependent component, e.g. a semiconductor saturable absorption mirror (SESAM) [41] or nonlinear polarization rotation [42].

The bottom row in Fig. 2.1 shows the electric field arising from a sum of different underlying frequencies. Some of the contained frequencies are shown above the pulse as an example and all the different frequency components form a wavepacket which is

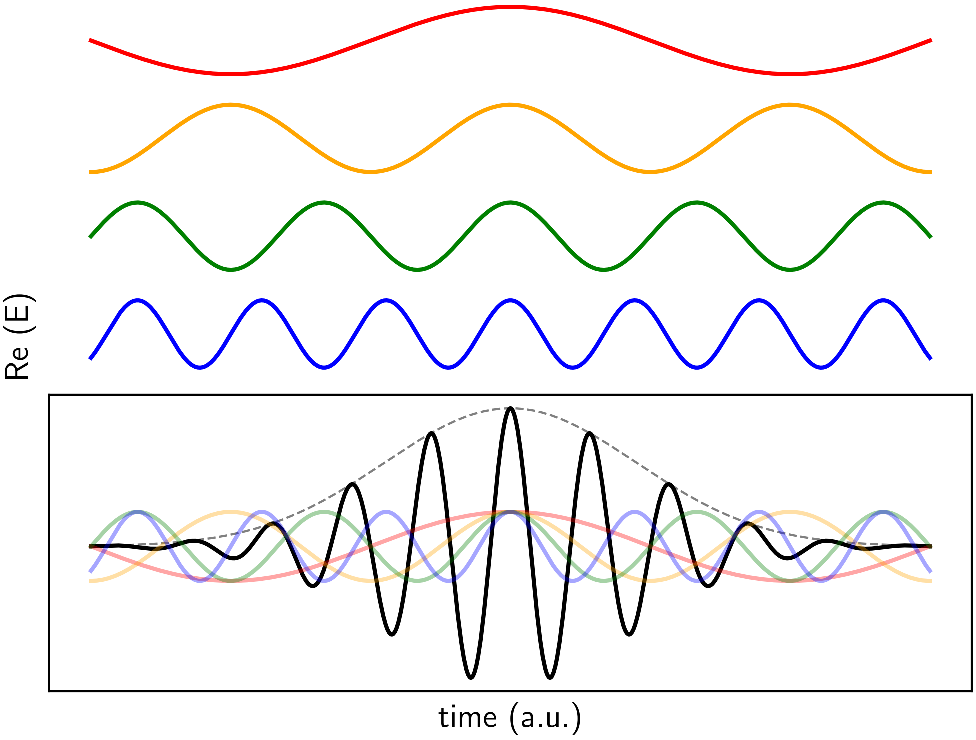

Figure 2.1: Schematic representation of mode-locking. Plane waves of different frequencies, exemplified in red–yellow–green–blue, forming a wave packet with the sum of the real part of the electric field in black. The envelope (dashed) has a stable Gaussian form when a mode-locked laser yields a fixed phase relation of the individual frequencies.

called a pulse. A description of this pulse now needs integration over all the contributing frequencies ω. The contributing frequencies are considered with respect to a central frequency ω_0 and the overall electric field is then

$$E(z,t) = \frac{1}{2\pi}\int_{-\infty}^{\infty} A(\omega-\omega_0)\exp(ikz)\exp(-i\omega t)d\omega, \tag{2.8}$$

where the amplitude $A(\omega)$ of each frequency is considered individually. Time domain and frequency domain are connected by means of the Fourier transform $\mathscr{F}$. The electric field in the frequency domain is then given by

$$\tilde{E}(z,\omega) = \mathscr{F}(E(z,t)) = A(\omega-\omega_0)\exp(ikz). \tag{2.9}$$

2.2 Frequency Combs

In a mode-locked laser, pulses are emitted at a certain repetition rate f_{rep} which is given by the roundtrip time T_{rep} of a resonator system. For a fiber laser, it is predominantly determined by the fiber length in the seed laser. The resulting pulse train is shown in Fig. 2.2(a) in the time domain. The repetition rate is indicated in green as time between two pulse envelopes (dashed green line). The electric field in this plot is shown in red. Specific for a frequency comb is the fixed phase relation between pulses. In Fig. 2.2(a) it is $\Delta\varphi_{\mathrm{CE}} = 2\pi/3$, experimentally administered by special locking electronics [43].

Until now, we focused on the Fourier transform of an individual pulses and their spectra. For a pulse train of N pulses with central frequency ω_c and fixed phase difference $\Delta\varphi_{\mathrm{CE}}$ between individual pulses, the electric field is summed over all n pulses as

$$E_{\mathrm{train}}(t) = \sum_n A\left(t-nT_{\mathrm{rep}}\right)\exp\left(i(\omega_c t - n\omega_c T_{\mathrm{rep}} + n\Delta\varphi_{\mathrm{CE}})\right). \tag{2.10}$$

The electric field in the frequency domain can be calculated via a Fourier transform as

$$\tilde{E}_{\mathrm{train}}(\omega) = \sum_n \exp\Big(n\big(\Delta\varphi_{\mathrm{CE}} - \omega_c T_{\mathrm{rep}}\big)\Big)\int_{-\infty}^{\infty}\mathrm{d}tA(t-nT_{\mathrm{rep}})\exp\big(-i(\omega-\omega_c)t\big). \tag{2.11}$$

By integration and using trigonometric identities and applying that a Fourier transform

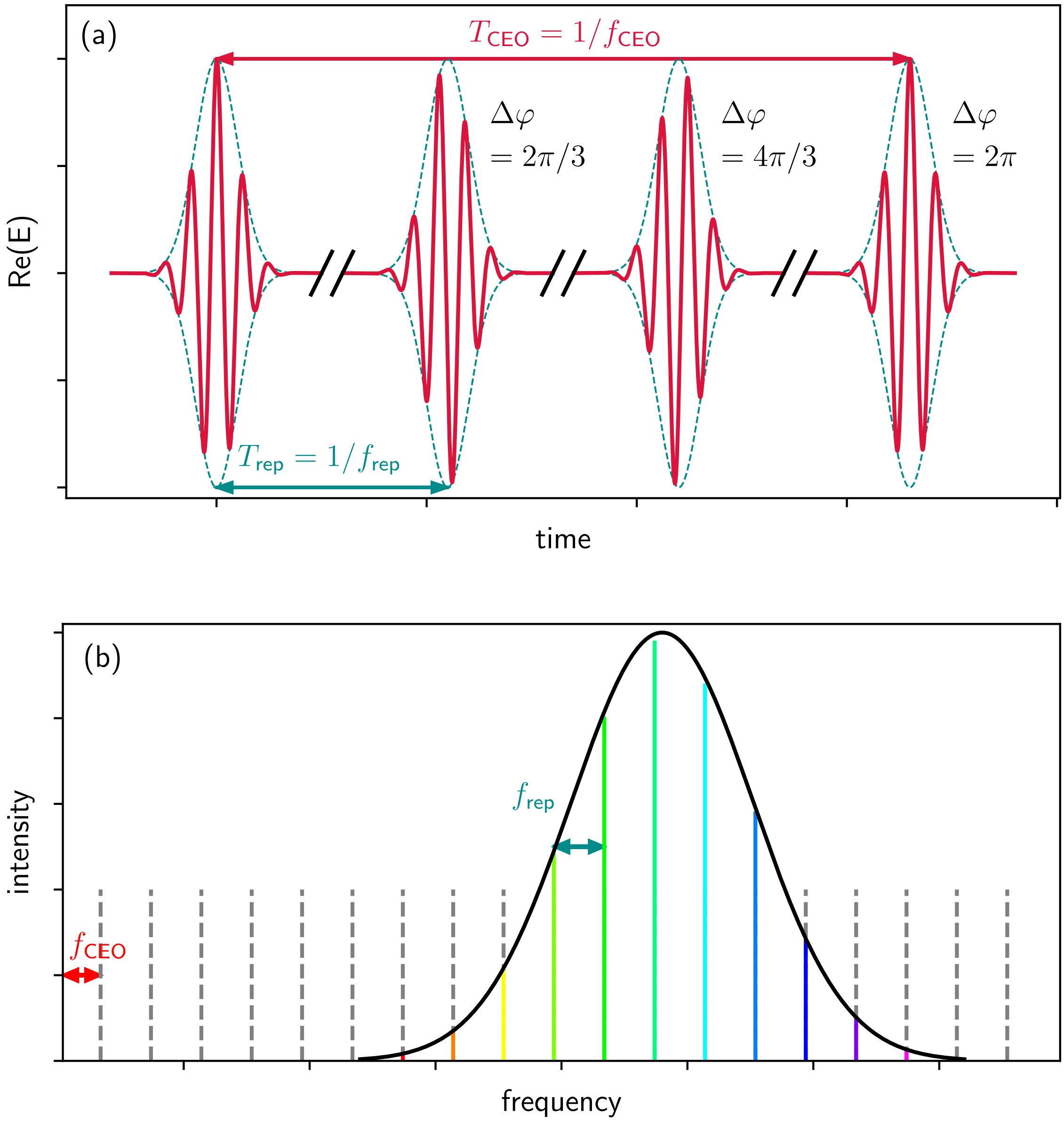

Figure 2.2: (a) Real part of the electric field (red) of a pulse train with repetition time T_{rep} emitted by a frequency comb with fixed phase relation $\Delta\varphi$ between pulses. (b) Schematic spectrum of such a frequency comb with discrete frequencies. Their spacing is determined by the repetition rate f_{rep}, the offset from zero by the carrier-envelope offset f_{CEO}. Only the frequencies contained in the individual pulse spectrum are realized.

of a Dirac distribution yields a constant [25], this expression simplifies for N pulses to

$$\tilde{E}_{\text{train}}(\omega) = \tilde{A}(\omega - \omega_c) \sum_{n=0}^{N} \delta\big(\omega T_{\text{rep}} + \Delta\phi_{\text{CE}} - 2N\pi\big). \tag{2.12}$$

This spectral distribution is plotted in Fig. 2.2(b) for $\lim\limits_{N\to\infty} \big(\tilde{E}_{\text{train}}(\omega)\big)$ where it resembles a comb-like structure: The contained frequencies lie at discrete points and form sharp lines. The fixed phase difference between pulses corresponds to an offset from zero in the Fourier-transformed frequency spectrum, the carrier-envelope offset f_{CEO}. It can be calculated by

$$f_{\text{CEO}} = \frac{\Delta\varphi_{\text{CE}}}{2\pi T_{\text{rep}}}. \tag{2.13}$$

The repetition rate corresponds to the distance between the discrete frequency lines $f_{\text{rep}} = T_{\text{rep}}^{-1}$. Thus, the n-th frequency on the grid is given by

$$f_n = f_{\text{CEO}} + n f_{\text{rep}}; \quad n \in \mathbb{N}. \tag{2.14}$$

The comb frequencies have an envelope given by the determined by the spectrum of a single pulse of the laser, indicated in the plot as colored lines on the grey frequency grid.

2.3 Dispersion

A nifty description of the bulky expression in (2.8) splits the wave-packet into an envelope $A(\omega)$ and an oscillating part $\exp(i\omega_0 t)$. This so-called *slowly varying envelope approximation* is valid for pulses with small spectral bandwidths compared to the central frequency ω_0. In other words, the maximal amplitude in the time domain, limited by the envelope, varies slowly from one to the next optical cycle. Expanding the wavenumber k as well yields

$$E(z,t) = A(z,t)\exp\big(i(k_0 z - \omega_0 t)\big), \tag{2.15}$$

and the description in frequency space is again given by a Fourier transform—the envelope is then denoted by $\tilde{A}(\omega)$. A widely used approximation of the pulse shape is the *Gaussian*.

It is given by

$$A(t) = E_0 \exp(-\frac{2\ln 2}{\tau^2}t^2) \tag{2.16}$$

in the time domain when centered around 0, where τ characterizes the full width at half maximum (FWHM) of the intensity envelope $I(t) = |E(t)|^2$. As the Fourier transform of a Gaussian pulse is still a Gaussian, the expression in the frequency domain reads

$$\tilde{A}(\omega - \omega_0) = E_0\tau\sqrt{\frac{\pi}{2\ln 2}} \exp\left(- \frac{\tau^2(\omega-\omega_0)^2}{8\ln 2}\right). \tag{2.17}$$

Such a Gaussian pulse is shown in Fig. 2.3.

In the following, intensity and phase are explained. They are constantly used for a compact description of pulses throughout this thesis. The intensity is given by

$$I(t) = |E(t)|^2. \tag{2.18}$$

This corresponds to the blue envelope in Fig. 2.3(a). For an ideal pulse, the electric field has a constant phase

$$\varphi(t) = \arg(E(t)) = \arctan\left(\frac{\mathrm{Im}\big(E(t)\big)}{\mathrm{Re}\big(E(t)\big)}\right) = \omega t. \tag{2.19}$$

Although there is an increasing part ωt, this phase is called constant because this part of the phase is just a shift in time. Therefore, it is usually subtracted in pulse descriptions—this gives the constant phase shown by the brown line in Fig. 2.3(b). Reconstructing this in a measurement is difficult and can be done e.g. by means of frequency-resolved optical gating (FROG) and will be explained in more detail in Section 2.6.

Intensity and phase are also used for describing the pulse in the frequency domain, as depicted by Fig. 2.3(c). Resolving the intensity of each wavelength contained in the pulse individually with a spectrometer gives the spectral intensity

$$\tilde{I}(\omega) = |\tilde{A}(\omega)|^2, \tag{2.20}$$

which is then called a *spectrum* and shown in Fig. 2.3(c). As this is the Fourier transform of the complex electric field in the time domain, the electric field $\tilde{E}(\omega)$ is also complex

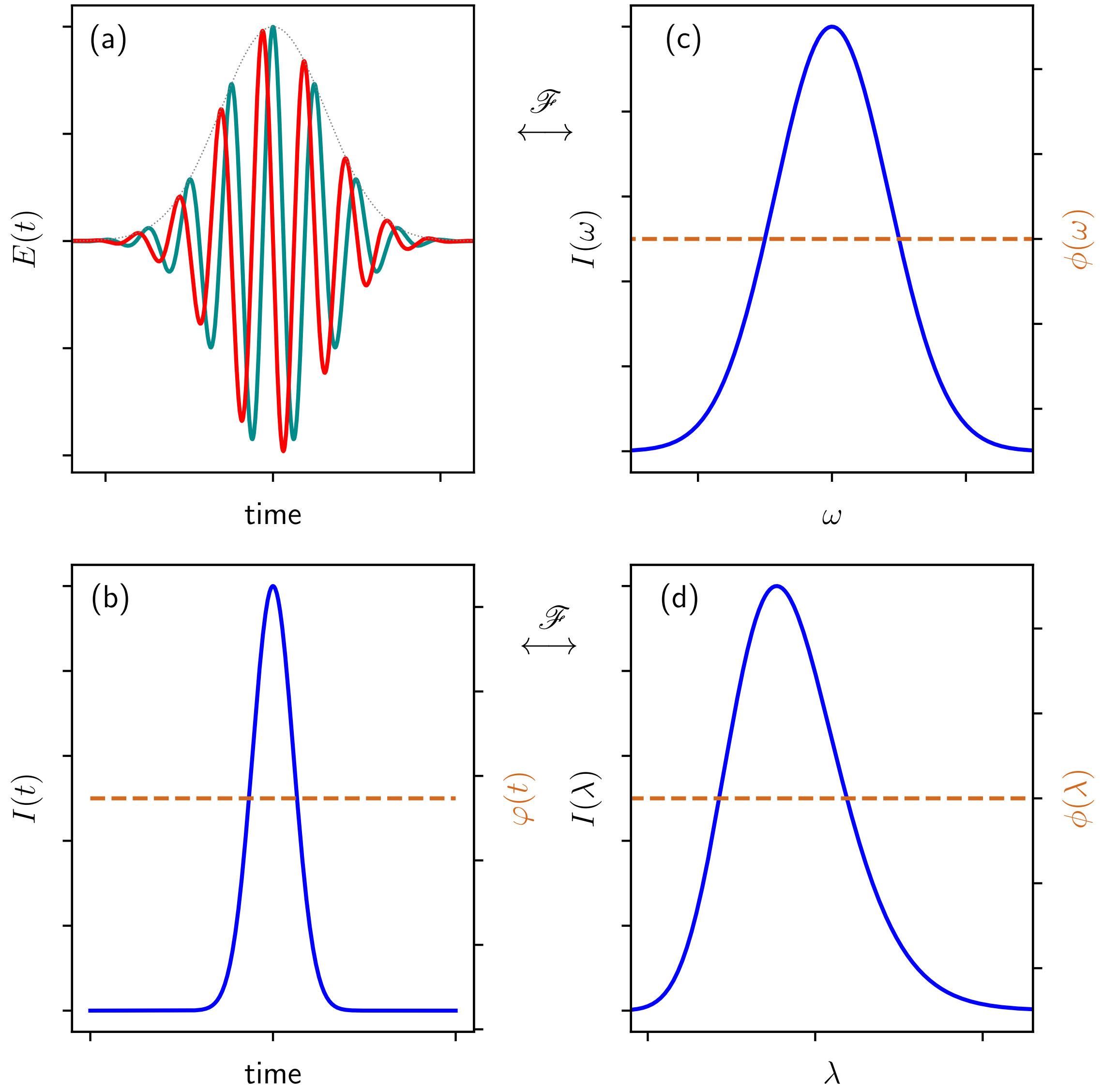

Figure 2.3: (a) A transform-limited Gaussian pulse in the time domain with real (red) and imaginary (green) part of the electric field. (b) The equivalent depiction of this pulse in the time domain via intensity (blue) and phase (brown). (c) The spectrum (blue) of such a pulse in the frequency domain and the spectral phase (brown). (d) The same spectrum and phase plotted against the wavelength. Note that the low number of cycles shown here for better visibility does hardly justify the slowly varying envelope approximation.

and therefore has a spectral phase

$$\phi(\omega) = \arg\left(\tilde{E}(\omega)\right) = \arctan\left(\frac{\mathrm{Im}\big(\tilde{E}(\omega)\big)}{\mathrm{Re}\big(\tilde{E}(\omega)\big)}\right). \tag{2.21}$$

Note that usually the temporal phase is written as φ whereas the spectral phase is denoted by ϕ. However, what is actually measured in the lab is the intensity as a function of the wavelength $\lambda = 2\pi c/\omega$. The inverse relation between frequency and wavelength can lead to misinterpretation of the spectrum for broadband spectra. In Fig. 2.3(d), the plotted spectrum is not a Gaussian— however, it describes the very same spectrum as in Fig. 2.3(c), just on an inverted abscissa.

There is a limit for the product of spectral bandwidth Δf and temporal width τ, namely the time-bandwidth product for Gaussian pulses [39]

$$\tau \cdot \Delta f \geq 0.441. \tag{2.22}$$

A pulse with a given spectral bandwidth can only be as short as this limit dictates. Then, the phase of such a *transform-limited* pulse (neglecting ωt) is constant as shown in Fig. 2.3.

Longer pulses are possible and commonly observed in ultrashort laser pulses. In Fig. 2.4, the frequency of the electric field varies over time. This change in frequency is called a *chirp*—in analogy to the bird sound where the frequency also changes over time. Therefore, the description of the pulse needs the incorporation of the instantaneous frequency $\omega_i(t)$, centering it around the frequency ω_0 for the transform-limited pulse as

$$\omega_i = \omega_0 + \frac{d\varphi}{dt}. \tag{2.23}$$

When the frequency of the pulse increases over time as seen in Fig. 2.4(a), it is called up-chirped. For decreasing frequency instead, it is called down-chirped as seen in Fig. 2.4(c). The colours of the plot illustrate the higher and lower frequencies as they would appear in the visible spectrum: Red light has a higher wavelength and lower frequency than blue light.

Starting from (2.23), it is becoming clear that varying ω_i yields a frequency-dependent

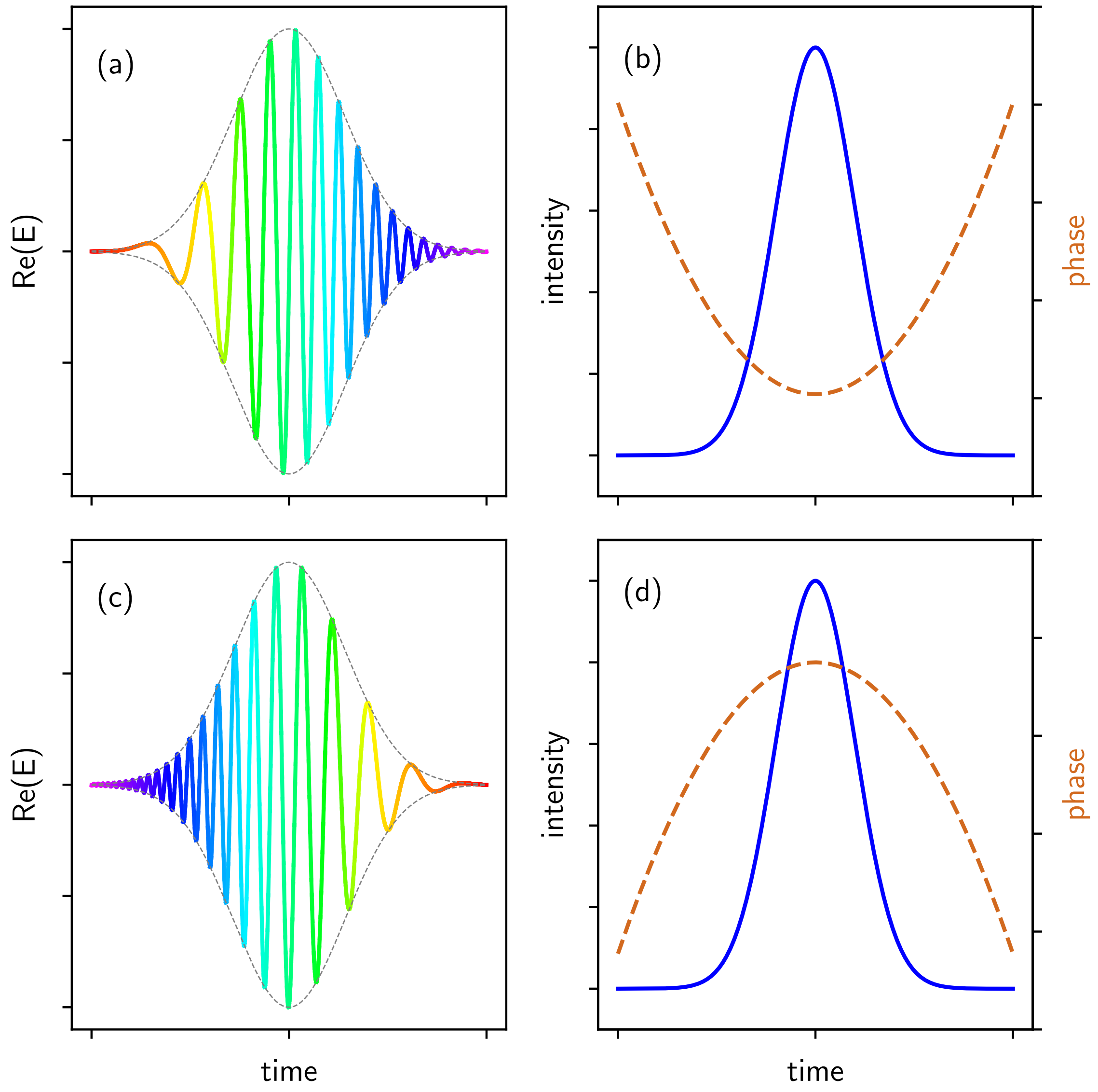

Figure 2.4: (a) The electric field of an up-chirped ultrashort laser pulse in the time domain and (b) its representation via intensity (blue) and phase (brown). (c) Electric field of a down-chirped pulse and (d) its intensity and phase. The rainbow colors illustrate the respective instantaneous frequencies ω_i in the visible spectrum.

phase in the spectral domain. Taylor-expanding ϕ as

$$\begin{aligned}\phi(\omega) &= \phi_0 + \frac{d\phi}{d\omega}(\omega-\omega_0) + \frac{1}{2}\frac{d^2\phi}{d\omega^2}(\omega-\omega_0)^2 + \frac{1}{6}\frac{d^3\phi}{d\omega^3}(\omega-\omega_0)^3 + \mathcal{O}(\omega^4) \\ &= \phi_0 + \phi_1(\omega-\omega_0) + \mathrm{GDD}\cdot(\omega-\omega_0)^2 + \mathrm{TOD}\cdot(\omega-\omega_0)^3 + \mathcal{O}(\omega^4)\end{aligned} \tag{2.24}$$

introduces the group delay dispersion (GDD) and third-order dispersion (TOD) as second and third derivative with respect to frequency, respectively. The group delay ϕ_1 accounts for a time delay of the pulse envelope. This already hints that there is a connection to the dispersion when light interacts with matter. In general, *dispersion* means that a property is frequency-dependent. In the context of optics this refers to the change of the refractive index n for different frequencies, so $n = n(\omega)$. A rainbow gives an intuitive understanding of this phenomenon—the splitting of the colours is happening exactly due to this phenomenon of dispersion in the water droplets [44]. In a weakly dispersive medium where the change of the refractive index over the frequency range of the pulse is small compared to the refractive index itself ($\Delta n(\omega) \ll n(\omega)$), an initial pulse $E(z=0,t)$, described by (2.15), can be written as

$$E(z_1,t) = A\left(t - \frac{z_1}{c}\right)\exp\left(i\omega_0\left(t - \frac{z_1}{v}\right)\right), \tag{2.25}$$

after propagating through the dispersive material of length z_1 with the group velocity v given by

$$v^{-1} = \frac{d}{d\omega}\left(\frac{\omega n(\omega)}{c_0}\right). \tag{2.26}$$

The group velocity itself usually depends on the frequency as well. Applying the concept of group velocity to the pulse in Fig. 2.4 means we can understand the frequency variations as the different frequency components in the wavepacket as illustrated in Fig. 2.1. They travel at different group velocities, stretching the pulse as faster components are at the front of the pulse and slower components at the back of the pulse. Quantitatively, this is the group velocity dispersion GVD which is

$$\mathrm{GVD} = \frac{d}{d\omega}\left(v^{-1}\right) = \frac{d^2}{d\omega^2}\left(\frac{\omega n(\omega)}{c_0}\right) \tag{2.27}$$

and now connects to the group delay dispersion GDD, *cf.* (2.24), just by multiplying the propagation length l onto the material constant GVD as

$$\mathrm{GDD} = \mathrm{GVD} \cdot l. \tag{2.28}$$

This is the connection of refractive index and phase of a pulse. The treatment for the third derivative, i.e. the TOD, is analogous [39]. Usually it is sufficient to look at the GDD and TOD that a pulse acquires when propagating through a dispersive material, neglecting higher orders. Note that the course of ϕ (Fig. 2.3(b), brown) is given by GDD and TOD. The nomenclature claims positive values of GDD as normal dispersion and negative values as anomalous dispersion. These parameters are usually given in units of fs^2 for GDD and fs^3 for TOD in ultrafast optics. Consequently, a dispersive material can convert a pulse closer to its transform-limited variant or further away. In other words, it can change the chirp of the pulse.

There is an empirical relation for the course of the refractive index over a wavelength range, the Sellmaier equation [45]

$$n^2(\lambda) = 1 + \sum_i \frac{B_i \lambda^2}{\lambda^2 - C_i} \tag{2.29}$$

with the Sellmaier coefficients B_i and C_i. From this equation, one can fit the GVD and TOD parameters. For transparent glasses, the sum can be restricted to $i = 1, 2, 3$ and the equation simplifies to [46]

$$n^2(\lambda) = 1 + \frac{B_1 \lambda^2}{\lambda^2 - C_1} + \frac{B_2 \lambda^2}{\lambda^2 - C_2} + \frac{B_3 \lambda^2}{\lambda^2 - C_3}. \tag{2.30}$$

2.4 Nonlinear Optics

The propagation of ultrashort laser pulses in matter is not only characterized by the different evolution of different frequency components, seen in Section 2.1, but also by the interaction of the material with the high peak powers of these laser pulses. As opposed to the linear model used in classical optics, a new regime of interactions between light and matter has to be introduced, where nonlinearities need to be considered. When the laser electric field $\vec{E}$ propagates through a medium with susceptibility χ, a linear relation

$$\vec{P} = \epsilon_0 \chi \vec{E} \tag{2.31}$$

for the polarization $\vec{P}$ is assumed in classical optics with the vacuum permittivity ϵ_0. This is a linear approximation that stems from the Lorentz oscillator model [47]. It assumes that the electronic binding forces can be described linearly. The refractive index n is connected to the susceptibility as

$$n = \sqrt{1 + \chi} \tag{2.32}$$

for weakly absorbing media. For laser field strengths comparable to the interatomic field strengths, the situation is more complex. Comparable to a far extended spring, when the relation between force and deflection becomes nonlinear, a Taylor expansion is necessary for the polarization of a medium:

$$\vec{P} = \epsilon_0 \big(\chi_1 \vec{E} + \chi_2 |\vec{E}| \vec{E} + \chi_3 \vec{E}^3 + \mathcal{O}(E^4) \big). \tag{2.33}$$

Different orders of this expansion are responsible for various phenomena. The second-order term $\vec{P}_2 = \epsilon_0 \chi_2 |\vec{E}| \vec{E}$ can be described in the photon picture. Two photons of frequency ω generate one photon of frequency 2ω as

$$\hbar\omega + \hbar\omega = \hbar(2\omega), \tag{2.34}$$

conserving the total energy. This process is called second-harmonic generation (SHG)—the generated light lies at twice the initial frequency. A schematic energy diagram of this process is shown in Fig. 2.5.

As the momentum is also conserved, the momenta of the incidental photons match the momentum of the outgoing photon, so

$$\hbar\vec{k}_\omega + \hbar\vec{k}_\omega = \hbar\vec{k}_{2\omega}. \tag{2.35}$$

The phase of the generated second harmonic and the incidental beam are then identical. This is a necessary condition for second-harmonic generation: The generated second harmonic after a small propagation distance in the material is still interfering constructively with the light generated at an earlier point in the crystal. The right end of Fig. 2.5 shows this constructive interference of the second harmonic for two photons, emitted at different positions along the crystal.

Using $k = n\omega/c$, the phase matching condition

$$n_\omega = n_{2\omega} \tag{2.36}$$

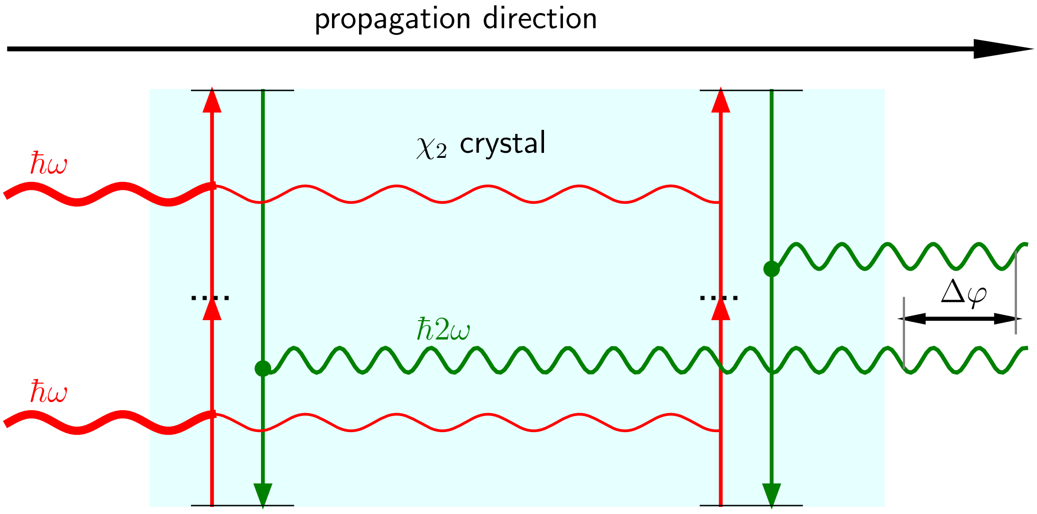

Figure 2.5: Schematic energy diagram of second-harmonic generation: Two incoming photons of frequency ω (red) generate a photon with doubled frequency 2ω (green) at two positions in the nonlinear crystal at the positions marked with green dots. $\Delta\varphi$ marks the phase difference. For phase-matching, it needs to be at even multiple integers of π.

follows directly. The highest efficiency of the process is therefore given for matching refractive indices, as then, constructive interference is achieved. The polarizability of a nonlinear medium can lead to a phase mismatch so that the wave vectors do not align. Crystals have a regular structure with symmetry axes that allow frequency conversion.

For an uniaxial crystal, distinguishing between the ordinary (o) and extraordinary (e) crystal axis which differ in their refractive indices n_o and n_e is necessary. The overall refractive index is then given by

$$\frac{1}{n^2(\Theta,\omega)} = \frac{\cos^2\Theta}{n_o^2(\omega)} + \frac{\sin^2\Theta}{n_e^2(\omega)}, \tag{2.37}$$

with the angle Θ between the wave axis and the optical axis of the crystal [47]. For a certain angle Θ, phase matching is fulfilled and light at doubled frequency can be generated.

For a material with negligible second-order nonlinearity, the Taylor expansion reads

$$\begin{aligned} \vec{P} &= \epsilon_0\big(\chi_1 + \chi_3|\vec{E}|^2\big)\vec{E} \\ &= \chi_{\text{eff}}\vec{E}. \end{aligned} \tag{2.38}$$

Replacing both prefactors with an effective polarizability χ_{eff}, the description simplifies to

$$n_{\text{eff}} = n + n_2 I, \tag{2.39}$$

with an effective intensity-dependent refractive index n_{eff}. The nonlinear part scales proportional to the intensity I with a prefactor of

$$n_2 = \frac{3\chi_3}{4\epsilon_0 c n^2}, \tag{2.40}$$

commonly given in $\mathrm{cm^2\,W^{-1}}$. Fused silica has a nonlinear index of $2.19 \times 10^{-16}\,\mathrm{cm^2\,W^{-1}}$ [48]. This nonlinear regime is of particular interest for pulse shaping applications as peak intensities lie on the order of $1 \times 10^{14}\,\mathrm{W\,cm^{-2}}$ in state-of-the-art ultrafast laser systems [49]. The nonlinear part in (2.39) is already 10^{-2} of the classical refractive index.

As the full description includes temporal *and* spatial dimensions, the nonlinearities alter the laser light in both space and time. It is called *self-phase modulation* (SPM) in the time domain and *self-focusing* in the spatial domain.

Self-phase modulation is a shift in the phase by

$$\Delta\varphi = \frac{2\pi}{\lambda} n_2 I L, \tag{2.41}$$

after a propagation length L in a nonlinear medium [50]. As mentioned above, the instantaneous frequency ω_i is the derivative of the phase. Self-phase modulation generates new frequencies, i.e. it broadens the spectrum of the pulse. It does however not change the temporal intensity profile of the pulse. The pulse gets up-chirped as depicted in Fig. 2.6(a). A Fourier transform of this pulse shows characteristic sidebands in the spectrum, as depicted in Fig. 2.6(b).

Self-focusing is the spatial interaction between beam and nonlinear medium. The beam acts as a lens on itself. Fig. 2.7 shows a Gaussian beam waist in the near field, focused in a nonlinear medium. For a spatial Gaussian profile (*cf.* Section 2.8), this interaction will be described in the following. In the beam center, the intensity is higher and so are the nonlinearities compared to the flanks of the beam where the linear interaction dominates. Hence, the refractive index is higher in the center and the beam is focused by itself in the spatial domain. This can lead to *catastrophic self-focusing*: With higher focus, the intensity increases and so does the nonlinearity. This self-reinforcing phenomenon can lead to destruction of the nonlinear medium for long propagation distances.

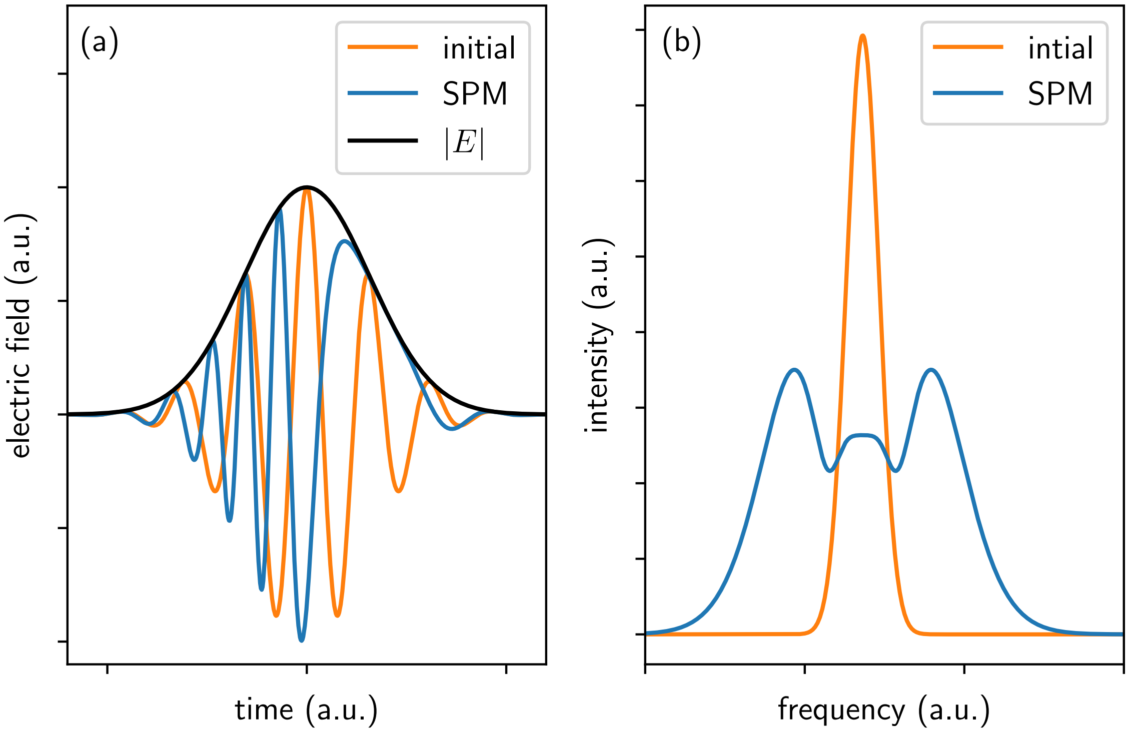

Figure 2.6: An initially transform-limited pulse (orange) undergoing self-phase modulation (SPM) (blue) with (a) unchanged temporal shape (black) and (b) characteristic sidebands in the spectral domain.

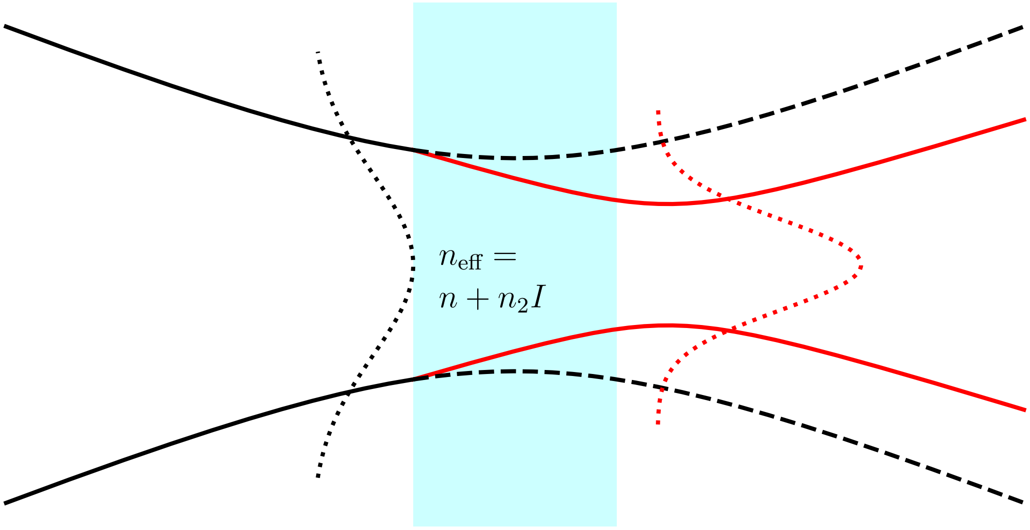

Figure 2.7: Self-focusing of a Gaussian beam (black) in a nonlinear medium (blue) with nonlinear index n_2 yields a smaller beam waist (red).

Including effects of the second-order nonlinearity in a single equation yields the *nonlinear Schrödinger equation* [51] which reads

$$\frac{\partial^2 A}{\partial x^2} + \frac{n_2}{\eta_0} k^2 |A|^2 A = 2ik \frac{\partial A}{\partial z} \tag{2.42}$$

for the pulse envelope $A(x, z)$ propagating along the z direction, *cf.* (2.15). x is the orthogonal distance from the optical axis and $\eta_0 = n|E|^2/(2I)$ condenses some prefactors. It can be derived from the paraxial Helmholtz equation assuming a slowly varying envelope and small nonlinear effects ($n_2 I \ll n$). The paraxiality gives a radial symmetry and, therefore allowing a restriction to a single coordinate x orthogonal to z.

2.5 Extremely Nonlinear Optics: High Harmonic Generation

For even stronger laser field strengths, the interactions need a different description. Such strong laser fields can be created in passive enhancement cavities in vacuum, where the roundtrip time in the cavity matches the repetition rate of the laser seeding the cavity. The circulating pulses are then resonantly enhanced, increasing the peak power to unprecedented levels.

Laser systems directly operating in the extreme ultraviolet (XUV) regime at wavelengths below 200 nm are not readily available. Therefore, the precision of the comb structure is limited to the regime where stable (fiber-based) laser systems are located, i.e. the near-infrared regime and the derived regimes accessible by second- or third-harmonic generation.

Transferring the comb structure from the near-infrared to the XUV is possible using high-harmonic generation (HHG) [20]. This phenomenon occurs upon shining intense laser light in a noble gas. It produces odd multiple integers of the incidental laser frequency. For a complete picture of the process, a quantum theory known as *Lewenstein model* [52] is necessary. However, a semi-classical description sufficiently explains the phenomena relevant for this thesis. The schematics of this simpler *three-step model* are shown in Fig. 2.8(a):

1. When a laser beam hits a gas target, the oscillation of the laser electric field (red) alters the Coulomb potential (blue) of the gas atoms. Then, the electron (green) is able to tunnel out of the atomic potential. As a free electron, it has a harmonic

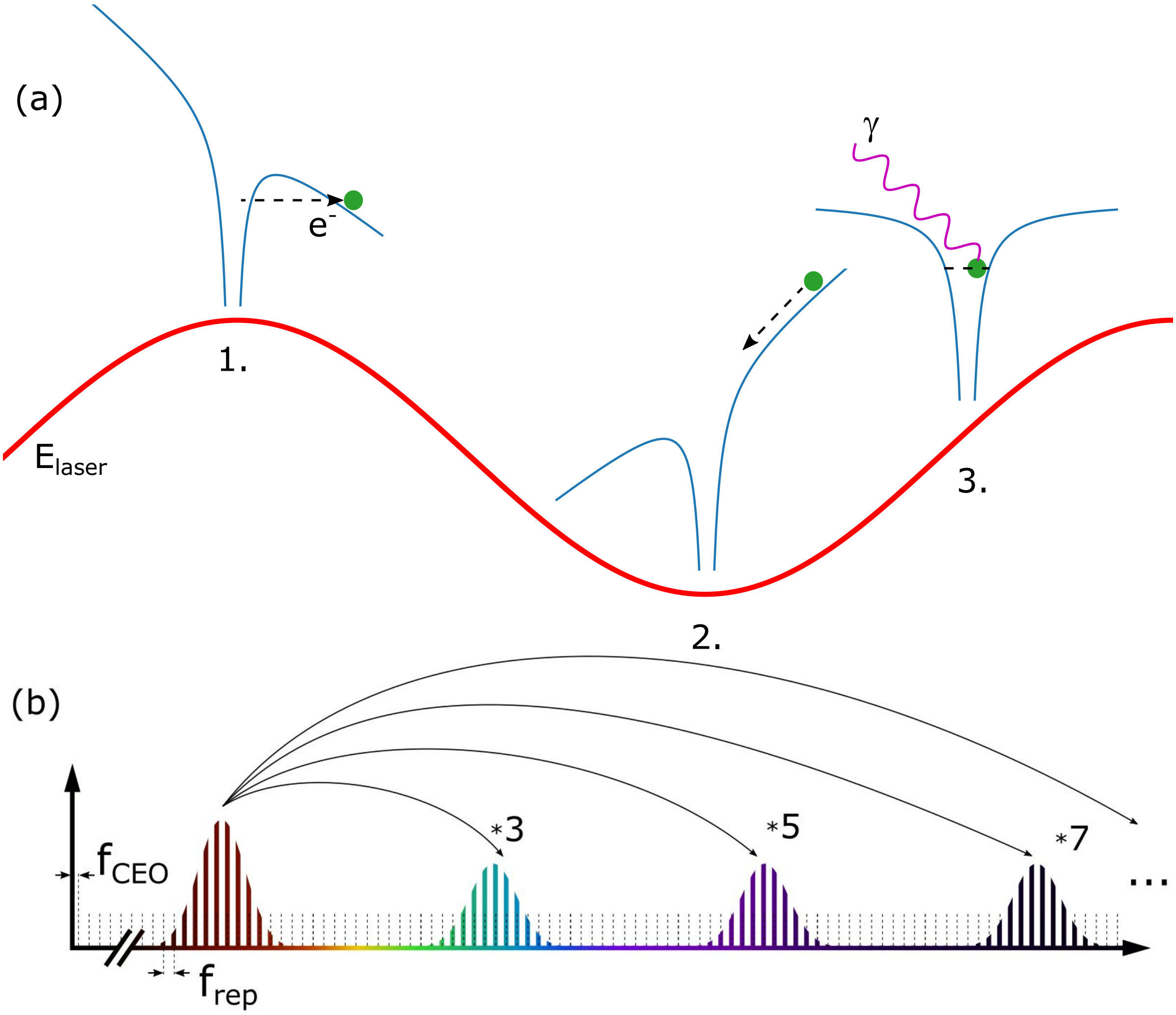

Figure 2.8: Working principle of an XUV frequency comb: (a) HHG based on the three-step model: 1. The laser field (red) changes the Coulomb potential (blue) of the atom so an electron (green) can tunnel out. 2. The oscillation of the laser field then accelerates the electron back to the atom. 3. Recollision then happens under emission of a high-energy photon. (b) This frequency of this high-energy photon lies at odd multiple integers (shown in green, violet, black) of the incidental laser frequency. Thus, the near-IR frequency comb structure (red) is transferred to the XUV. Taken from [25].

trajectory in the laser field and therefore a kinetic energy, called *ponderomotive energy*

$$U_{\text{pond}} = \frac{e^2 I_{\text{peak}}}{2c\epsilon_0 m_e \omega_c^2}, \tag{2.43}$$

with the elementary charge e, peak laser intensity I_{peak}, vacuum permittivity ϵ_0 and electron mass m_e.

2. After half an optical cycle, the Coulomb potential is perturbed in the other direction. This accelerates the electron back to the core. The equations of motion for position x and velocity v in the laser electric field with amplitude $E_0 = \sqrt{2I_{\text{peak}}/(c\epsilon_0)}$ are given by [53]

$$\begin{aligned} x(\varphi) &= \frac{eE_0}{m_e\omega_c^2}\big(\cos\varphi_i - \cos\varphi + (\varphi - \varphi_i)\sin\varphi_i\big), \\ v(\varphi) &= \frac{eE_0}{m_e\omega_c}\big(\sin\varphi - \sin\varphi_i\big), \end{aligned} \tag{2.44}$$

and therefore the motion of returning to the core ion depends on the instantaneous phase φ_i of the laser electric field.

3. Recombination of electron and core then happens under emission of a high-energy photon γ. Its energy is given by

$$E_\gamma = 2U_{\text{pond}}\big(\sin\varphi - \sin\varphi_i\big)^2. \tag{2.45}$$

The suppression of even harmonics can only be explained with the quantum mechanical model. The maximal possible kinetic energy E_{cutoff} is reached for $\varphi_i = 0.31$ which can be graphically deduced [25]. It is then

$$E_{\text{cutoff}} = U_{\text{ion}} + 3.17U_{\text{pond}} \tag{2.46}$$

and limits the frequency range of harmonics that can be produced.

For estimation of the cross-section the *Keldysh parameter* [27] is defined as

$$\gamma_k = \sqrt{\frac{U_{\text{ion}}}{2U_{\text{pond}}}}, \tag{2.47}$$

where U_{ion} is the ionization potential of the particular gas atom. For low values of γ_k

close to one, the HHG process is more efficient.
The frequency comb structure of Fig. 2.2(b) can thus be transferred to higher frequencies as sketched in Fig. 2.8(b).A system like this can then be utilized for implementation of optical clocks in the XUV. The laser intensity I is proportional to the ponderomotive energy U_{pond} according to (2.43). Hence, shorter pulses with higher peak intensities yield a higher ponderomotive energy and are thus desirable for high harmonic generation: The Keldysh parameter decreases and the cutoff energy increases.

2.6 Measuring Ultrashort Laser Pulses

The duration of an event is usually measured with ease. A shorter event with a well known duration is taken as a reference. Then, the time can be quantified by counting the occurrence of the reference event in the measured timeframe. For example, in the time interval that Usain Bolt takes to run 100 m, the big watch hand moves 9 times and the small one another 69 times. This works fine until—inevitably—the shortest event is encountered. So what to do when there is no shorter reference available? The best reference available is the event *itself*.
Therefore, for ultrashort laser pulses, this reference is the pulse. Using a beamsplitter, the beam can be split up. This gives two identical pulses, enabling the measurement of the pulse with itself. There are different methods of comparing these two pulse copies. For the work described in this thesis, autocorrelation (AC) and frequency-resolved optical gating (FROG) are set up. As an interferometric-based as well as an intensity-based measurement method for both AC and FROG are in use, both are explained in more detail in this chapter.

Autocorrelation

Autocorrelation measures the intensity of a pulse over time. The general optical implementation is shown in Fig. 2.9. Propagating the laser beam through a 50:50 beamsplitter gives rise to two identical copies of the pulse with halved intensity. One pulse propagates along a beam path with adjustable path length. For a difference between both path lengths d, the pulses are temporally delayed by a time $\tau = d/c$. The beams are then spatially overlapped in a nonlinear crystal. A lens focuses the beams in the crystal to increase the spatial intensity, so that the nonlinear process—which is highly dependent on the intensity—is more pronounced. With the nonlinear intensity dependence of second-harmonic generation (SHG, *cf.* Section 2.4), differing delays are responsible for differing

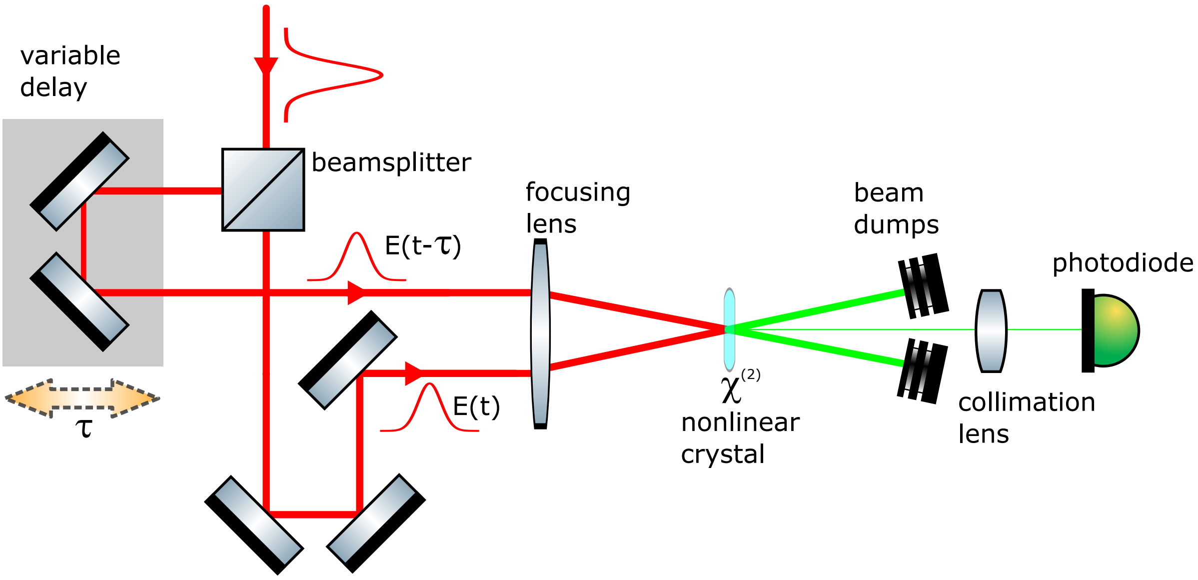

Figure 2.9: Optical setup of intensity autocorrelation. The beam is split up, one part is traveling through an adjustable delay stage. Both beams are then focused into a nonlinear crystal. The $\chi^{(2)}$crystal response on the delayed pulses is measured with a photodiode.

signals. Only by delaying the pulses, one can gain information about the temporal shape of the pulses. After the crystal, there is a small amount of light at doubled frequency exiting the crystal and the rest of the incidental light just continues to propagate along its beam path. The frequency-doubled signal is then detected with a photodiode or rather the integration of the pulse shape. Plotting the recorded signal versus the delay set in the beam path can then give information on the pulse structure.

The generated second harmonic at doubled frequency means that the wavelength is halved. The generated electric field $E(t)_{\text{SHG}}$ is proportional to the product of both pulses as [54]

$$E(t)_{\text{SHG}} \propto E(t)E(t-\tau). \tag{2.48}$$

As $I = |E|^2$, the resulting intensity is

$$I(t)_{\text{SHG}} \propto I(t)I(t-\tau). \tag{2.49}$$

A graphic analysis of the nonlinear crystal response on varying pulse delays is shown in Fig. 2.10. Pulse intensities of two delayed pulses with 250 fs pulse duration at FWHM are depicted in the top row (a–c). There is a delay of 400 fs in (a), a delay of 200 fs in

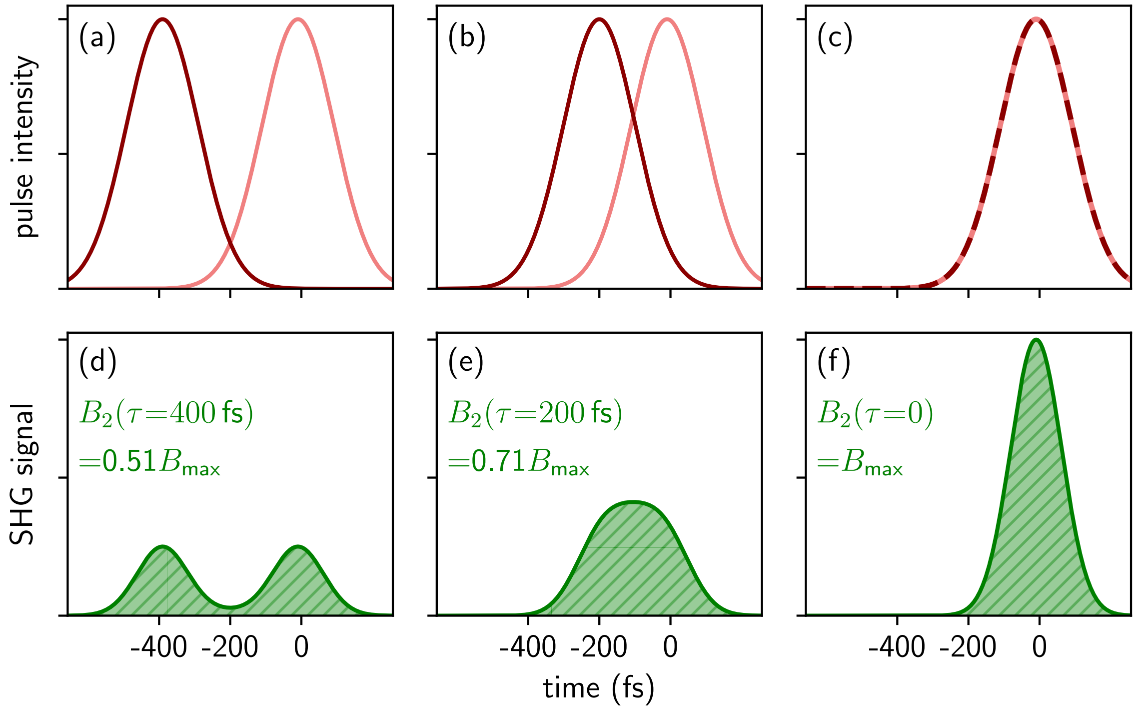

Figure 2.10: Laser pulses with decreasing delay (a–c). The integrated nonlinear response of the SHG signal $B_2(\tau)$ (d–f) gives rise to larger signals for shorter delay times.

(b) and full overlap in (c). This leads to differing SHG signals (d–f). As detectors are too slow to resolve this temporally, we can only measure the overall signal

$$B_2(\tau) = \int_{-\infty}^{\infty} I(t)I(t-\tau)dt; \tag{2.50}$$

indicated by the hatched green area under the curves. The relative signal strength is also indicated in the plot: The signal gradually gets stronger from (d) to (e) to (f). Plotting the recorded signal, usually detected by a photodiode, versus the delay steps yields the autocorrelation *trace*. The generated autocorrelation trace (Fig. 2.11 (d)) has a longer width than the original pulse (Fig. 2.11 (a)) as it is the convolution of the two pulses. For a perfect Gaussian, the convolution factor results in the relation

$$\tau = 0.7071 \cdot \tau_{AC} \tag{2.51}$$

between the full widths at half maximum of the pulse envelope τ and the autocorrelation trace τ_{AC}.

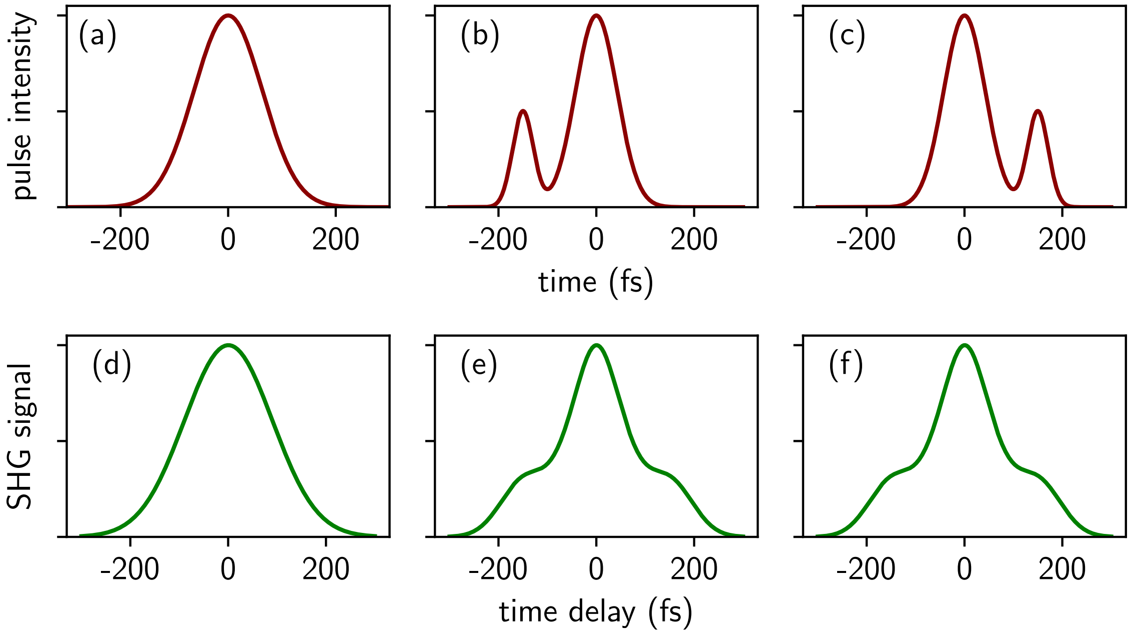

Figure 2.11: (a) A Gaussian pulse, (b) a pulse with a pre-pulse and (c) a pulse with a post-pulse. (d) The intensity autocorrelation signal for the Gaussian, (e-f) both pre-and post-pulse exhibit the same signal.

Autocorrelation reveals only a limited amount of information on the pulse. The autocorrelation trace is symmetric, whilst the pulse may well not be. This is because the pulse is measured with itself by delaying one pulse with respect to the other—so $\Delta\tau > 0$ and $\Delta\tau < 0$ yield the same signal. This becomes particularly troublesome for asymmetric pulse shapes, for example a main pulse that is accompanied by a satellite pulse as in Fig. 2.11: In the top row, there is a main pulse with (b) a pre- and (c) post-pulse. The resulting autocorrelation signal for each pulse shape is shown in (e) and (f). Both structures lead to the same signal when a Gaussian envelope is assumed.

It is also possible to use a collinear alignment of the two beams with the separated pulses instead of crossing the beams in the nonlinear crystal. *Interferometric autocorrelation* generates a nonlinear response directly resulting from the interferometry of the delayed pulses. So instead of the setup shown in Fig. 2.9, the beams are guided onto the same path as in Fig. 2.12.

This changes the generated signal: Only the intensity envelopes were considered in the previous setup (*cf.* Fig. 2.10). Here, the actual electric field is taken into account. The delayed pulses generate the same polarization response with respect to the crystal axes, so we need to consider their phase. Two schematic pulses, or rather the real part of their

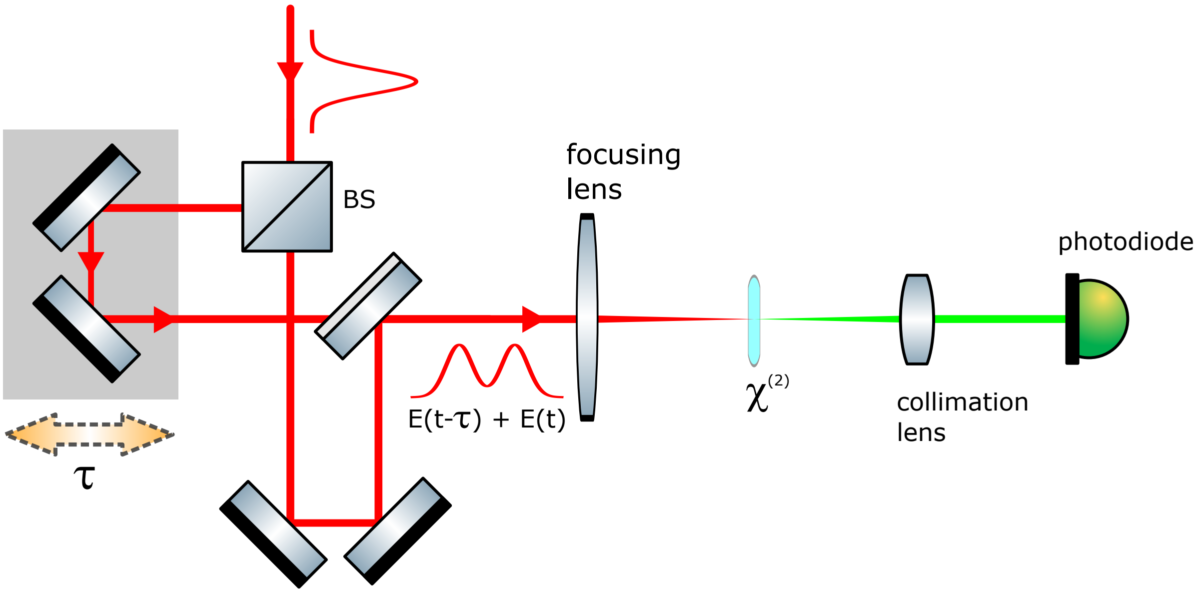

Figure 2.12: Optical setup of interferometric autocorrelation. The beam is split up and overlayed again with delayed pulses. The nonlinear crystal response on the interferometry is measured with a photodiode.

respective electric fields are shown in Fig. 2.13 in red and orange in the top row. In (a), where the pulses are in phase and interfere constructively, the situation is still the same as it was before: The signal strength of the second harmonic is unchanged for zero delay. But for a delay of half an optical cycle in (b), where the pulses are out of phase and interfere destructively, there is almost no signal. This leads to an autocorrelation trace with interferometric wiggles under the envelope. It is possible to extract additional phase information from the interferometric structure with a combination of genetic algorithms and graduated optimization algorithms [55], but the retrieval tends to be unreliable [54]. Thus, interferometric autocorrelation does also not provide a pulse characterization with reliable phase and envelope information. It may path a way to obtain at least some information on the pulse shape in a relative simple setup. Yet, nontrivial ambiguities such as pre- and post-pulses can still not be identified sufficiently.

Frequency-Resolved Optical Gating

The shortcomings of autocorrelation can be overcome by measuring more information contained in the SHG signal. By using a spectrometer instead of a photodiode, complementary information in the frequency domain can be obtained. The extraction of not only the pulse intensity, but also the phase is then possible.
For every delay step, a full spectrum is recorded. The total information is contained

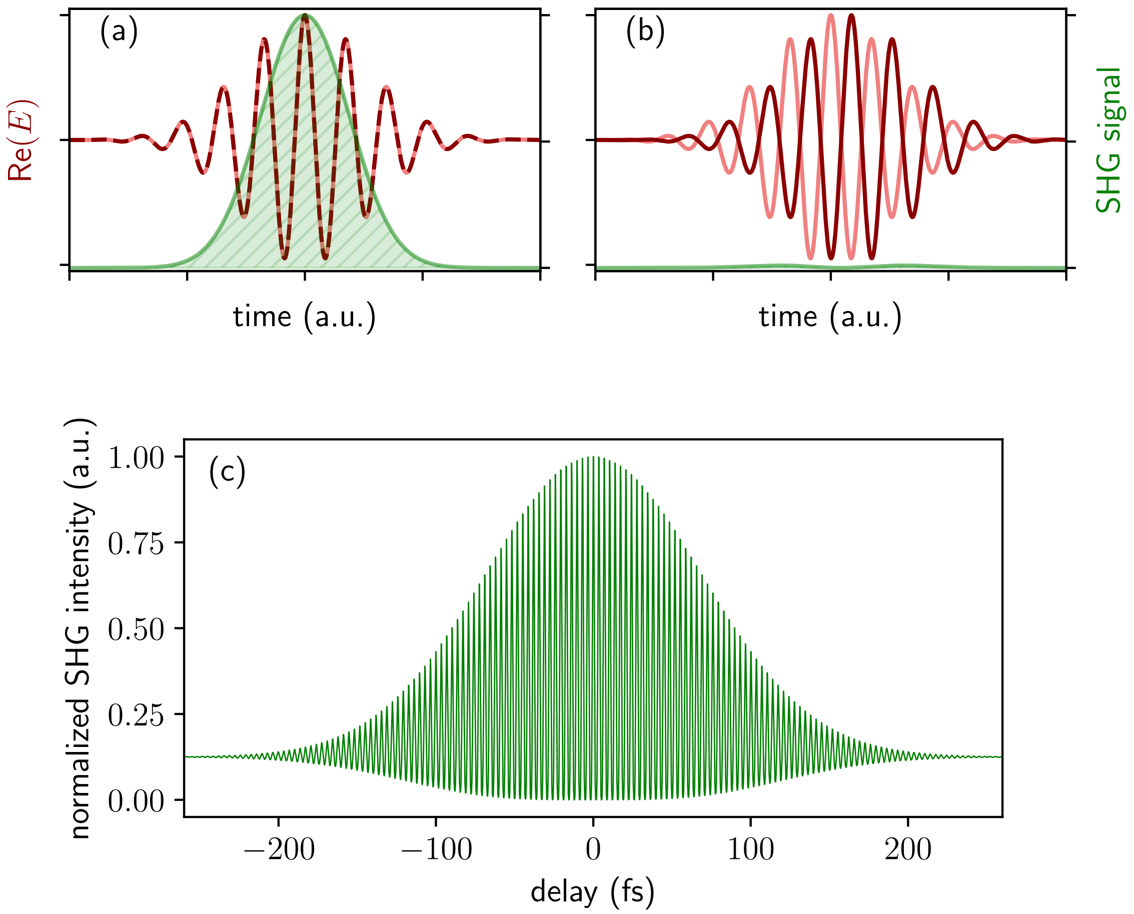

Figure 2.13: Nonlinear SHG response of a crystal considering the electric field. (a) Zero delay yields a strong signal while (b) a delay of half an optical cycle delivers almost zero signal. (c) Plotting the signal strength against the delay yields an autocorrelation trace, here for a Gaussian pulse with 150 fs FWHM centered around 1030 nm. For large delays, the pulses do not overlap temporally and the generated signal is the sum of both individually generated signals, i.e. at 1/8 of the signal for zero delay.

in the *trace*. An ideal trace is shown in Fig. 2.14(c) for a Gaussian pulse in the time domain (a) and the frequency domain (b). The intensity is recorded for every wavelength (ordinate) and delay step (abscissa) and is pictured in Fig. 2.14(c,f) with a colorscale indicating the intensity. The pulse is optically gated by itself in an autocorrelation setup to generate a frequency-doubled delay-dependent signal, subsequently spectrally resolved into the frequency components: This technique is therefore called **f**requency-**r**esolved **o**ptical **g**ating (FROG).

The nonlinear crystal generates the second harmonic of the measured pulse. Therefore, the spectrogram, usually given in the wavelength domain, has its axis centered around half the wavelength of the measured pulse. For a pulse after self-phase modulation, shown in (b) and (d), the trace in (f) looks fundamentally different. First guesses of the intensity profile, and even the phase, is possible from looking at the trace.

Frequency-resolving the signal from an interferometric autocorrelation setup yields the interferometric FROG (iFROG) trace. The interference pattern is clearly visible in the iFROG-trace in Fig. 2.15 (a) and (b). Both FROG and iFROG traces can be used for retrieval of the pulse shape. For both autocorrelation and frequency-resolved optical gating, the interferometric setup is easier to align as the beams are already overlapped before the crystal. Scanning each optical cycle with sufficient resolution makes the recording of the interferometric signal slower compared to the intensity-based method.

The full recorded trace of an ultrashort laser pulse system delivers sufficient information to determine the complex electric field of the pulse as it contains measurements in the frequency domain and measurements in the time domain [56]. A phase-retrieval algorithm can then transfer the FROG trace to a full retrieval of intensity and phase of the pulse. FROG algorithms have an iterative working principle which is schematically shown in Fig. 2.16. An initial reasonable guess for the electric field E_0 is used to generate the signal field $E_{sig}(t)$. With a Fourier transformation $\mathcal{F}$ one arrives at the signal field in the frequency domain $\tilde{E}_{sig}(\omega)$. Subsequently, the algorithm compares the measured trace and the signal field and concludes an improved expression for the signal field $\tilde{E}'_{sig}(\omega)$. This is now back-transformed into an improved signal field $E'_{sig}(t)$ with the inverse Fourier transform $\mathcal{F}^{-1}$. With this, a new guess for the input field can be taken and the algorithm starts the process again. The algorithm may be run several times to yield a satisfying result.

Retrieval of pulse shapes from iFROG traces is also possible with commercially available implementations of retrieval algorithms.

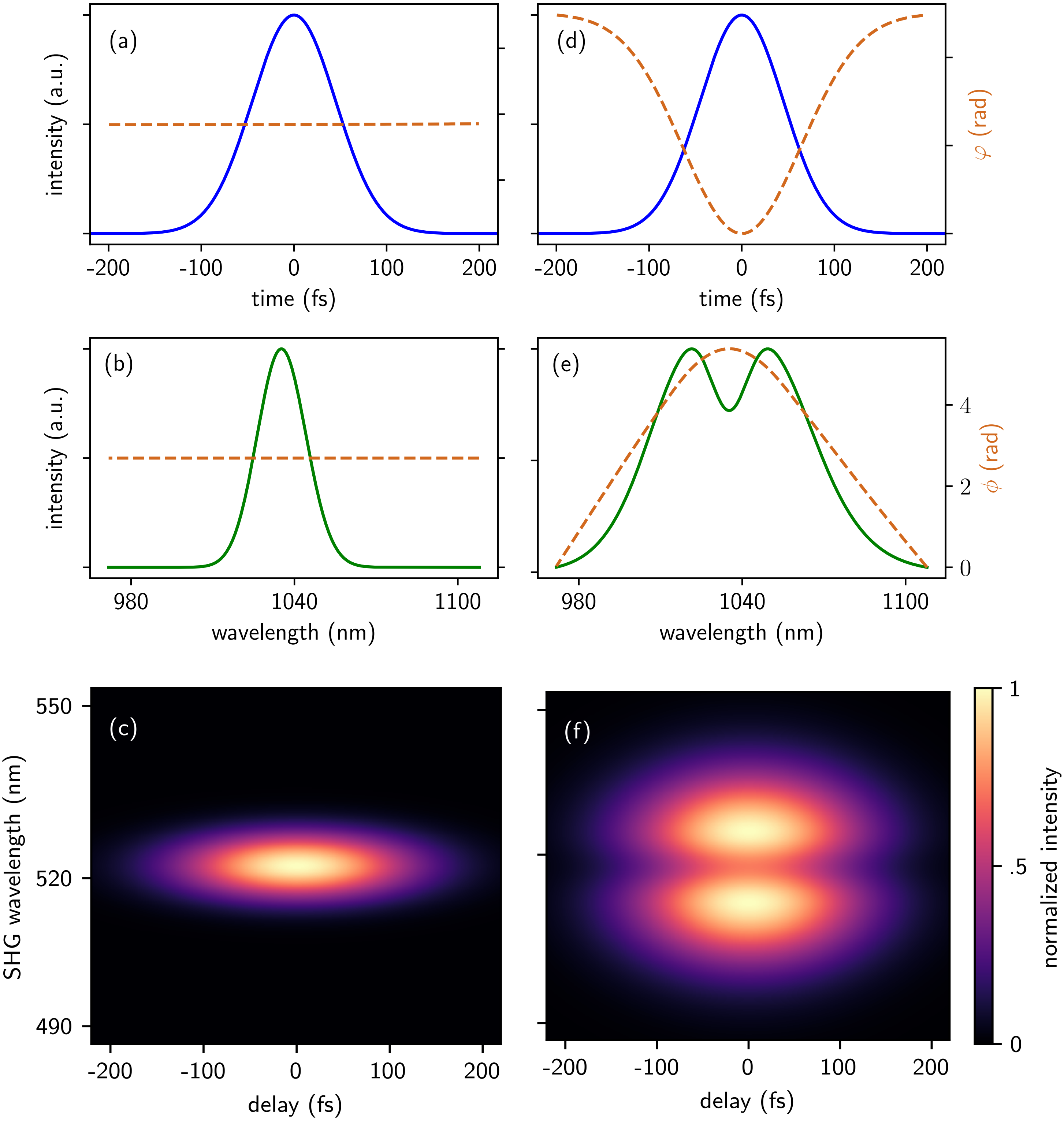

Figure 2.14: A Gaussian laser pulse (a) in the time domain and (b) the spectral domain. (c) The FROG trace of this pulse. (d) After self-phase modulation of this pulse the temporal shape is unchanged. (e) However, the spectral form has changed. (f) This is clearly visible in the trace.

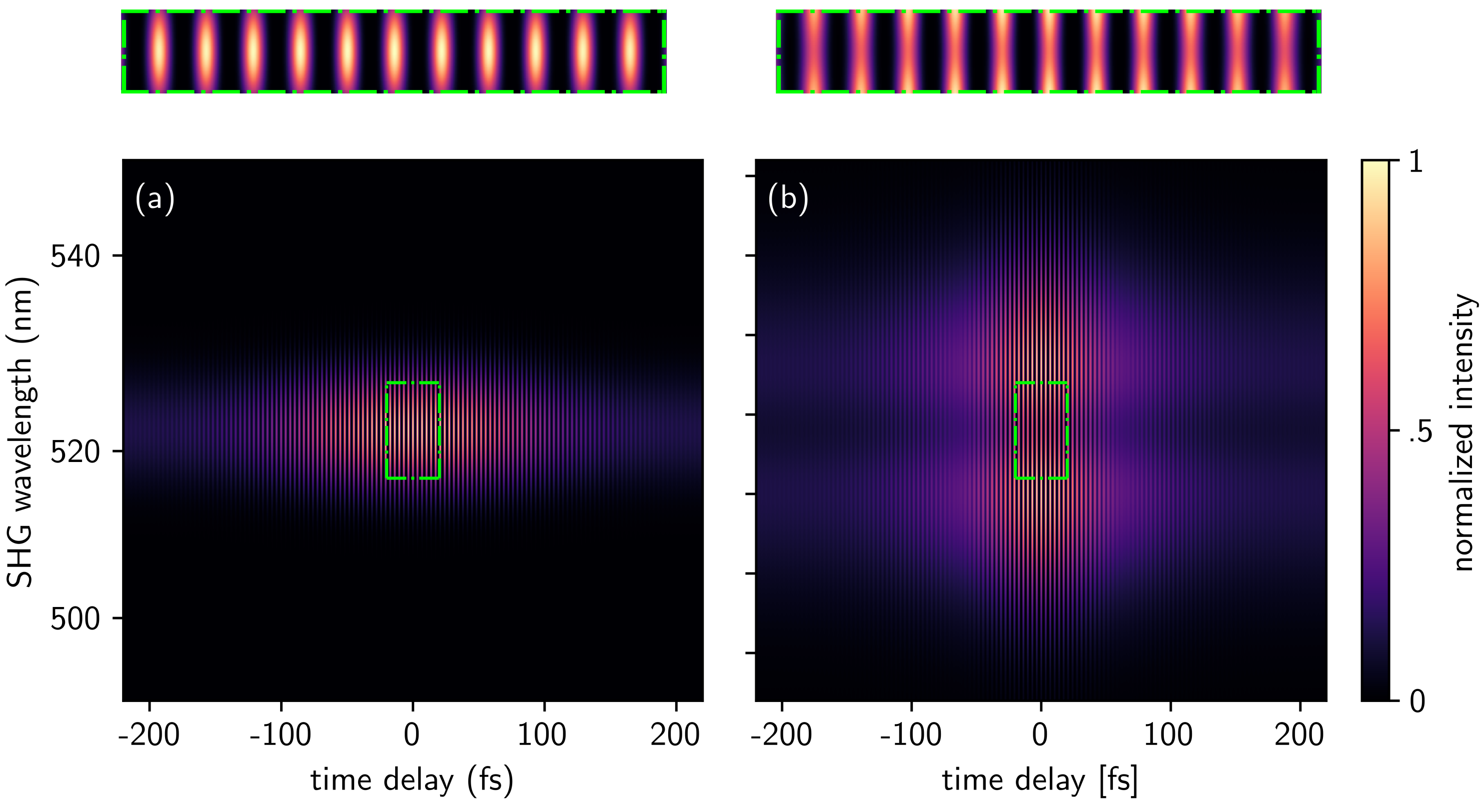

Figure 2.15: (a) iFROG trace of the pulse in Fig. 2.14(a–c). (b) iFROG trace of the pulse in Fig. 2.14(d–f). The zoom boxes, marked in green, show the interference fringes.

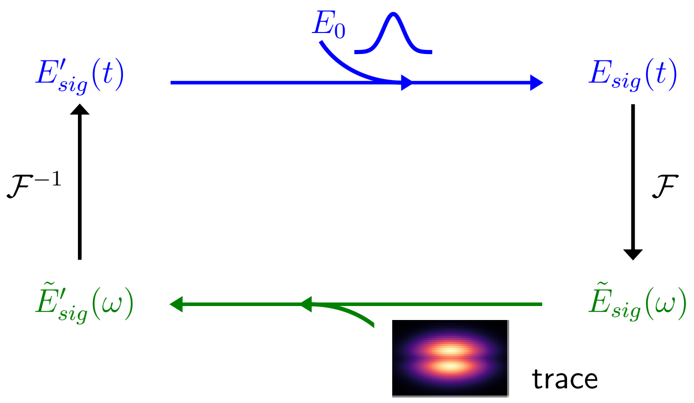

Figure 2.16: Working principle of the iterative FROG algorithm: An initial guess for the electric field E_0 is used to generate an artificial trace from the signal field E_{sig} with a Fourier transform $\mathcal{F}$. By comparison with the measured trace and inverse transformation $\mathcal{F}^{-1}$, the guess is improved and the process starts again.

2.7 Pulse Shaping Techniques

Self-phase modulation and chirp manipulation are useful for handling ultrashort laser pulses. Employing the material properties of dispersion and nonlinearities, they can be tailored to fit a specific application. Chirped pulse amplification [57] is widely used to generate pulses even in the multi-kW average power regime [58, 59]. By propagation in a material such as a fiber or by reflections at multiple gratings, the pulse acquires a chirp and is stretched in time [60, 61]. The peak power is then reduced and can be increased in a laser gain material without destroying said material by too high peak powers. By removing the chirp with a grating, a prism or the combined grism compressor[62, 63], the peak intensity increases again, to even higher values compared to the start.

Instead of pulse amplification, this section will focus on nonlinear pulse compression by spectral broadening, i.e. narrowing of the pulse in the time domain. Temporal compression of ultrashort laser pulses by chirp removal is only possible as long as they have not reached their transform limit yet. For further temporal compression, the spectrum needs to be broadened. A broader spectrum in the frequency domain enables shorter pulses in the time domain. The most prominent effect for such broadening, namely self-phase modulation, was already explained in Section 2.4. By propagation in a nonlinear material, the pulse will also acquire a chirp through the group velocity dispersion of the material, depending on the length according to (2.28). For transform-limited pulses, which are the shortest possible pulses for a given spectral distribution, this chirp needs to be removed.

Most materials exhibit a positive GVD in the near infrared where the central wavelength of this experiment lies, e.g. fused silica [64] or yttrium aluminium garnet (YAG) [65]. There are also materials that have anomalous dispersion such as Potassium Dihydrogen Phosphate (german *Kaliumdiphosphat*, KDP) [66]. The course of the refractive index of these materials is shown in Fig. 2.17(a). The group velocity dispersion corresponds to the curvature of the refractive index $n(\omega)$, i.e. the second derivative, which is plotted in 2.17(b). While YAG and fused silica have normal dispersion, the curvature of KDP changes at around 800 nm, exhibiting anomalous dispersion already in the near-infrared.

The compression factor strongly depends on the magnitude of the self-phase modulation φ in the nonlinear material. According to (2.41), it scales proportional to the nonlinear index n_2 and the intensity I. High intensities are therefore beneficial for pulse compression and can be achieved in a fiber. There are different types of fibers available. Commercially available passive fibers, made of fused silica have core diameters of up to 40 µm. For handling large input powers, this might not be sufficient. Even small misalignment or

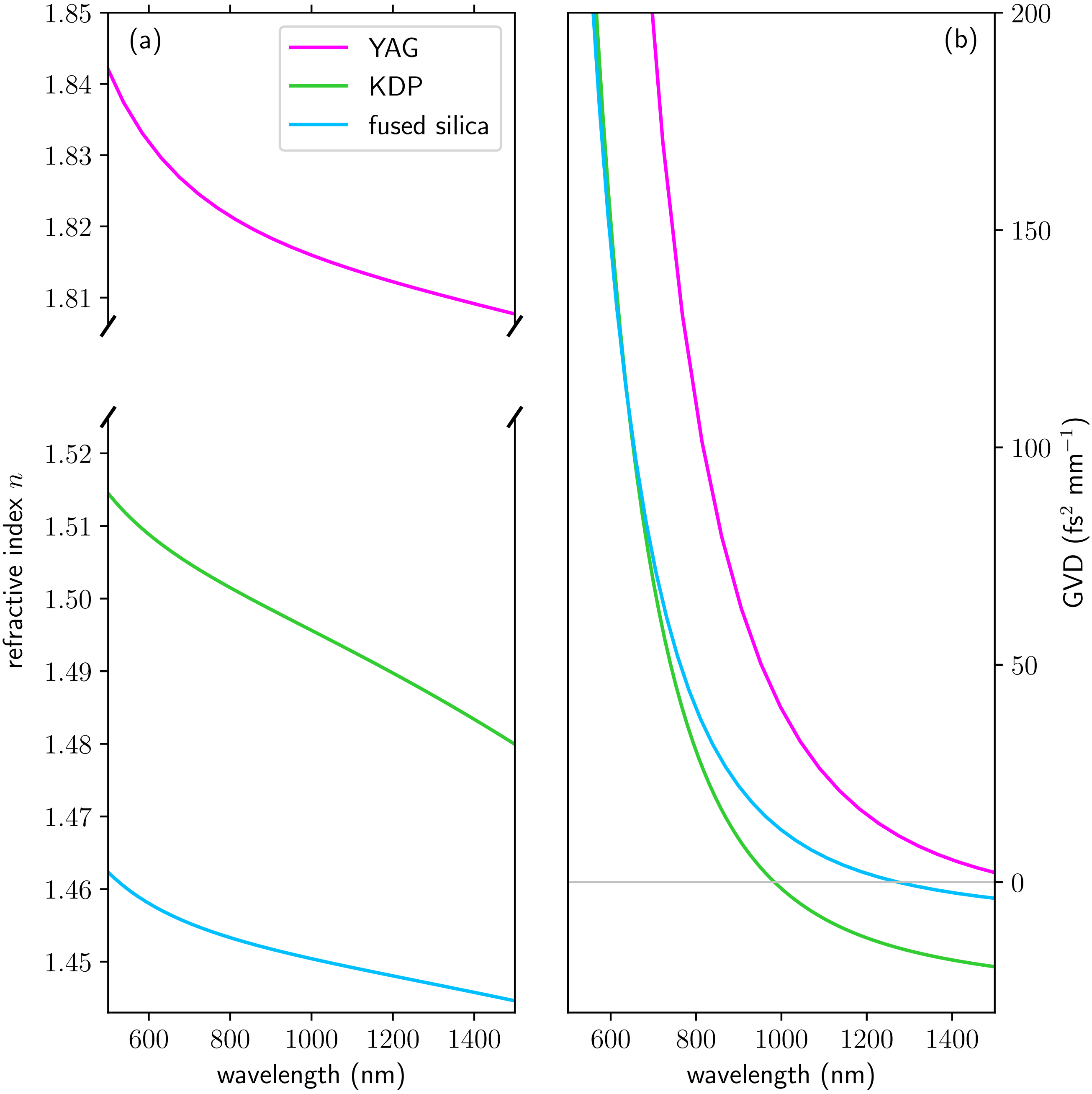

Figure 2.17: (a) Refractive index of KDP, YAG and fused silica as function of the wavelength. The beginning negative curvature of the KDP refractive index around 1000 nm hints at the anomalous dispersion. (b) GVD of these materials can be obtained by calculation of the second derivative. KDP has anomalous dispersion from 984 nm onwards. Data from [64–66].

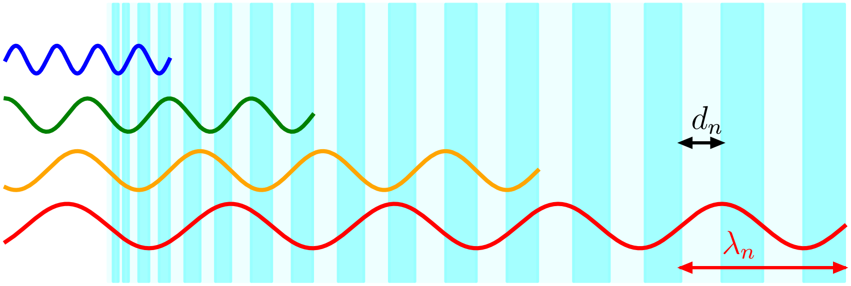

Figure 2.18: Working principle of a chirped mirror: The thickness of the layers increases in the mirror. Longer (red) wavelengths are reflected after a longer travel distance where the wavelength matches the layer thickness by $d_n = \lambda_n/4$, yielding anomalous dispersion.

dust on the fiber end lead to destruction of the fiber. Therefore, larger core diameters which incorporate photonic crystal structures were shown to deliver stable performance in pulse compression [67]. Gas can also be employed as nonlinear medium in fibers by using hollow cores. Delicate structures guide the light in the gas-filled core and nonlinear interaction with the gas broadens the spectrum [68]. The dispersion in hollow-core fibers can be tuned by the choice of different gases and gas pressures [69].

Compression is also possible in bulk material. For this, it is convenient to use a multipass cell which allows several propagation steps in the material. The multipass cell setup consists of curved mirrors on both sides and a bulk nonlinear material in the middle [30]. Curved mirrors ensure alignment stability on a Herriott-cell like beam path and focus the beam in the nonlinear material to reach higher intensities[70]. Multiple propagation steps instead of a propagation in one bulk crystal are necessary due to self-focusing, which would lead to destruction of the material after some propagation. In a setup with curved mirrors the beam instead widens up again. With small scraper mirrors, the beam can be coupled in and out of the cell.

The dispersion gained in a nonlinear material can be removed with a *chirped mirror*. The principle of such a device is shown in Fig. 2.18. Each wavelength is reflected at a multilayer. The thickness of the respective layers d_n where a certain wavelength is reflected matches the wavelengths $\lambda_n/4$ of the incidental pulse [71]. The longer wavelengths are reflected after a longer propagation distance in the material. This enables the removal of chirp acquired by propagation in a material with normal dispersion.

For multipass cells, the chirp removal can be done either inside the cell with a chirped curved mirror, with a set of chirped mirrors after the cell or a combination of both.

2.8 Gaussian Beam Propagation

For the analysis of the nonlinear interaction strengths and the multipass cell design, the spatial description of the laser beam needs further evaluation. For this, we start by formulating the principles of Gaussian beam propagation and will then continue to use the ABCD matrix formalism to simplify the description [72].

For an electromagnetic wave that propagates in z-direction the electric field is

$$E(x, y, z) = u(x, y, z) \exp(-ik), \tag{2.52}$$

where the spatial dependence of the scalar amplitude $u \in \mathbb{C}$ is considered explicitly on the coordinates x, y and z. Substituting this into the wave equation (2.4) and assuming $\Delta u(z) \ll u$, i.e. the amplitude varies slowly along the propagation axis, the wave equation can be re-written as the paraxial Helmholtz equation

$$\nabla_\perp^2 u(x, y, z) - 2ik \frac{\partial u(x, y, z)}{\partial z} = 0, \tag{2.53}$$

where paraxial means that we consider a wave close to the optical axis. The transverse Laplace operator $\nabla_\perp^2 = \partial^2/\partial x^2 + \partial^2/\partial y^2$ simplifies this equation. This is valid for divergence angles $\Theta \leq 30°$. A solution of this differential equation is the *Gaussian beam* that reads

$$u(r, z) = \frac{u_0}{\sqrt{1 + (z/z_R)^2}} \exp\left[-\frac{r^2}{\omega(z)^2} - ik\left(z + \frac{r^2}{2R(z)}\right) + i \arctan\left(\frac{z}{z_R}\right)\right]. \tag{2.54}$$

The symmetry of the problem was used to simplify the notation by writing $r^2 = x^2 + y^2$ for the transverse radial coordinate and

$$z_R = i\frac{w_0^2}{\lambda} \tag{2.55}$$

as the *Rayleigh length*, i.e. the distance from the focus where the beam waist reaches $\sqrt{2}w_0$.

Fig. 2.19 shows the beam around the focus. The beam waist $w(z)$, where the intensity reaches $1/e^2$ of its maximum value, evolves according to

$$w(z) = w_0\sqrt{\left(\frac{z}{z_R}\right) + 1}, \tag{2.56}$$

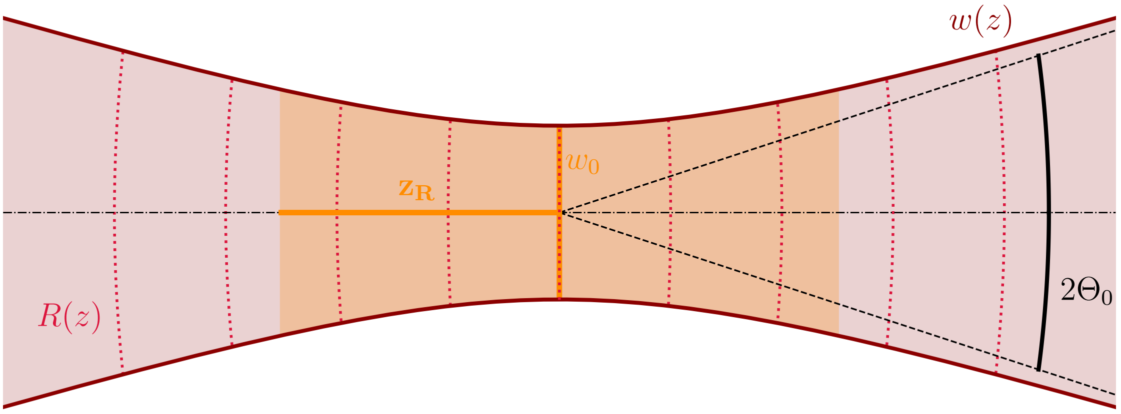

Figure 2.19: Focus of a Gaussian beam, where the characteristic parameters waist w_0, Rayleigh length z_R, divergence angle Θ_0 and wavefronts $R(z)$ are indicated. z measures the horizontal distance from the focal plane.

along the propagation length z. w_0 is the minimal beam waist. The orange area indicates the distances smaller than the Rayleigh length. The red-dotted wavefronts $R(z)$ have a curvature according to

$$R(z) = z\left(1 + \left(\frac{z_R}{z}\right)^2\right). \tag{2.57}$$

For $z = 0$, the wavefront is in a plane orthogonal to z.

By defining the complex beam parameter q as

$$q(z)^{-1} = R(z)^{-1} - i\frac{\lambda}{\pi w(z)^2}, \tag{2.58}$$

(2.54) simplifies to

$$u(r,z) = \frac{q_0}{w_0 q(z)} \exp\left(-ikz - ik\frac{r^2}{2q(z)}\right), \tag{2.59}$$

with $q_0 = i\pi w_0^2/\lambda = iz_R$. All relevant spatial information on the beam is contained in the q parameter. Physical effects on the beam profile can also be incorporated and the calculations are simplified. For example, the propagation in free space over a distance z

optical element	ABCD matrix
vacuum	$\begin{pmatrix} 1 & z \\ 0 & 1 \end{pmatrix}$
medium with refractive index n	$\begin{pmatrix} 1 & z/n \\ 0 & 1 \end{pmatrix}$
curved mirror, tangential plane	$\begin{pmatrix} 1 & 0 \\ -2/(R\cos\Theta) & 1 \end{pmatrix}$
curved mirror, sagittal plane	$\begin{pmatrix} 1 & 0 \\ -2\cos\Theta/R & 1 \end{pmatrix}$

Table 2.1: Ray matrices for the optical components used in this thesis with R as radius of curvature of the curved mirrors and an angle of incidence Θ on the curved mirror with respect to the optical axis. z refers to the propagation distance.

changes the q parameter by

$$q(z) = q_0 + z. \tag{2.60}$$

For more complex elements, the ABCD formalism offers a simple method to propagate the q parameter through various optical elements. The formalism of ray transfer matrices from classical optics is adopted. After an optical element with ray transfer matrix M and entries A, B, C and D as

$$M = \begin{pmatrix} A & B \\ C & D \end{pmatrix}, \tag{2.61}$$

the beam parameter q' is

$$q' = \frac{Aq + B}{Cq + D}. \tag{2.62}$$

The matrices in use for this thesis are shown in Table 2.1.

The beam parameters can then be recovered from the q parameter via the relations

$$R(z) = \frac{1}{\mathrm{Re}\left(q(z)^{-1}\right)}, \tag{2.63}$$

for the wavefronts of the beam and

$$w(z) = \sqrt{\mathrm{Im}\Big(q(z)\Big)\frac{\lambda}{\pi}}, \tag{2.64}$$

for the beam waist size.

With these concepts at hand, the multipass cell design is explained in more detail in Chapter 4. Nonlinear interactions and dispersion are evaluated for the setup of a compression scheme, whereas the evaluation of spatial beam properties determine the geometric design of the cell.

3 Experimental Setup

The experimental setup relevant for the scope of this thesis is described in this chapter. An introduction of the laser system seeding the enhancement cavities is followed by a description of the pulse characterization instrumentation built for this thesis. A more detailed description on the passive enhancement cavity can be found in [25].

3.1 Oscillator, Amplifier and Compressor

A graphical overview of the laser system before the pulse characterization setup is shown in Fig. 3.1.

The laser system is seeded by a commercially available frequency comb FC1000-250 from Menlo Systems GmbH. This oscillator is a Yb:glass fiber laser which is specified to a central frequency of 1039 nm with a spectral width of 7 nm. For the high precision necessary in the experiment, the fiber comb has a repetition rate of 100 MHz. The light is then coupled out of the fiber oscillator and propagated through 60 m of passive fiber (XP980-PM, Nufern) to stretch the pulses to 24 ps. The beam can then either be sent through a grism compressor to achieve an overall average power of 12 W and a pulse length of 170 fs or it is directly outcoupled to have 15 W of average power with the stretched 24 ps pulses [25]. However, more than the readily available 15 W power are necessary for the generation of high harmonics and a further amplification stage was built.

The beam is coupled into a 80 cm long Yb-doped rod-type photonic crystal fiber amplifier (aeroGAIN-ROD-MODULE-2.0 PM85, NKT photonics) pumped with 250 W of continuous-wave light at 976 nm from a fiber diode (D4F2S22-976.3-250C-IS58.1, DILAS Diodenlaser GmbH). Coupling of the pump light into the fiber is done with an off-axis parabolic mirror (OAP). Back-reflections into the fiber comb are prevented by a Faraday isolator (PAVOS-Ultra-0-I-1015-1065, Soliton). A beam dump with a hole in the center followed by a collimation lens and a dichroic mirror separates the pump light from the seed. Afterwards, the amplified pulses are compressed via a home-built grating compressor. It consists of a transmission grating with a line density of 1000 mm^{-1}

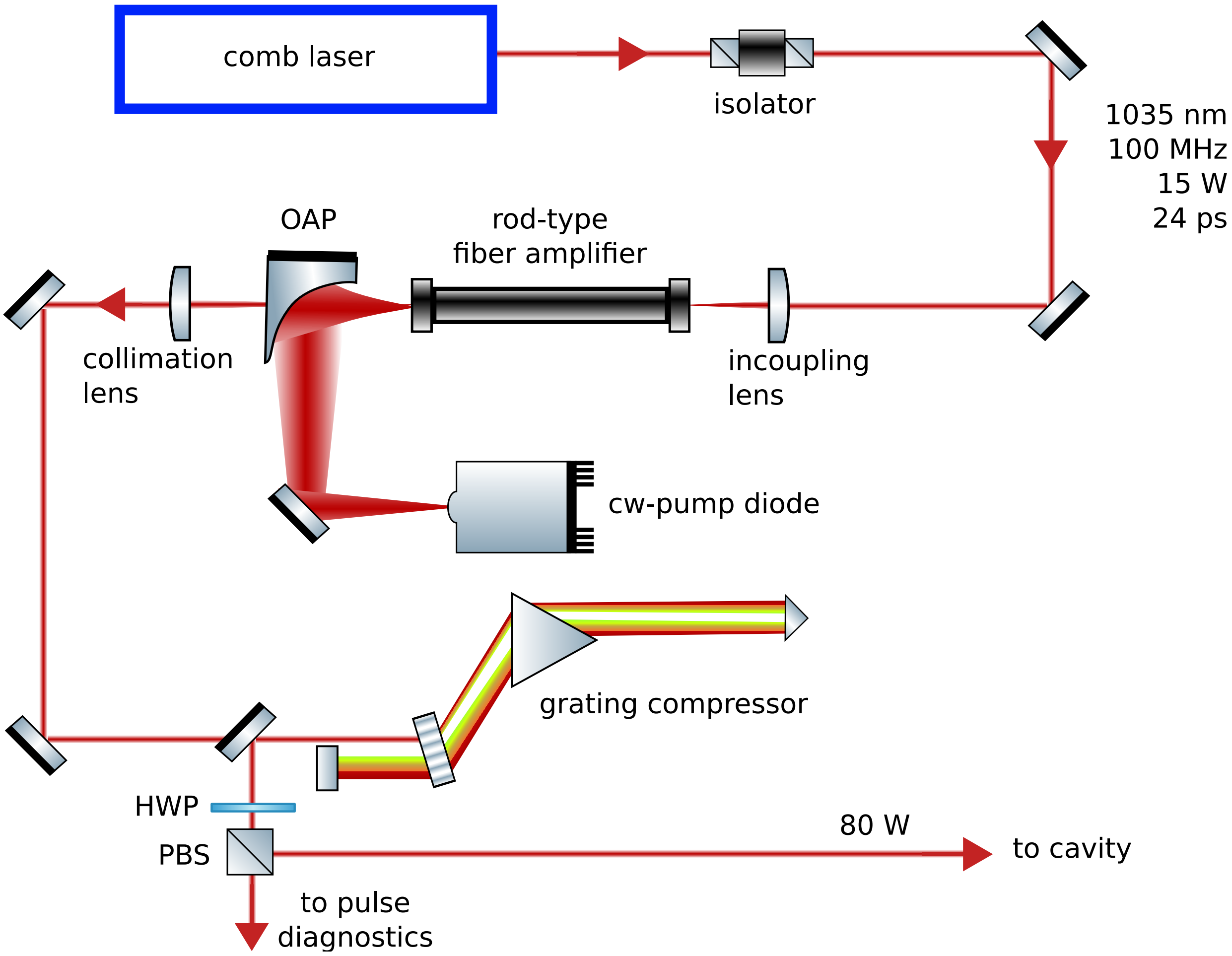

Figure 3.1: Overview of the laser system before the enhancement cavity incoupling. The 24 ps pulses at 10 W average power from the fiber comb are amplified in a diode-pumped active fiber to 80 W and then compressed to about 200 fs in a grating compressor. OAP: off-axis parabolic mirror, PBS: polarizing beamsplitter, HWP: half-wave plate. Adapted from [25].

(1158_28x18_6.35_H, Gitterwerk GmbH) and two retroreflectors which transmit the beam through the grating four consecutive times. These beams are subsequently coupled into the cavity.

Before sending pulses in the XUV cavity, a pulse characterization setup is implemented to measure the amplified, compressed pulses.

3.2 Pulse Characterization

A rotatable waveplate is followed by a polarizing beamsplitter in the path of the laser system just before the cavity. This enables simultaneously measuring the pulses with a small fraction of the overall power while operating the cavity. The measurement of the pulses is done via autocorrelation and frequency-resolved optical gating (FROG, *cf.* 2.6). A FROG system consists of an autocorrelation system followed by a spectrometer, hence both subsystems are described in detail. The pulse characterization system can be operated using an interferometric technique or an intensity-based setup. Thus, both systems and their respective performance are evaluated.

3.2.1 Autocorrelation

The autocorrelation setup consists of a delay stage to split the beam and delay the pulses with respect to each other and a subsequent stage for second-harmonic generation in a nonlinear beta barium borate (BBO) crystal.

Intensity Autocorrelation

The delay stage utilizes an existing setup used in the cavity experiment, originally intended to send counter-propagating pulses into the cavity with adjustable delay. This setup is also used for autocorrelation, as the movable stage offers a fast and precise adjustable delay with absolute reference. The schematics of the beam path are shown in Fig. 3.2(a). A picture of the delay stage operated as intensity autocorrelator is presented in (b).

A high passive stability of the setup is reached because the optical components are mounted on a separate box clamped onto the optical table. Especially the interferometric technique in the next section needs reliable and constant delay of pulses. Hence, the box walls and base plate are made of 5 mm stainless steel which minimizes distortion and vibration. The beam enters the box through a rotatable half-wave plate (HWP1) in

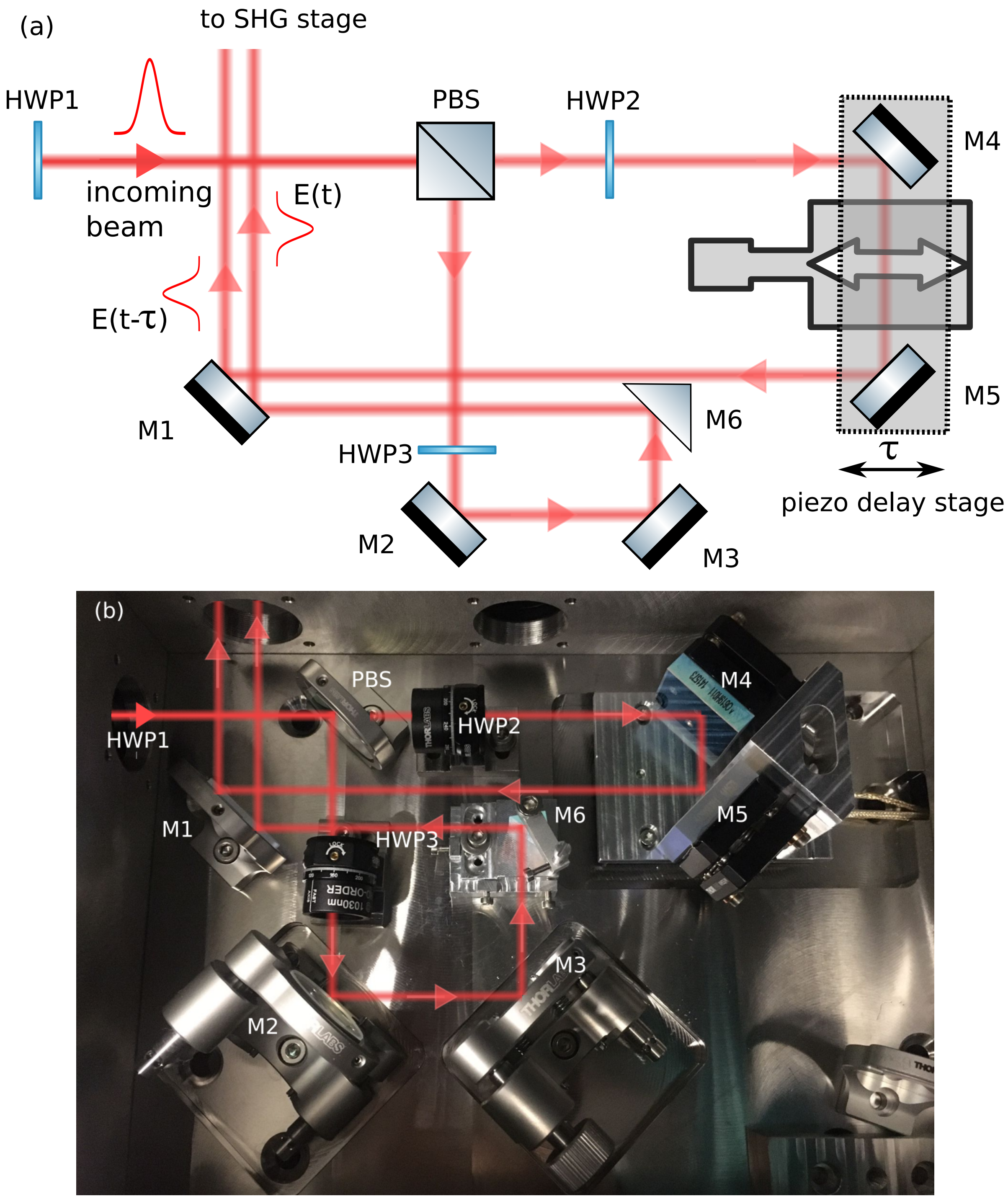

Figure 3.2: (a) Delay stage for intensity autocorrelation with indicated beam path in red. The incoming beam is split with a polarizing beam splitter (PBS). The power in each arm can be adjusted with the first half-wave plate (HWP1) and the polarization is re-paralleled with half-wave plates in each arm (HWP2, HWP3). One pulse travels on a fixed path length along the mirrors M2, M3 and the prism-mirror M6. The other pulse has a variable delay through a retro-reflector consisting of two mirrors (M4,M5) mounted on a piezo delay stage. Both beams are coupled out via the mirror M1. (b) Photograph of the setup with overlayed optical beam path in red and component numbers according to (a).

the sidewall. Afterwards, a polarizing beamsplitter divides the beam in two (PBS). The power in each arm can be adjusted by turning the first waveplate. Additional rotatable half-wave plates in each beamsplitter arm (HWP2, HWP3) allow the re-parallelization of the polarization. This is necessary to prevent unwanted polarization effects in the generation of the second harmonic later on. One half of the beam is subsequently guided onto a retroreflector, consisting of two mirrors (M4, M5, BBSQ1-E03, Thorlabs Inc.). The retroreflector is mounted on a movable stage (Q-545 Q-Motion® Precision Linear Stage, Physik Instrumente (PI) GmbH & Co. KG.) with a maximal movement range of $d_{\mathrm{max}} = 20\,\mathrm{mm}$ and a minimal step size of $\Delta d_{\mathrm{min}} = 10\,\mathrm{nm}$. The time delay τ of the pulse for a movement d of the stage is then adjustable via

$$\tau = \frac{2d}{c}, \tag{3.1}$$

as the pulse travels to the retroreflector and back. The minimal time delay step is therefore $\tau_{\mathrm{min}} = 0.067\,\mathrm{fs}$ and the delay range is $\tau_{\mathrm{max}} = 33.3\,\mathrm{ps}$. This resolution allows sampling of one optical cycle of the light in this setup (3.45 fs) with over 50 data points.

In order to align the second beam parallel to the beam from the retroreflector, it is led on a path of fixed length with with two mirrors (M2, M3) and a prism-shaped mirror M6. The prism-shaped mirror is clamped on a home-built stage which is mounted on two dowel pins in the base plate of the box. This allows faster re-alignment, as the setup is usually operated with different optical components to send counter-propagating pulses into the cavity. The stage can be adjusted with M2 screws and the prism-shaped mirror is mounted on the stage with a home-built clamp.

Both beams are parallel when the second beam passes the prism-shaped mirror on the upper end. Another mirror (M1) guides the beams out of the delay box. A home-built mount with two individual mirrors for each beam outside of the box ensures parallel beams.

Subsequently, the beams are sent onto the stage for frequency conversion via a beam path of over 2 m and various mirrors, enabling precise angular adjustments of the beams due to the long optical path length. A home-built tube shields the laser light which is subsequently sent on a periscope to adjust the height from the delay stage to the height of the optical table.

In the following, a SHG stage (Fig. 3.3) is used for signal generation. The stage is placed on an aluminum breadboard (MB1545/M, Thorlabs Inc.) with 150 x 450 mm^2 footprint. Anodized aluminium plates are bolted on 30 mm item-profiles around the breadboard

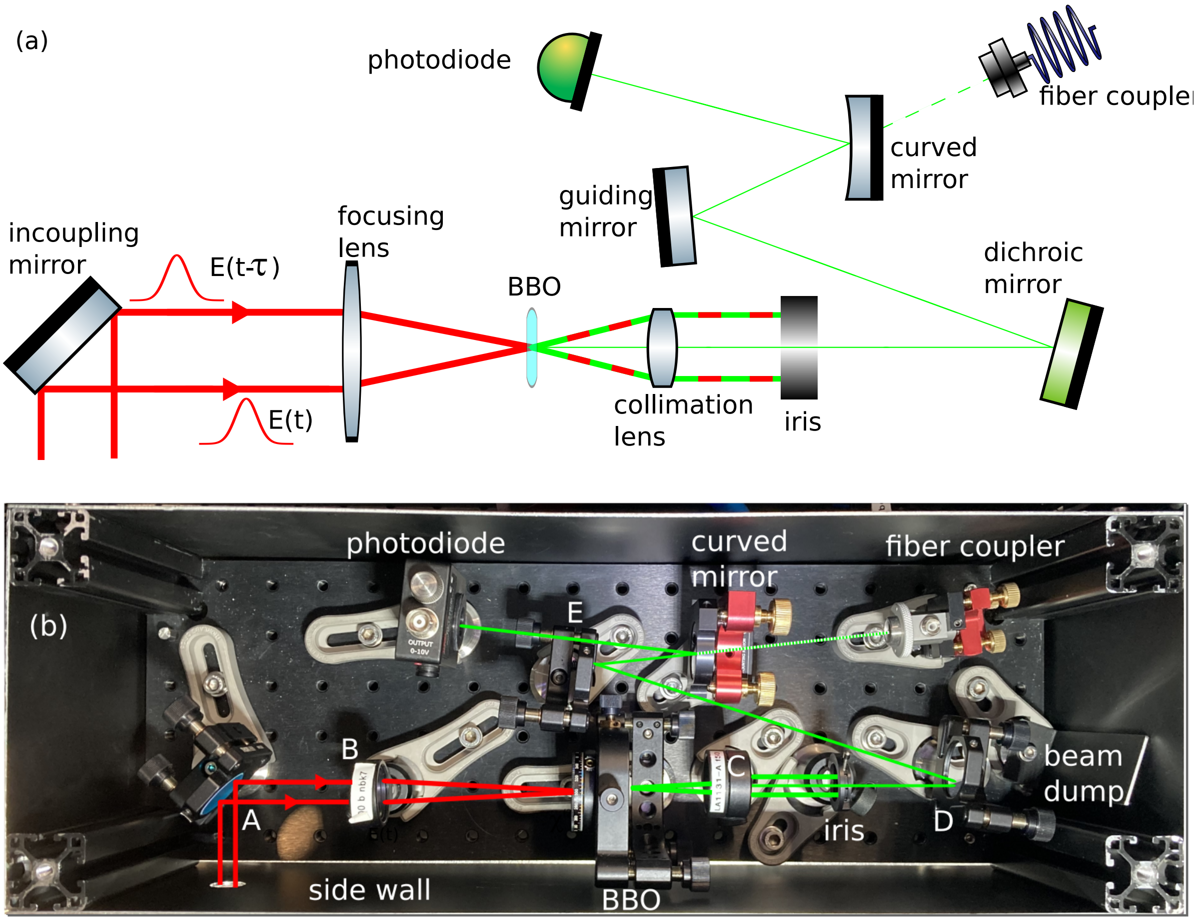

Figure 3.3: (a) Schematic optical setup and beam path of the SHG stage for intensity autocorrelation. (b) SHG stage with housing on a breadboard: (A) incoupling mirror, (B) $f = 100\,\mathrm{mm}$ focusing lens, (C) $f = 50\,\mathrm{mm}$ collimation lens, (D) dichroic mirror, (E) guiding mirror.

as an enclosure for laser safety as well as protection from dust. The laser light enters the box through a small hole in the enclosure. With a mirror (A), the beam is then guided on a lens (B, $f = 100\,\mathrm{mm}$) which focuses it on the BBO crystal. In this rotatable crystal (thickness $d_{\mathrm{BBO}} = 50\,\mu\mathrm{m}$), the second harmonic is generated. A further lens (C, $f = 50\,\mathrm{mm}$) collimates the beam. An iris aides the re-alignment of the setup and blocks the second-harmonic beams generated by the individual uncorrelated pulses. A dichroic mirror ensures that only the second harmonic is evaluated, whereas the remaining infrared light hits a beam dump. Via another mirror (E) the beam hits a curved mirror ($R = 200\,\mathrm{mm}$ which focuses the beam on the responsive area of a photodiode. A magnetic mount allows the curved mirror to be removed and the light is then directly coupled into a fiber for the FROG measurements in the following sections.

Results from intensity autocorrelation are shown in Fig. 3.4. Autocorrelation traces were recorded for different pump currents from 2 A to 7 A (a–e) of the pre-amplifier in the fiber frequency comb, corresponding approximately to output powers of 2 W to 7 W.

The autocorrelation traces exhibit a main pulse with clear side lobes ranging over 1000 fs. For a first estimate of the pulse length, a single Gaussian was fitted. The time range considered for this fit is highlighted in orange, as is the result of the fit. The pulse duration is directly written in the plot. The side lobes suggest a more delicate pulse shape than a single Gaussian. With Fig. 2.11 in mind, fitting a double pulse structure yields a more accurate intensity profile, plotted in green. The values of the side pulse length and distance from the main pulse result in a very long side pulse. Still, the fit does not cover the side lobes in a accurate manner either.

Interferometric Autocorrelation

Therefore, a better estimate of the pulse shape and more information on the phase of the pulse is desirable. The phase may be retrieved with *interferometric* autocorrelation. For an interferometric autocorrelator we use a slightly different setup presented in Fig. 3.5, because the beams of the delayed pulses have to be collinear to interfere. The beam path scheme is drawn in (a), whereas (b) displays a photograph of the actual setup. Apart from replacing the prism-shaped mirror M6 by a second polarizing beamsplitter (PBS2), the setup is identical to the one depicted in Fig. 3.2. As a result, the two beam paths are collinear with two delayed pulses instead of two parallel beams with delayed pulses. This allows to measure the correlation of the electric field with itself instead of the intensity. The dashed beam part in Fig. 3.5 leads to the passive enhancement cavity. Adjusting HWP2 and HWP3 enables switching of the beam path between enhancement cavity and

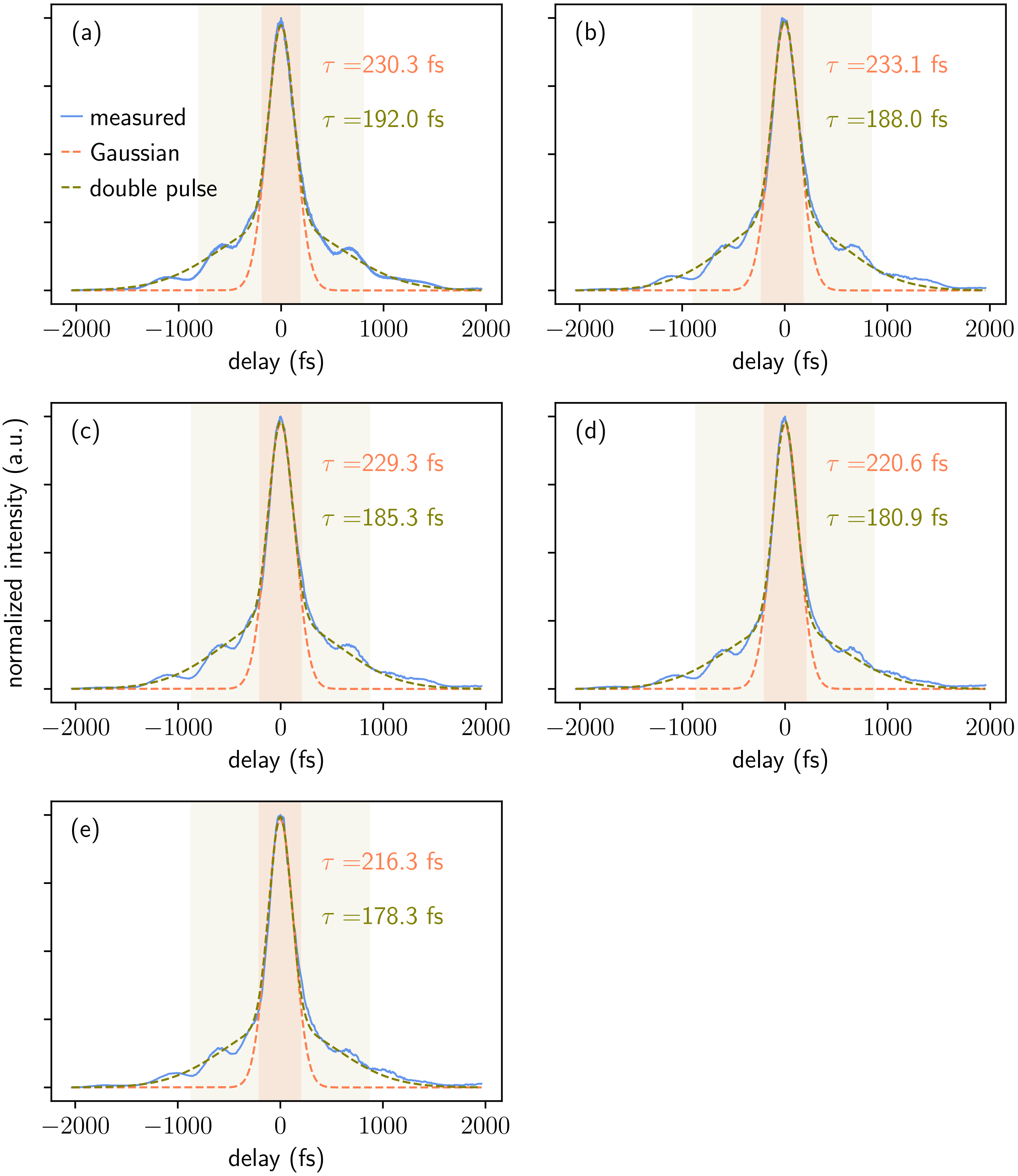

Figure 3.4: Intensity autocorrelation traces in blue with different fit methods: A single Gaussian pulse (orange) and an accompanying satellite pulse in green. The shaded areas correspond to the values considered for the fits. Traces are recorded at pre-amplifier currents of 2 A(a), 3 A(b), 4 A(c), 6 A(d), 7 A(e).

second-harmonic generation stage.

The beam is directed along the same path length of over 2 m to enter the SHG stage. This length allows for a good angular and positional adjustment of the beams. The setup for second-harmonic generation is shown in Fig. 3.6. The optical components are the same as implemented for intensity-based autocorrelation in Fig. 3.3. However, instead of two parallel beams, only a single beam containing both delayed pulses enters the stage. Therefore, the dichroic mirror in this case filters a substantial part of the infrared light out of the signal. The infrared light passes the dichroic mirror unchanged and hits a small beam block, while the green light is reflected at the mirror surface. The green light can again be detected with a photodiode or coupled into a fiber with a fiber coupler.

Fig. 3.7(a) shows an interferometric autocorrelation trace recorded with the described setup. Due to the interferometric oscillation, the plot appears is spaced very densely. Three cycles around zero pulse delay are indicated with all recorded data points in the inset of (a) to make these oscillations visible in detail.

A simple Gaussian fit that considers only the peaks of each cycle results in a pulse width of 208 fs and is plotted in orange. The time area considered for the fit is highlighted in orange.

Again, the trace exhibits side lobes which were already noticeable in the autocorrelation of the intensity, hinting at a pulse that is not described accurately with a simple Gaussian. The structure resembles known signals for pulses with a high third-order dispersion. For comparison, a pulse of 208 fs FWHM with third-order dispersion of 120 fs^3 is plotted in Fig. 3.7(b) for visual comparison to the trace recorded in (a).

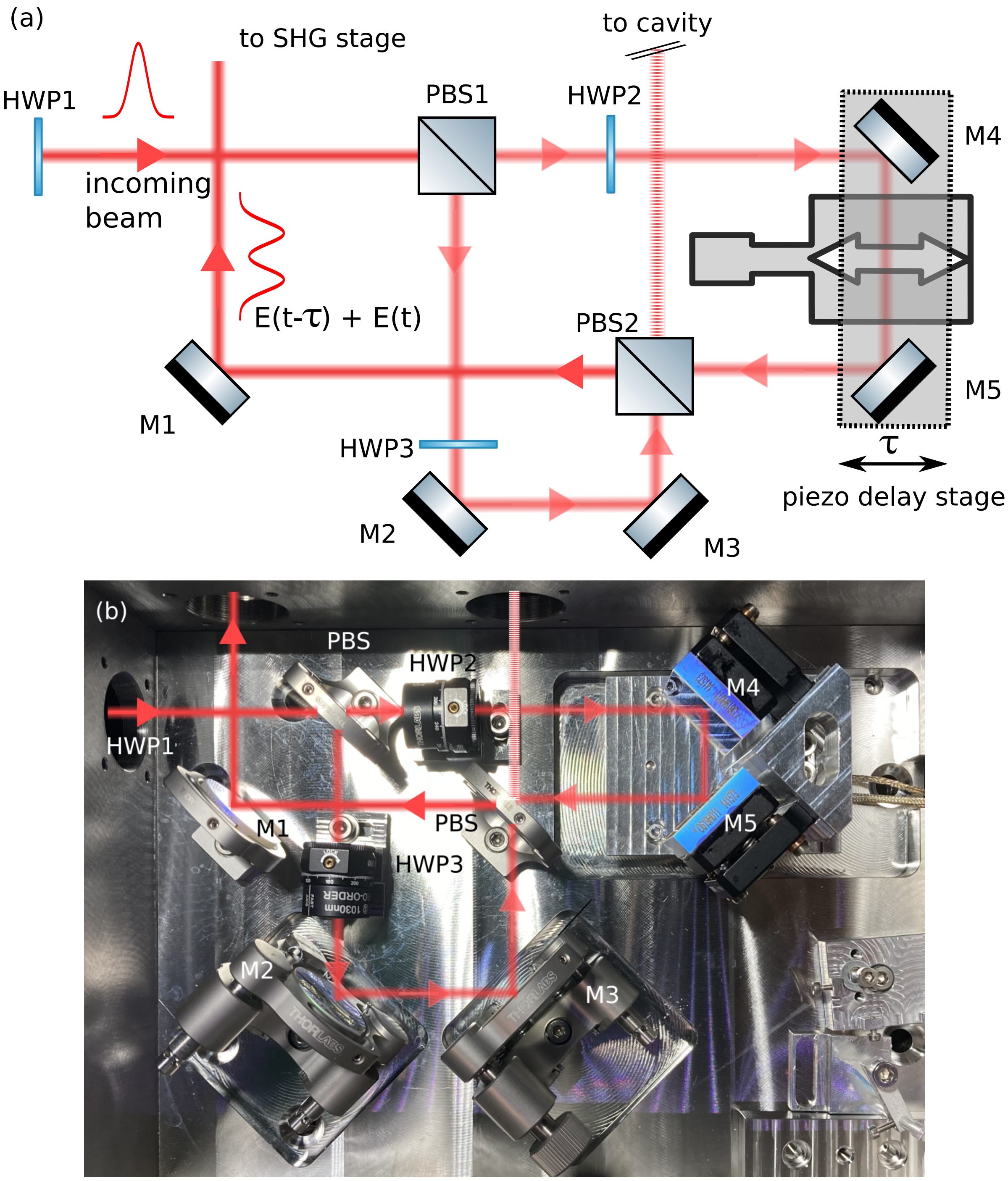

Figure 3.5: (a) Delay stage for interferometric autocorrelation with indicated beam path in red. The beams are aligned collinear instead of parallel compared to Fig. 3.2. The incoming beam is split with a polarizing beam splitter (PBS). The power in each arm can be adjusted with the first half-wave plate (HWP1) and is re-paralleled with half-wave plates in each arm (HWP2,HWP3). One pulse travels on a fixed path length along the mirrors M2, M3. The other pulse has a variable delay through a retro-reflector consisting of two mirrors (M4,M5) mounted on a piezo delay stage. Both beams are overlapped in another polarizing beam splitter and coupled out via the mirror M1 to the SHG stage. (b) Picture of the setup, the beam path is overlayed in red. The enhancement cavity exit is laid out dashed.

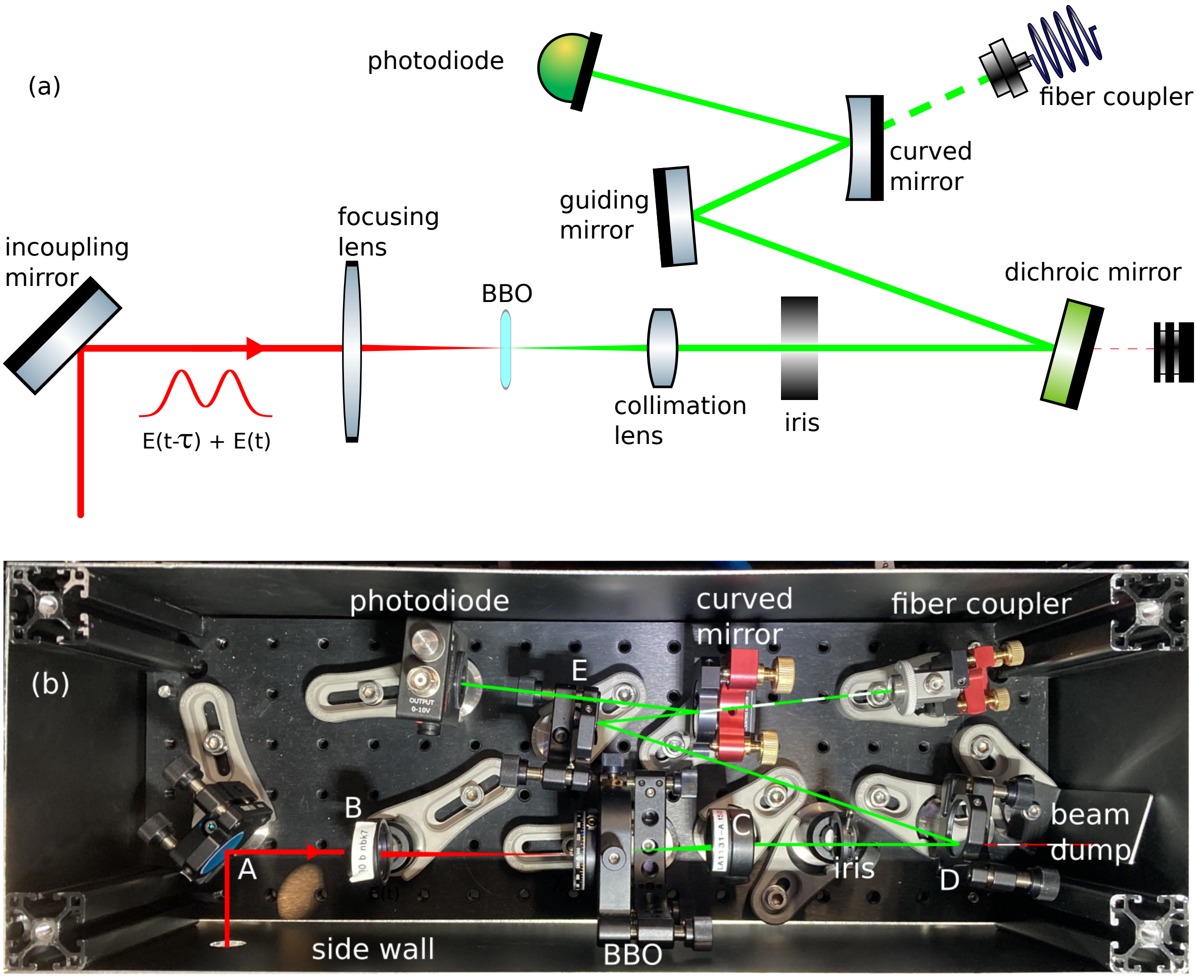

Figure 3.6: (a) Schematic optical setup and beam path of the SHG stage for interferometric autocorrelation. Only a single beam is focused in the BBO crystal for generation of the nonlinear crystal response compared to Fig. 3.3. (b) SHG stage with inhousing on a breadboard: (A) incoupling mirror (B) $f = 100\,\text{mm}$ focusing lens (C) $f = 100\,\text{mm}$ collimation lens (D) dichroic mirror (E) guiding mirror

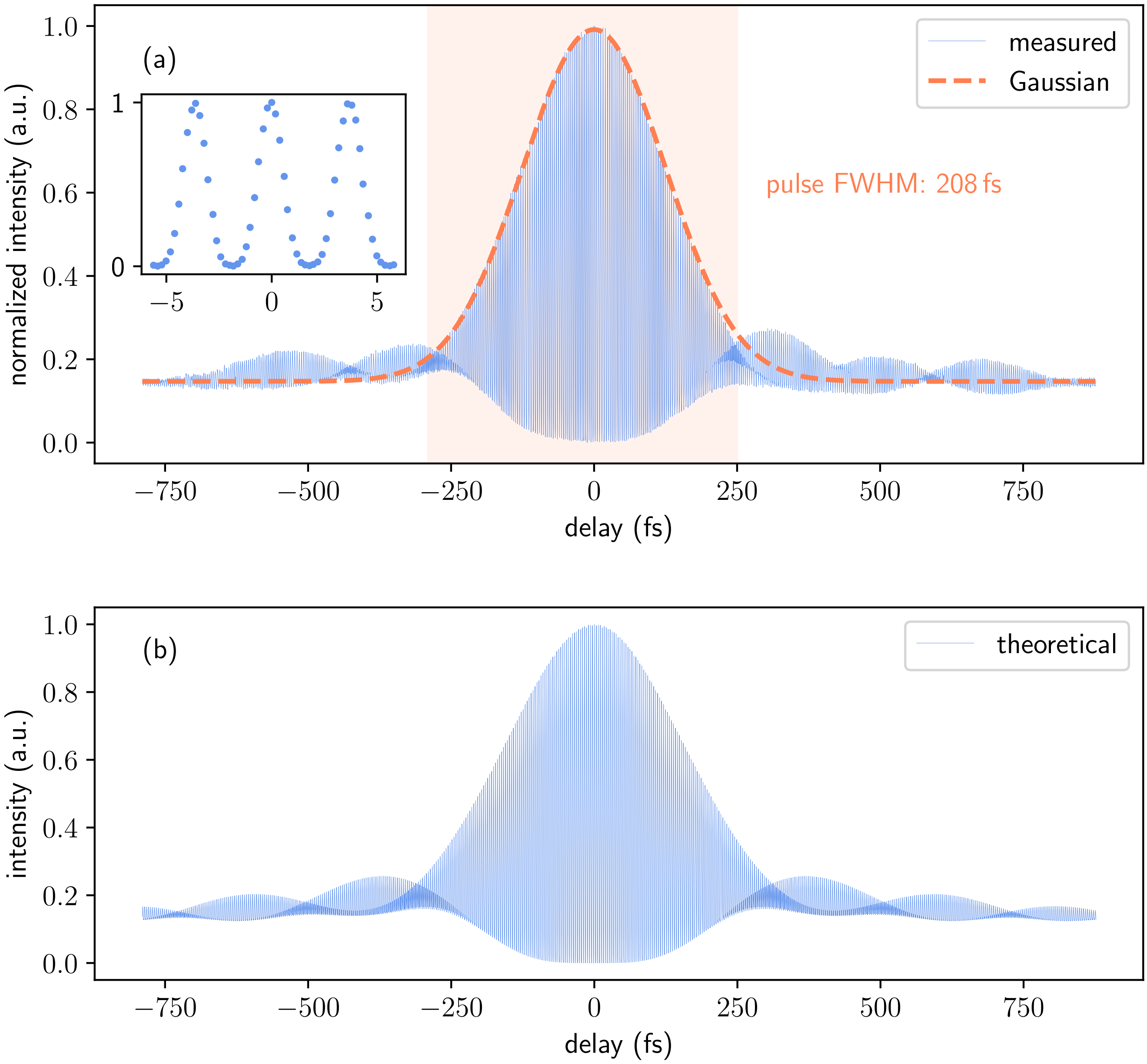

Figure 3.7: (a) Interferometric autocorrelation, recorded at at 7 A pre-amplifier current with a Gaussian fit (orange) on the main pulse. The orange-shaded area marks the area considered for the fit. The inset shows three oscillation cycles around zero delay. (b) Theoretical trace of a pulse with 208 fs FWHM and 120 fs^3 for comparison.

3.2.2 Spectrometer

More information on the pulse than in an autocorrelation setup can be obtained by spectrally resolving the generated second harmonic. Therefore, the laser light is analyzed in a home-built Czerner-Turny-Spectrometer to enable frequency-resolved optical gating. Within the scope of this thesis, a new spectrometer was designed, assembled and commissioned. The spectrometer is located inside a 650x125x500 mm^3 box of aluminium. The beam path along the optical elements can be seen in Fig. 3.8(a). A three-dimensional drawing of the device is shown in (b), whereas (c) shows an actual picture of the spectrometer in the laboratory.

The light is coupled into the spectrometer via a single-mode fiber (P2-460B-PCSMA-1) with 4.2 µm mode diameter. A prism mirror (MRA20-E02, Thorlabs Inc.) guides it through a bandpass filter for green wavelengths (central wavelength $\lambda_c = 520\,\mathrm{nm}$, bandwidth $\Delta\lambda = 40\,\mathrm{nm}$, FBH520-40, Thorlabs Inc.). As the light exits the fiber end divergently (numerical aperture NA = 0.13), a curved mirror (092-0125R-600, EKSMA Optics) collimates the beam. The mirror diameter was chosen to be larger than the beam at the respective position to collect most of the light. The beam diameter b can be calculated by

$$b = \mathrm{NA} \cdot l. \tag{3.2}$$

A propagation length of $l = 300\,\mathrm{mm}$, equalling the focal length f of the mirror, gives a maximum beam waist of $w = 39\,\mathrm{mm}$ at the collimation mirror. The focal length is connected to the radius of curvature ROC of a curved mirror as

$$f = \frac{\mathrm{ROC}}{2}. \tag{3.3}$$

This beam is spectrally resolved at an echelle grating with a line density of $92\,\mathrm{mm}^{-1}$, splitting the beam in its respective wavelengths [73]. The echelle grating is operated at an angle of incidence of about 45°. The diverging color components are collimated by a curved mirror (CM750-500-P01, Thorlabs Inc.) with a focal length of $f = 500\,\mathrm{mm}$ matching the distance between grating and mirror. This mirror focuses each color on a line camera (LC100, Thorlabs Inc.) with 2048 pixels. The camera records a spectrally resolved intensity distribution, i.e. the spectrum, and is controlled via a home-written python library.

Calibration of the lamp is done with a Iron-Neon calibration lamp (P826, Photron Pty Ltd.).

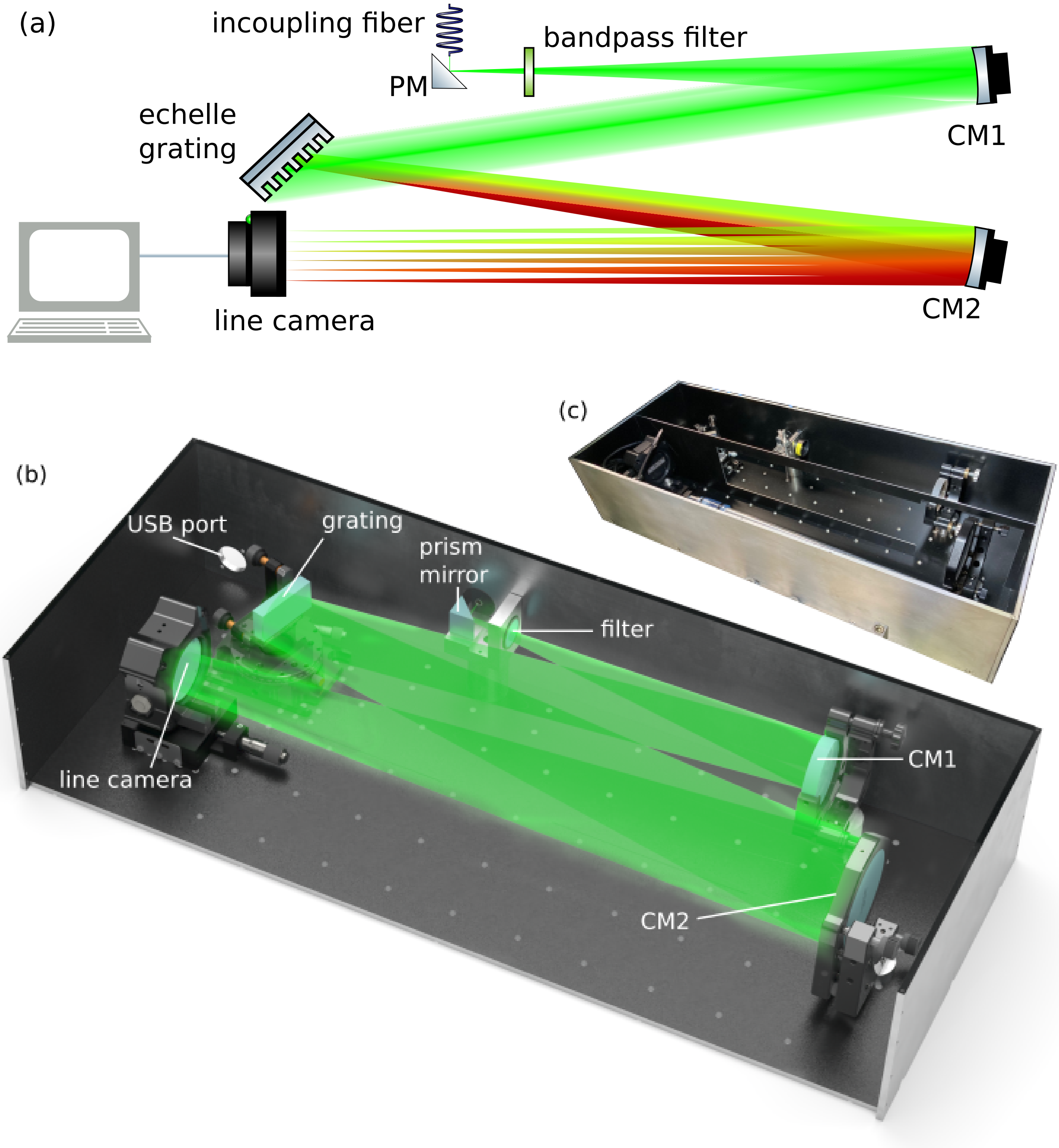

Figure 3.8: (a) Optical setup scheme of the spectrometer. After the incoupling fiber, the beam is guided by a prism mirror (PM) onto a curved mirror (CM1, ROC $= 500\,\mathrm{mm}$) for collimation. The wavelengths are separated at the echelle grating, the second curved mirror (CM2, $R = 600\,\mathrm{mm}$) collimates the beam on the line camera where the spectrum is recorded.

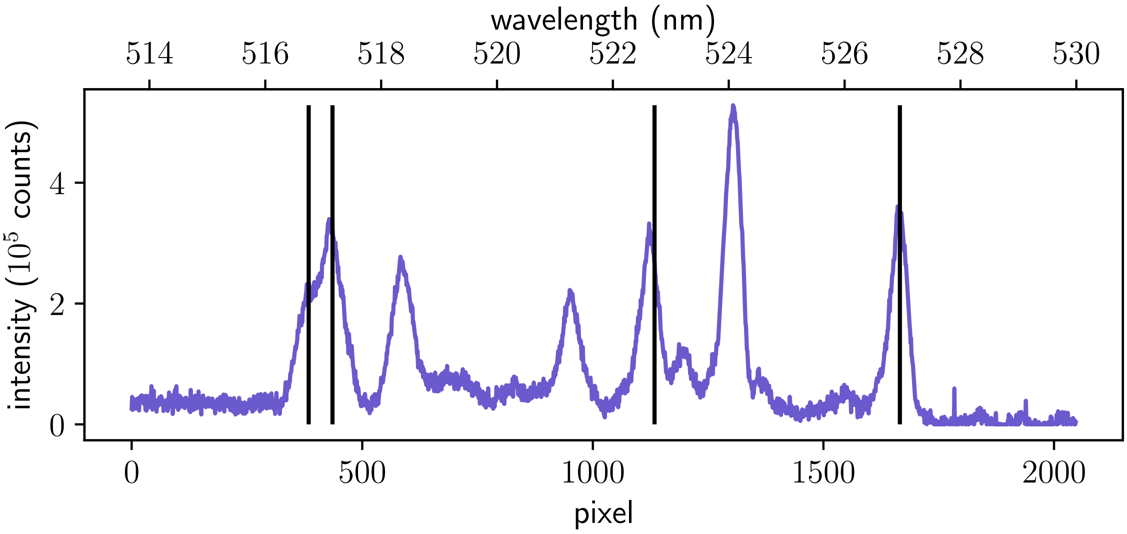

Figure 3.9: Spectrum of a FeNe-Lamp (violet) with indicated iron transitions used for calibration (black). The remaining peaks correspond to neon transitions.

Fig. 3.9 shows the recorded calibration spectrum. Four FeI-transitions at 516.749 nm, 517.16 nm, 522.719 nm and 526.954 nm are identified for the calibration, indicated by black lines in Fig. 3.9. The remaining lines correspond to neon transitions. Due to the bandpass filter, higher order diffraction lines do not need to be taken into account. The remaining peaks correspond to Neon transition lines. The wavelength λ for a given pixel number px is calculated with a second-order calibration function given as

$$\lambda = -1.909 \times 10^{-7}\,\mathrm{nm}^2 \cdot \mathrm{px}^{-2} + 8.352 \times 10^{-3}\,\mathrm{nm} \cdot \mathrm{px}^{-1} + 513.7\,\mathrm{nm}. \tag{3.4}$$

With a different bandpass filter, the spectrometer can easily be operated in the near-infrared regime. This offers a flexible method to measure spectral broadening after the multipass cell directly. The spectrometer offers the ability for higher spectral resolutions when the grating is operated at a higher angle of incidence. For broader spectra, expected from the multipass setup, a broader bandwidth is also recordable by operating the grating at lower angles.

3.2.3 Frequency-Resolved Optical Gating

Combining the aforementioned components, autocorrelator and spectrometer, enables us to fully characterize the pulse by means of frequency-resolved optical gating (FROG) [54, 56, 74]. Light from both autocorrelation setups can be coupled into the spectrometer and a FROG trace is then recorded by saving a spectrum for every delay step.

Intensity Frequency-Resolved Optical Gating

Fig. 3.10 shows intensity-based FROG traces of the pulse in the laser system described in Section 3.1. The colorscale indicates the intensity. Data acquisition time of a trace with a width of 1200 fs with and a step size of 0.33 fs is below 90 s. The temporal system performance is thus improved by a factor of over 20 with respect to a previous home-built setup [75]. FROG traces were recorded for different currents of the amplifier from 2 A to 7 A.

The FROG trace at 7 A is evaluated as in Fig. 3.11 with an adapted version of an open-source FROG retrieval algorithm from S. Kleinert [76]. The script implements an improved version of the 'classical' FROG algorithm, the principal component generalized projects algorithm (PCGPA) [77]. It is based on the same principle as the FROG algorithm described in Section 2.6 with use of an outer product in between the steps.

For pulse retrieval, the raw measured trace needs some corrections for a converging solution of the algorithm. The script subtracts noisy pixels and sets values below a certain threshold to zero. The trace is then centered around the maximum value and symmetrized with respect to the delay to correct asymmetries arising from misalignment. For the algorithm, the trace is then transferred from the wavelength to the frequency domain. The central wavelength λ_c, the spacing between pixels $\Delta\lambda$ and the delay step width $\Delta\tau$ need to be entered manually. The spectrum recorded at zero delay is, by a Fourier transform to the time domain with zero phase, the intial guess for the retrieval algorithm.

Fig. 3.11(a) shows the retrieved spectrum (blue) and spectral phase (brown). The bandwidth of the spectrum is in line with the manufacturer-specified bandwidth of 7 nm centered around 1039 nm. However, the spectral phase does not confirm the supposition from interferometric autocorrelation of a substantial third-order dispersion. Fig. 3.11(b) shows the retrieved intensity profile (blue) and phase (brown). The FWHM length is 103 fs and thus lower compared to the expectations from previous measurements by a factor of two.

The trace and the retrieved theoretical trace is displayed in (c) and (d), respectively. The experimental trace appears different compared to Fig. 3.10(e) as the intensity is plotted on a logarithmic colorscale. The agreement between experimental and retrieved trace is rather low. Therefore, a conclusion on the pulse shape is not yet possible with

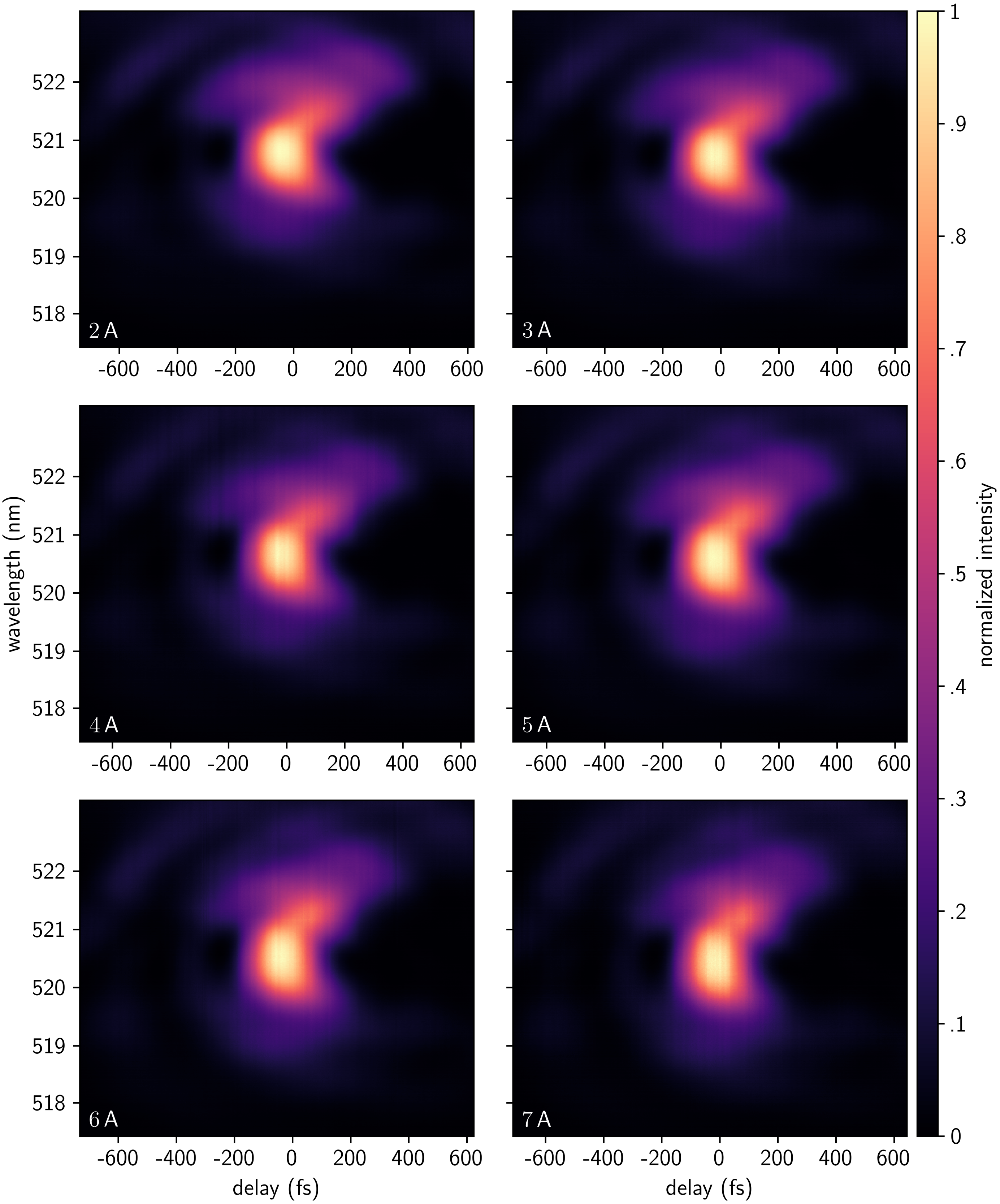

Figure 3.10: Intensity-FROG traces, recorded at different operating currents of the amplifier from 2 A to 7 A.

this approach. The traces are not symmetric with respect to zero delay, as they should inherently be, making it difficult for the algorithm to deliver a reasonable result. A limiting factor in the experimental setup was parallel alignment of the beams, an improved optomechanical setup for adjustment of the prism mirror (M6, Fig. 3.2) is already being worked on.

Interferometric Frequency-Resolved Optical Gating

The interferometric autocorrelation signal is also spectrally resolved for an interferometric frequency-resolved optical gating (iFROG) setup [78]. The recorded trace is shown in Fig. 3.12(a) with a colorscale indicating the intensity. The white frame is plotted in more detail in (b) to show the interferometric structure. The trace appears more symmetric with respect to delay than the intensity-FROG traces.

Evaluation of the iFROG trace could yield a more reliable retrieval of the pulse shape, as already the interferometric autocorrelation revealed a third-order dispersion in the pulse. This could, e.g., be done with an adapted version of the common pulse retrieval algorithm (COPRA) [79]. This was not considered before as we under-estimated the accuracy of this measurement method based on the results from interferometric autocorrelation.

Further improvement of the setup could be achieved by the use of a 50:50 beamsplitter instead of a polarizing beamsplitter as small changes in the alignment of the waveplates had substantial effect on the recorded traces. Furthermore, movement of the delay stage changes the pointing of the beam, yielding unwanted geometrical effects on the recorded traces. The recorded traces in the interferometric setup appear to be more promising, although recording of interferometric traces takes longer (about 30 min) as the interferometric structure needs to be sampled with enough detail.

The intensity autocorrelation gave a first estimate of the pulse shape. The pulse cannot be described as a simple unchirped Gaussian. Yet, an estimate of the pulse duration of about 220 fs can be extracted. Intensity-based FROG did not lead to a satisfying retrieval of the pulse shape with the adapted version of a publicly available retrieval algorithm due to asymmetry of the—inherently symmetric—traces. An improved optomechanical alignment is subject to a consecutive thesis. The interferometric FROG traces could prove a valid candidate for a reliable pulse shape retrieval with a algorithm capable of retrieving the pulse shape from such a trace at full available laser power.

An improved optomechanical setup will enable characterization of the pulses after the fiber amplifier in full operational mode of the enhancement cavity at over 80 W as well as measurements of pulse compression and spectral broadening after the multipass cell.

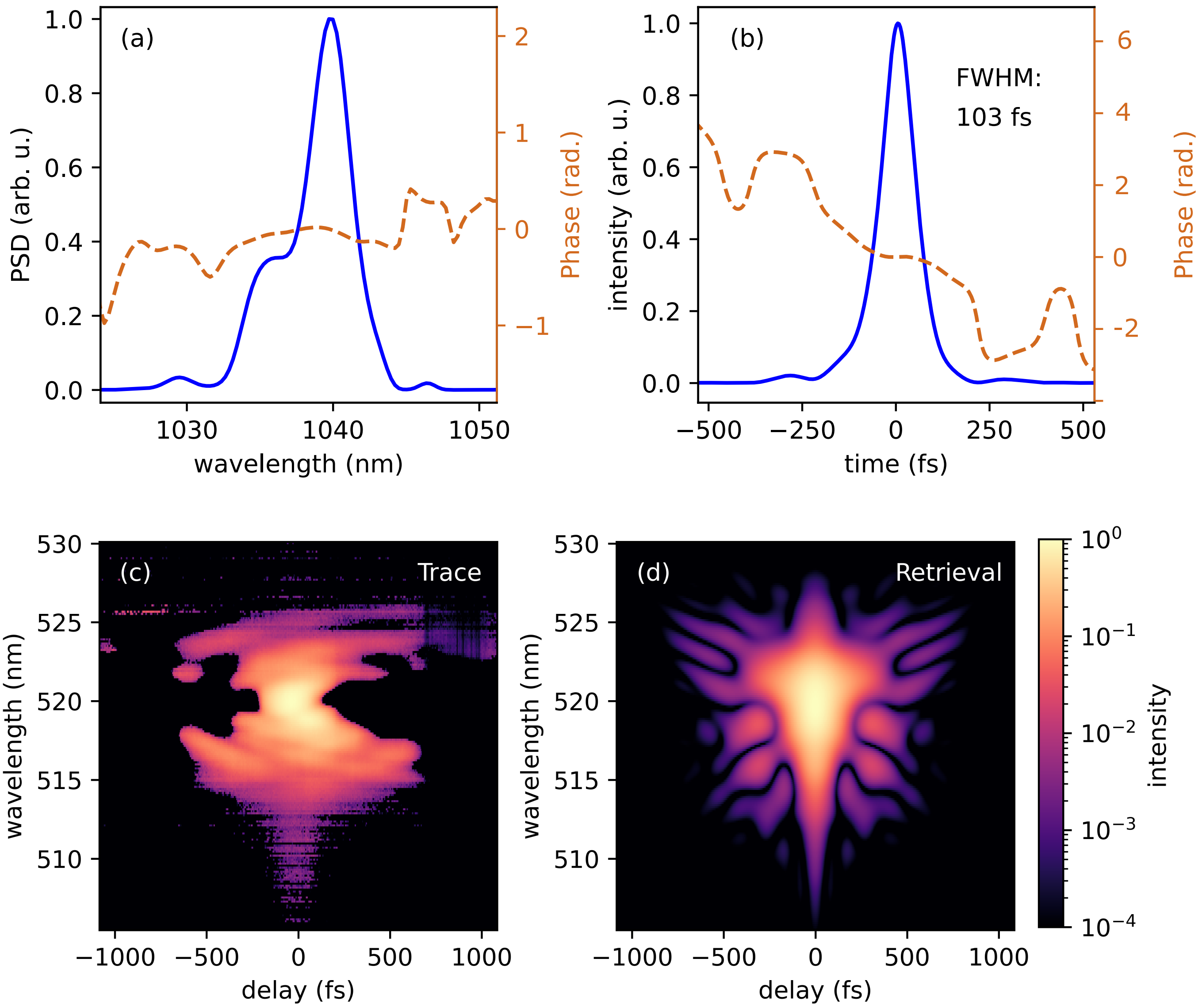

Figure 3.11: Pulse retrieval result for the FROG trace recorded at 7 A amplifier current. (a) Spectrum (blue) and spectral phase (brown) (b) Temporal Intensity (blue) and temporal phase (brown). (c) Symmetrized, background-corrected recorded trace. (d) Retrieved trace.

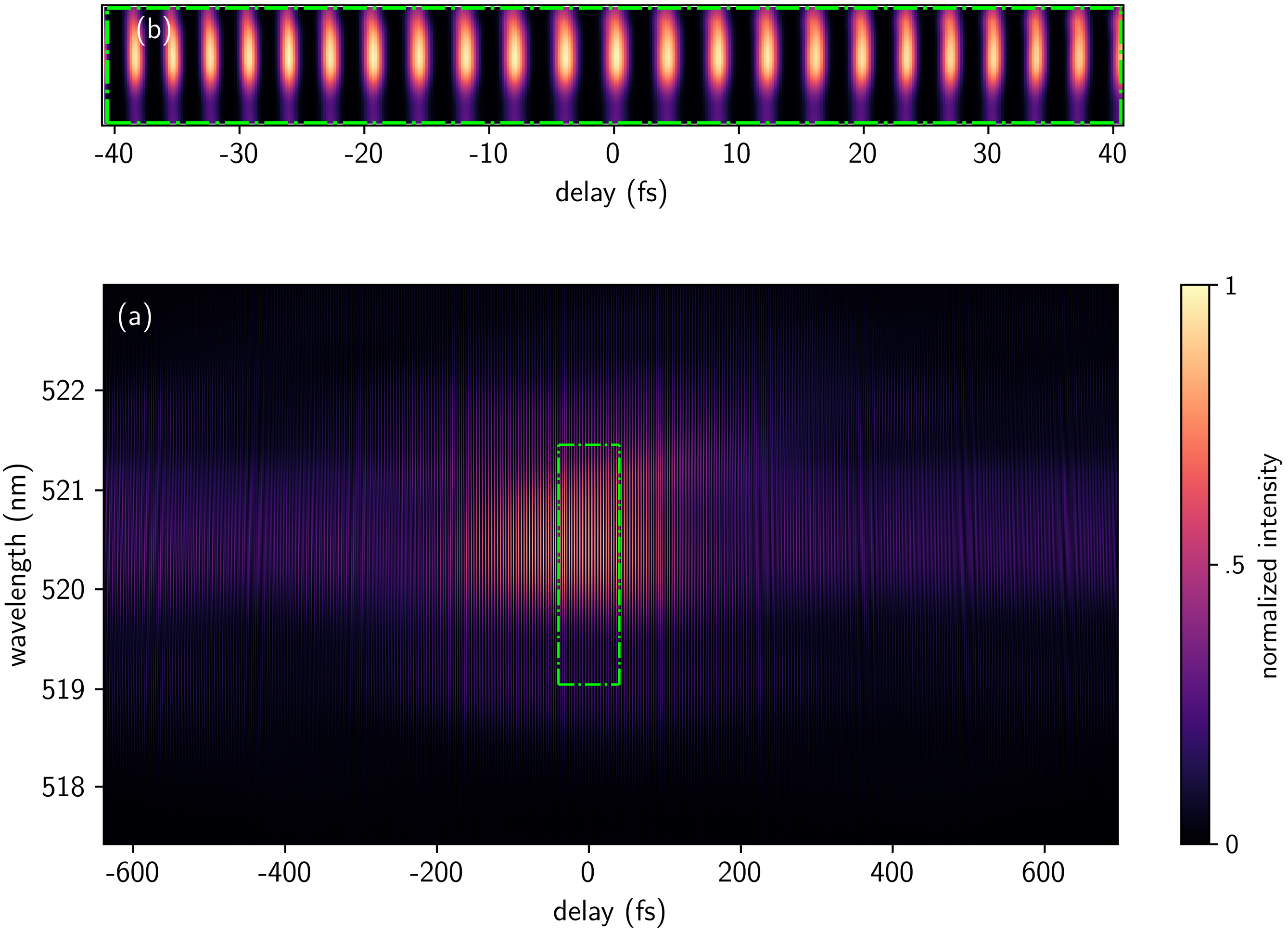

Figure 3.12: (a) Interferometric FROG trace at 7 A current at the amplifier. The white box marks the detail shown in (b) for better visibility of the interferometric structure.

4 Nonlinear Pulse Compression Multipass Cell

For a higher yield of HHG generation, better temporal resolution in general and a broader frequency range in the XUV, it is beneficial to compress the pulses of the frequency comb temporally by broadening them spectrally and compensating the dispersion. The laser system described in Section 3.1 yields constraints on the design of such a setup. The average power is over 75 W at full amplification and the repetition rate of the fiber comb is 100 MHz. This results in an energy of 0.75 µJ per pulse. For an estimated pulse duration of 220 fs, this accumulates to a peak pulse power of 3 MW.

4.1 General Setup

There are several methods in use for nonlinear pulse compression. For a more detailed discussion see Chapter 2.7. As the nonlinear phase shift scales proportional to the nonlinear index n_2 of the material and the intensity I, it is crucial to have a highly nonlinear material and a high intensity. A feasible way of reaching high intensities lies in confinement of the light into a waveguide. This reduces the mode area of the beam, increasing the intensity. Such a waveguide may be a hollow-core photonic crystal fiber (HC-PCF), which can handle high input powers [80] as found in this experiment. Nonlinear effects can be accumulated by a gas filling of the hollow core [81]. However, the costs of these fibers are rather high.

Conventional fibers with fused silica (FS) as nonlinear material enable high intensities and even higher nonlinearites. However, the handling of fibers is difficult at common output powers of the frequency comb laser. It is already highly problematic to couple more than 50 W into a fiber since minor misalignment or contaminated end facets lead to burning and destruction of the system. Even with endcaps, delicate larger structures spliced on the fiber end that guide the light in the fiber, this is still unreliable to operate. Long-term stability and reliability is a key aspect for the operation of the enhancement cavities to enable continuous and extensive measurements. The implementation of very

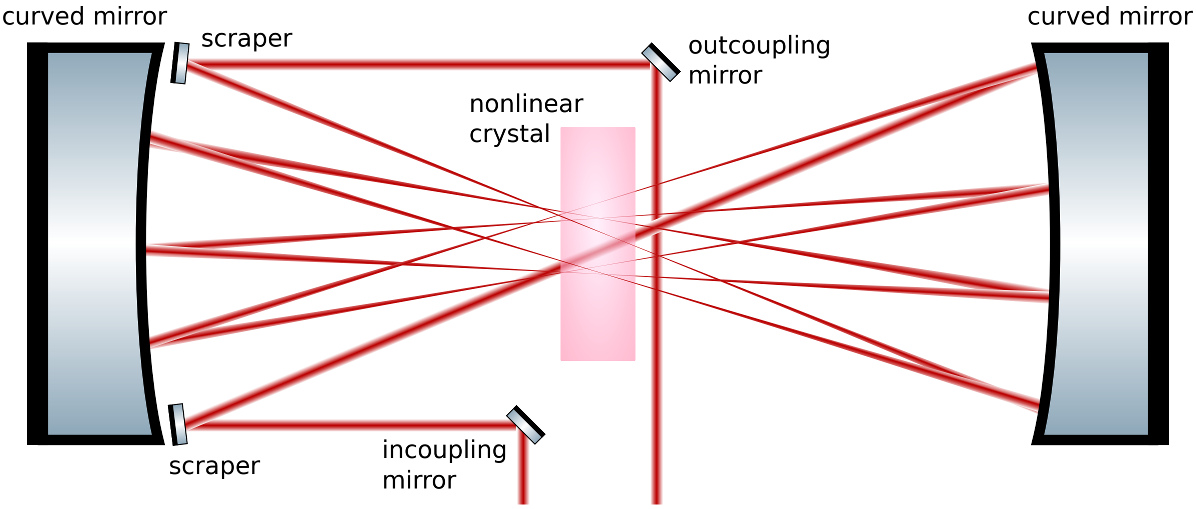

Figure 4.1: Optical setup of a multipass cell for nonlinear pulse compression. The laser beam is coupled in with an incoupling and a scraper mirror and advances between the curved mirrors. The beam is focused in the middle of the cell after reflection on a curved mirror. The nonlinear material is placed in the focus of the mirrors. The beam is coupled out with another scraper and an outcoupling mirror.

large mode area fibers ($> 100\,\mu$m mode diameter) is over and above that hindered by their non-commercialization [82].

Spectral broadening was recently demonstrated in a multipass cell with a setup as depicted by Fig. 4.1. The beam is reflected back and forth between two curved mirrors and the nonlinear phase shift is generated in a bulk material placed in the focus [28].

4.2 Geometric Considerations

A free parameter in the design of a multipass cell is the focal length f of the curved mirrors with radius of curvature R on both ends. It determines the distance between the two mirrors l as

$$l \geq 2R = 4f. \tag{4.1}$$

As the curved mirror focuses the beam, it also affects the size of the beam waist at the nonlinear element site in the middle of the cell. Typical values for the radius of curvature R in current research span from $R = 200$ mm to $R = 300$ mm [29, 30]. Mirrors with lower focal length are more prone to instabilities as the optical path length is decreased, making correct alignment of the beam path difficult. A compromise of alignment simplicity and

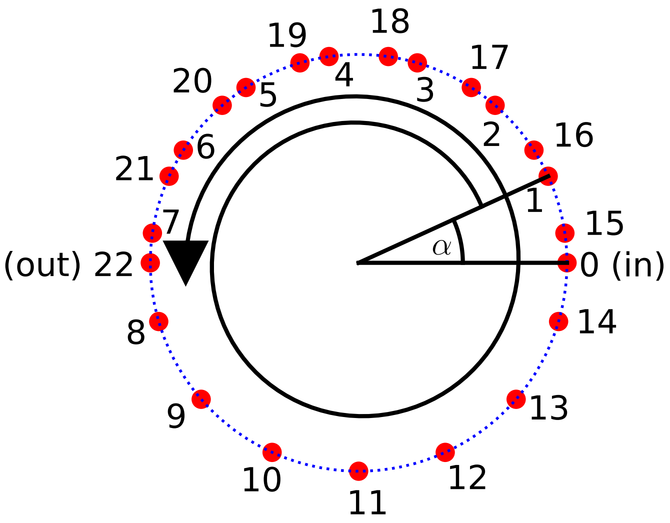

Figure 4.2: Pattern of the beam spots (red) on the mirror of a Herriott cell for 22 passes. The spots lie on a circle (blue). The numbers indicate the number of passes in the cell that have already taken place. An angular advance α between each pass gives 3π total angular advance.

footprint reduction in the space-restricted portable XUV comb lab are curved mirrors with a curvature of $R = 250\,\mathrm{mm}$ (025-8025, EKSMA Optics).

Multipass cells are usually designed as Herriott-type cells where the propagation of the beam between the mirrors lies on a hyperboloid. The spot pattern on the mirrors of such a cell is displayed in Fig. 4.2. With each propagation the beam advances an angle α and has in total n reflections. After a total angular advance of $m\pi$, the beam is coupled out again. One can show that the q-parameter of the beam is conserved for

$$n\alpha = m\pi; \qquad m, n \in \mathbb{N}, \tag{4.2}$$

i.e. when the beam is coupled out after a multiple integer of π [70].

The beam waist is minimal at the nonlinear element. An estimation of this beam waist size is possible with Gaussian beam propagation. Fig. 4.3 shows the beam profile of the experiment at the position of the proposed laser setup measured with a beam profiler (BP209-VIS/M, Thorlabs Inc.). The values for an $1/e^2$ decrease of the beam size are recorded in Table 4.1. The beam has a beam quality factor M^2 lower than 1.2. In the calculation, the beam diameter is thus averaged to an uni-axial diameter of $2\,\mathrm{mm}$. The calculation is performed with the open-source software GaussianBeam [83]. The minimal

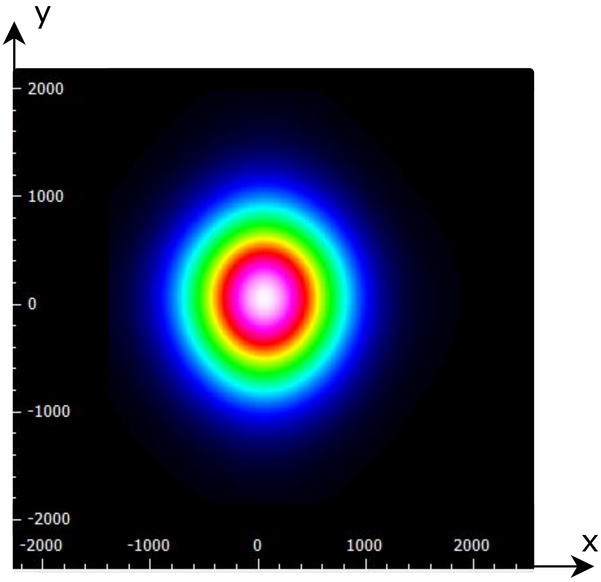

Figure 4.3: Beam profile measurement before entering the cavity. White-red-green-blue-black marks higher-to-lower intensity.

axis	diameter (µm)
x	1943.9
y	2168.3

Table 4.1: Beam widths of Fig. 4.3 at $1/e^2$ of the maximal intensity.

beam waist for a wavelength $\lambda = 1039\,\mathrm{nm}$ is $w_0 = 20.7\,\mu\mathrm{m}$ and the Rayleigh length is $z_\mathrm{r} = 1.3\,\mathrm{mm}$.

4.3 Simulation Results

The scheme of the implemented algorithm for the simulation of light-matter interaction in the multipass cell is shown in Fig. 4.4. The algorithm propagates any initial pulse shape through the cell in iterative steps. In (a), one back- and forth reflection between the mirrors (grey) is displayed which is referred to as one *pass* in the following. The number of passes can be chosen freely. The algorithm starts by propagating the pulse shape through the nonlinear material. After that, dispersion from the propagation in air—or any gas—and by reflection on the mirrors is added to the pulse by multiplying the electric field in the frequency domain with the phase factor $e^{i\phi}$. The phase is calculated as

$$\phi(\omega) = \frac{1}{2}R\beta_{2,\mathrm{air}}(\omega-\omega_0)^2 + \frac{1}{3}R\beta_{3,\mathrm{air}}(\omega-\omega_0)^3 + \mathrm{GDD}_\mathrm{mirror}, \tag{4.3}$$

where the β coefficients are the values for group velocity dispersion. $\mathrm{GDD}_\mathrm{mirror}$ is the possible group delay induced by a chirped mirror. Dispersion values for air are taken

parameter	symbol	value
central wavelength	λ_0	1039 nm
pulse length	τ	220 fs
pulse energy	E_p	0.7 µJ
beam size	w_0	80 µm

Table 4.2: Simulation parameters for optical multipass cell design.

from [84]. Nonlinearities in air are neglected as they are two orders of magnitude smaller compared to the crystal nonlinearity [85]. Furthermore, the beam is only focused in the center of the cell. This results in even smaller nonlinearities in air due to the wider beam diameter. For the back-reflection, the pulse is again propagated through the nonlinear material and then dispersion from the air and the mirrors is added. The output fields in time and frequency domain of each pass are stored in a .sim-file.

The propagation in the nonlinear material is based on the publicly available repository 'gnlse' [86]. The code incorporates a solver for the generalized nonlinear Schrödinger equation (GNLSE). This equation is an extension of the nonlinear schrödinger equation for short few-cycle laser pulses [87]. Effects such as Raman scattering and self-steepening are included in this ordinary differential equation that is solvable with tools from the scipy-library. The python algorithm is based on the MATLAB script described by Dudley *et al.*[88] which uses the split-step Fourier method.

The split-step Fourier method can be understood as follows: The propagation distance is split up in small increments dz (Fig. 4.4(b)). In each increment, effects in the frequency domain (dispersion) and in the time domain (nonlinearities) are considered consecutively. The Fourier transform ensures consistency in the time and frequency domain in each step as the effects are modeled in both domains (see Fig. 4.4(c)).

As the simulation was originally intended for use in optical fibers, spatial alterations of the beam due to self-focusing is not taken into account. This approximation is justified as the thickness of the nonlinear material ($< 3\,\text{mm}$) in the cell is comparable to the Rayleigh range. Thus, variation of the beam profile over one propagation is negligible.

Pure spectral broadening in bulk KDP was simulated to estimate the validity of the simulation results. Qualitative measurements of the spectral change by propagating the laser beam of the experiment in bulk KDP verified the simulation results. These measurements have shown that the beam waist size is under-estimated. Hence, the beam waist size has been adapted to 80 µm in the simulation. The parameters used in the cell simulation are recorded in Table 4.2.

The pulse shape considered in the simulation is Gaussian, the pulse length τ refers to the

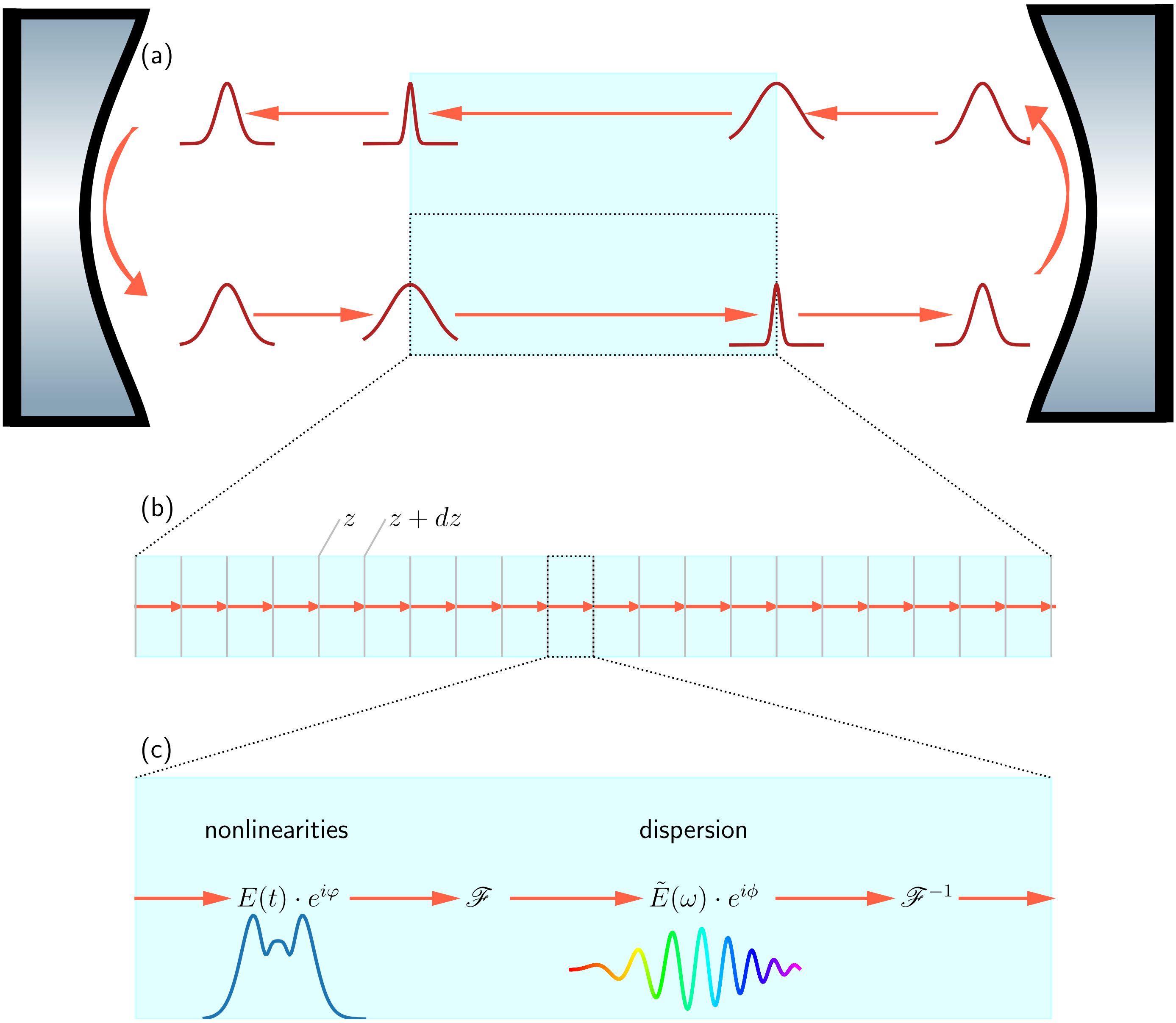

Figure 4.4: Working principle of the multipass cell simulation: (a) The pulse is propagated through a pair of curved mirrors with a nonlinear material and gas in between. Dispersion is added at each reflection on the mirrors and for propagation in gas. Nonlinearities are only considered in the crystal in the following manner: (b) The crystal length is split up into small increments. (c) In each increment, the nonlinearities in the time domain and dispersion in the frequency domain are added consecutively. The Fourier transform connects time and frequency domain.

Gaussian FWHM. The pulse energy $E_p = 0.7\,\mu\mathrm{J}$ (corresponding to 70 W average power) was estimated with a margin to the maximum pulse energy of $0.8\,\mu\mathrm{J}$ (corresponding to 80 W average power) to ensure compression even if the average power of the system is decreased.

Different materials are evaluated for pulse compression. The material used in bulk nonlinear pulse compression multipass cells is, to the best of our knowledge, exclusively fused silica. However, the self-focusing threshold for fused silica lies above 4 MW [28, 30]. It can be calculated by [89]

$$P_{\text{crit}} = \frac{0.148\lambda^2}{n n_2}. \tag{4.4}$$

As the peak power in the system lies below 3 MW, an approach with fused silica is not feasible. This was also verified in the simulations.

Hence, the use of different materials is necessary to achieve sufficient nonlinearities for spectral broadening. (4.4) suggests the choice of a material with a higher nonlinear index. Yttrium aluminium garnet (YAG) has a nonlinear index of $n_2 = 6.13 \times 10^{-20}\,\mathrm{m^2\,W^{-1}}$, resulting in a self-focusing threshold of $P_{\text{crit}} = 1.41\,\mathrm{MW}$. The peak power in the system exceeds the threshold and nonlinearities can broaden the spectrum and shorten the pulse.

However, YAG has a substantial normal group velocity dispersion around 1030 nm of $\beta_{2,\text{YAG}} = 66.675\,\mathrm{fs^2\,mm^{-1}}$. Hence, a multipass cell with YAG needs chirp removal inside the cell. Otherwise, the dispersion broadens the pulse in the time domain stronger than the nonlinearities compress it and the peak power might even fall below the self-focusing threshold. A configuration of chirped mirrors with $90\,\mathrm{fs^3}$ GDD for a crystal thickness of 2 mm has delivered the best theoretical compression results. For a low number of passes, the chirp could be removed after the propagation in the cell. The number of passes without immediate chirp removal is limited by the propagation step at which dispersion has lowered the peak power below the self-focusing threshold.

The result of this setup is presented in Fig. 4.5. The time domain is shown in (a) with the incoming Gaussian pulse in orange and the outgoing pulse in blue. The compression is clearly visible and the peak power is increased from under 3 MW to over 5 MW. The spectral broadening is depicted in (b), where the input spectrum (orange) is broadened to a spectral range of over 150 nm. The bottom row (c,d) shows the evolution over the number of passes. Fig. 4.5(c) shows that the dispersion compensations through the chirped mirrors allow compressed pulses in each pass whereas in (d) the increasing spectral broadening over the number of passes is depicted.

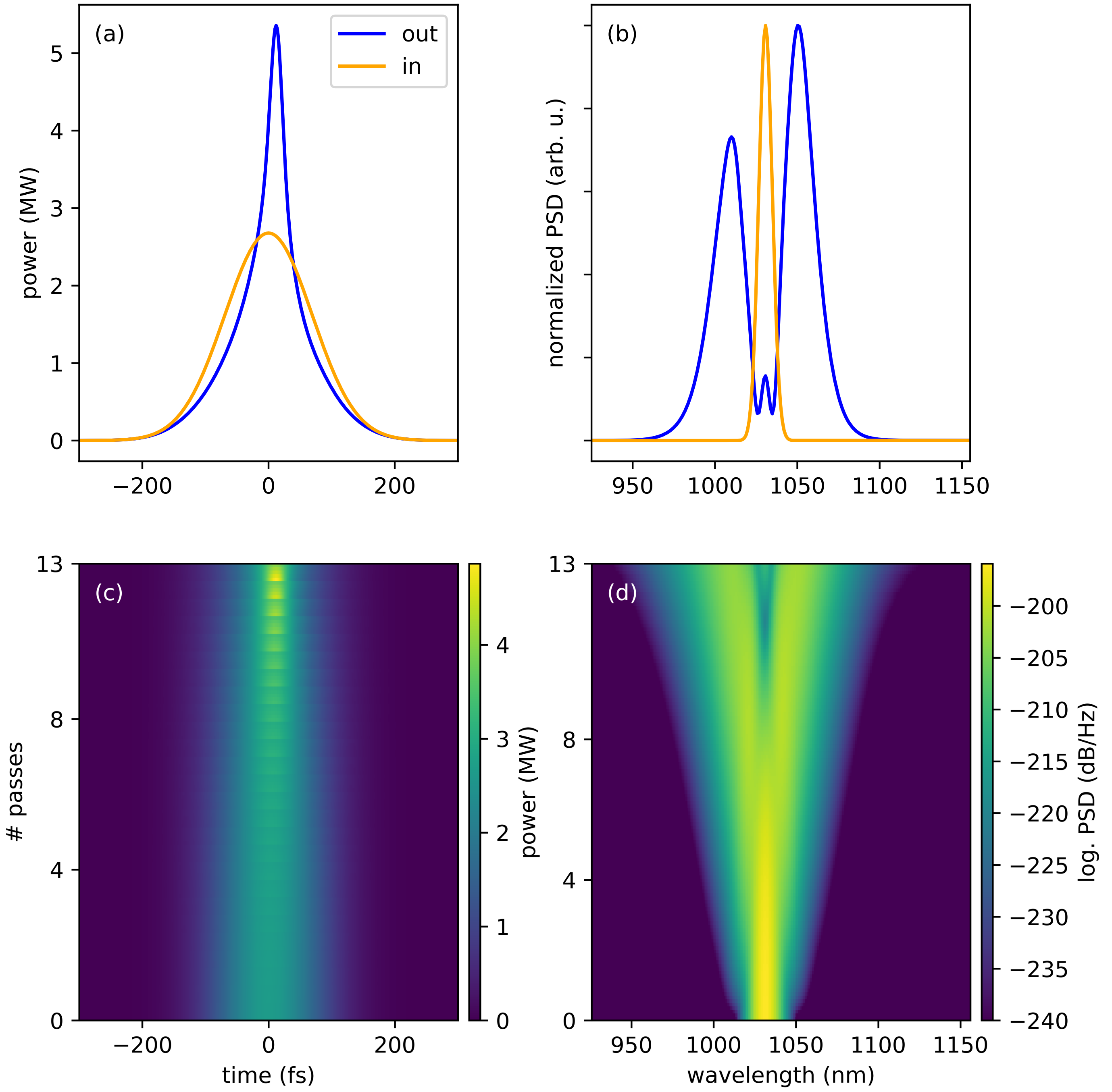

Figure 4.5: Simulation result of a multipass cell with 13 passes through 2 mm YAG as nonlinear material and chirped mirrors of 90 fs^2 on each side. (a) The incoming pulse (orange) is shortened from 220 fs FWHM to 49.8 fs pulse length (blue). (b) The incoming Gaussian spectrum is broadened from 7 nm FWHM to over 150 nm bandwidth. (c) The continuous compression of the pulse over the number of passes, because dispersion is compensated in every step by chirped mirrors. (d) Spectral broadening over the number of passes plotted on a logarithmic power spectral density (PSD) colorscale.

The systems are evaluated with respect to the compression factor $\eta = \tau_{\text{in}}/\tau_{\text{out}}$, which compares the length of the outgoing pulse τ_{out} with the incoming pulse length τ_{in}.

As the dispersion is nearly compensated in every step, the setup with YAG and chirped mirrors allows a compression factor of $\eta_{\text{YAG}} = 4.4$. The use of chirped mirrors in such a setup is however difficult as they are expensive and tedious to handle.

A different approach is the use of potassium dihydrogenphosphate (KDP) as nonlinear material. It has a nonlinear index of $6.54 \times 10^{-20}\,\text{m}^2\,\text{W}^{-1}$ [90], resulting in a self-focusing threshold of $P_{\text{crit}} = 1.61\,\text{MW}$. A valuable property of KDP is the anomalous dispersion it exhibits already around 1039 nm with a group velocity dispersion of $\beta_{2,\text{KDP}} = -7.5745\,\text{fs}^2\,\text{mm}^{-1}$ [66]. Dispersion compensation can therefore be achieved by simple propagation through a material of normal dispersion. The obvious choice in the multipass setup is the implementation of air for dispersion compensation. As the propagation length is fixed by the choice of the mirrors, the free parameter is the crystal thickness. The optimal combination is a crystal thickness of 3 mm and 22 passes in the multipass cell.

The simulation result is plotted in Fig. 4.6 in a similar manner to the result in Fig. 4.5. The temporal compression of the 220 fs input pulse (orange) down to an output pulse of 32.6 fs (blue) is shown in (a). This yields a compression factor of $\eta_{\text{KDP}} = 6.7$, exceeding the compression factors achieved by conventional fused silica multipass cells of $\eta_{\text{FS},1} = 5.8$, reported by Weitenberg *et al.* and $\eta_{\text{FS},2} = 5$, reported by Schulte *et al.* The spectral change in (b) enables a broadening of the incidental spectrum (orange) to a spectral range of over 200 nm (blue). Fig. 4.6(c) shows the evolution of the compression over the multiple passes. As the dispersion is in equilibrium in each pass, out-coupling could also be performed at a sooner stage. The same evolution in the spectral domain is presented in (d) over a logarithmic scale.

The simulation has shortcomings because the spatial domain is not considered. This could be improved by approximating the Gaussian beam waist in steps and simulating the behaviour in each step separately [91]. For a good match of theoretical predictions and future experimental results, the dispersion added by the scraper, incoupling mirrors and glass windows for beam incoupling need to be considered. The groundwork for a better estimation of the pulse shape by frequency-resolved gating was set up in this thesis. A follow-up thesis is aiming at an even more reliable pulse shape retrieval.

The peak power of the outgoing pulses in the proposed setup is significantly higher. Moreover, further compression is possible with a simpler setup. A consecutive multipass cell with fused silica and a chirped mirror pair can be set up. Consecutive multipass cell

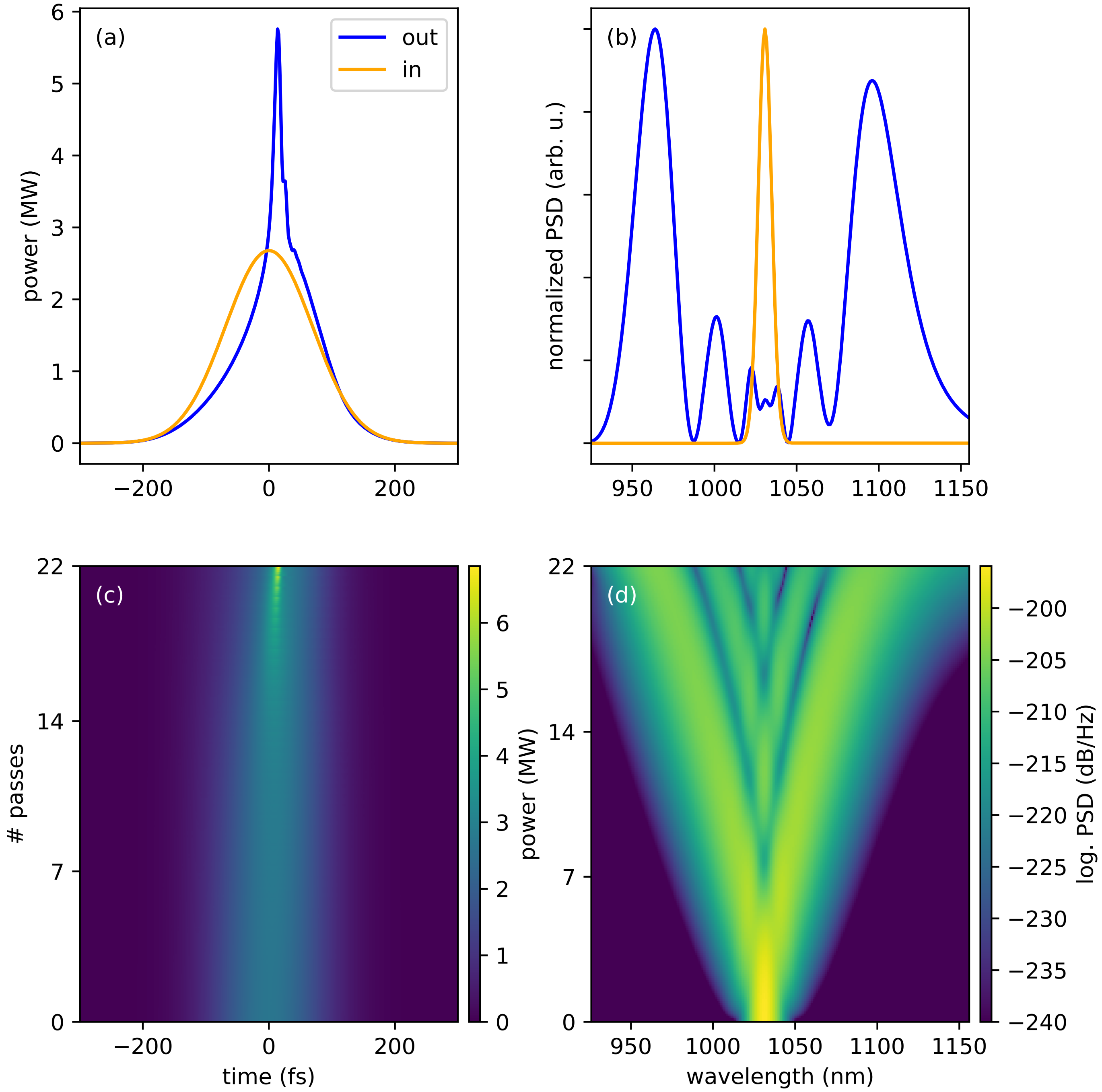

Figure 4.6: Simulation result of a multipass cell with 22 passes through 3 mm KDP, where the air compensates the dispersion of KDP. (a) The incoming pulse (orange) is shortened from 220 fs FWHM to 32.6 fs pulse length (blue). (b) The incoming Gaussian spectrum is broadened to over 200 nm bandwidth. (c) The continuous compression of the pulse over the number of passes, as dispersion is compensated in every step by propagation in air. (d) Spectral broadening over the number of passes plotted on a logarithmic power spectral density (PSD) colorscale.

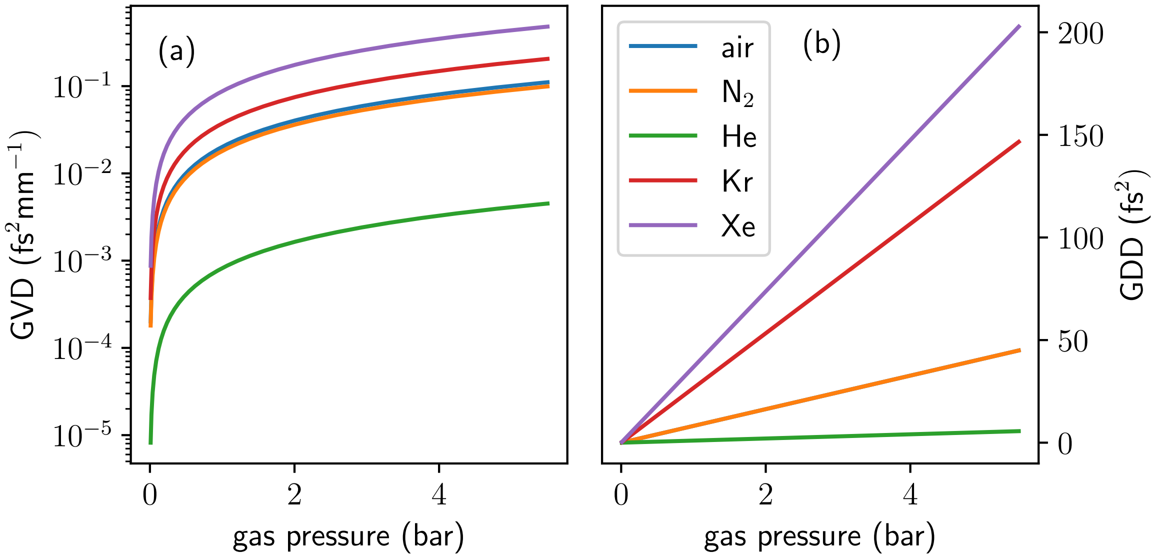

Figure 4.7: (a) Measured dispersion tuning of the group velocity dispersion of different gases by pressure adjustment from 0.01 bar to 5 bar around 800 nm. Data from [94]. (b) Adaption of this dispersion tuning to 1039 nm for the proposed multipass setup. The GDD is already calculated according to the dimensions of the setup for one pass in the cell. This enables dispersion compensation and fine-tuning by pressure adjustment. The lines for N_2 and air overlap. Data for air from [84], for N_2 from [95], for Xe, Kr from [94] and for He from [96].

arrangements deliver excellent compression results [29, 31]. The pulses recovered from the simulations exhibit a strong bottom pedestal which could be removed by implementation of a nonlinear polarization rotation stage. Such a setup has an intensity-dependent transmission, isolating the main pulse [92]. A drawback of this method may be the loss in pulse energy (39% loss reported by Seidel *et al.* [92]). To minimize spatial beam distortions, the performance could be further improved by splitting up the nonlinear crystal in two or more crystal plates in the center of the cell [93].

Further dispersion tunability is achievable by implementing a gas pressurized system. Dispersion tuning in gas-filled hollow-core photonic crystal fibers (HC-PCF) is already a well-known technique [69]. This is now adapted for a bulk multipass setup. As the dispersion of a gas scales linearly with pressure, fine tuning of the system can be realized by adjusting the pressure [94]. The principle behind this is shown in Fig. 4.7 where (a) shows measured pressure dependence of the dispersion at 800 nm. An adaption for the proposed length of 500 mm between two propagations in the nonlinear crystal and the available pressures in the cell that range from vacuum to 5.5 bar is depicted in Fig. 4.7(b).

Broad dispersion ranges from 0 to 200 fs^2 can be realized in this system. For a more sophisticated setup, gas mixtures can also be used.

In the bulk multipass setups presented to this date, the chirp removal is performed after the compression stage or with a combination of chirp removal in the cell and afterwards. The proposed setup is adaptive for different number of passes because the dispersion is compensated in every step. Furthermore, the maxima of the broadened spectrum (*cf.* Fig. 4.6) can be tuned to different wavelength ranges by adjusting the number of passes to access certain transitions. The compressed pulses with broader spectra are then sent into an enhancement cavity for XUV generation. Broader incoming spectra therefore yield broader XUV spectra. This is giving access to a wider range of transitions for frequency meteorology measurements on HCIs.

4.4 Mechanical Design of a Pressure Cell

Thus, a pressure cell was designed for this work to enable dispersion tuning by adjusting gas pressure. A further advantage of an enclosed system is reduction of accidental misalignment and long term stability. This is crucial for reliable operation of the enhancement cavity. In addition, KDP is a hygroscopic material and needs to be in a controlled atmosphere of reduced humidity.

The pressure cell is drawn in Fig. 4.8. All parts are made of stainless steel unless stated otherwise to ensure stability of the setup and to reduce vibrations and misalignment. The cell consists of a main clamp which is mounted on the optical table with six M6 screws. Two steel tubes of 130 mm diameter are mounted on the sides of the clamp. End flanges with o-rings are mounted on the ends of the steel tubes. The main clamp has a inner lining on the bottom for water cooling. Due to the high average power at which the system is operated, cooling is necessary as thermal expansion of the elements can lead to misalignment or even destruction of parts.

Two gas plugs can be used to pump and flush the cell with different gases. A high-pressure gas system is already set up in the XUV frequency comb laboratory, which simplifies operation with various gases. Two windows where the laser beam enters and exits the cell are mounted in the main clamp. Two further blind flanges are inserted for possible further adjustments and ports in the cell such as steering mechanisms or electronics.

Two maintenance windows are necessary to see through the cell in case of a malfunction. They are placed exactly over two mirrors in the cell. In this way, it is possible to see the whole cell without opening it. Monitoring of the system without having to open the

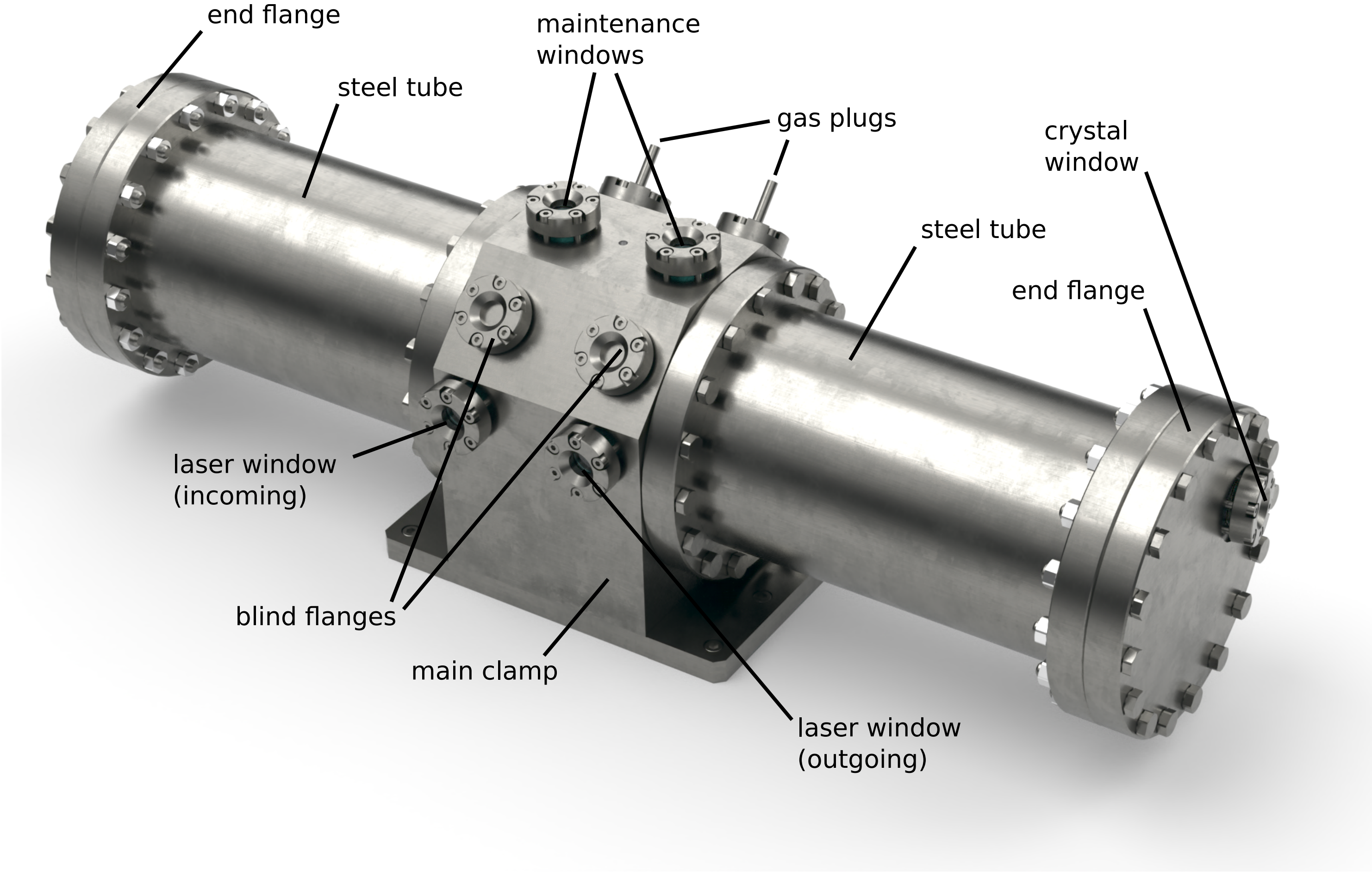

Figure 4.8: Pressure cell containing the multipass setup. The main clamp is mounted on the optical table and is the mount for the steel tubes. The tubes and end flanges enclose the pressure cell. The pressure can be adjusted with gas plugs. The laser beam is coupled into the cell by the laser windows. Additional windows for monitoring of the cell and blind flanges for future components are installed.

pressure cell is thus possible. The "crystal window" in one of the end flanges is a small fused silica flange placed at an angle to the central axis such that the nonlinear crystal in the cell center can be seen. Damage on the crystal is then directly visible.

With this setup, the *Druckgeräterichtlinie* allows a maximum operating pressure of 5.5 bar [97]. This enables a broad dispersion tuning range.

Fig. 4.9 shows the inside of the cell with the laser beam propagating through the cell. The laser beam enters the cell through a first 5 mm thick fused silica window. A first mirror with a diameter of 0.5" (adjustable via a side optic retention mount) guides the beam towards a first scraper mirror that couples the beam on the hyperboloid structure between the two curved mirrors. The beam reflection pattern in use has 22 passes between the mirrors and advances a total angle of 3π, as previously displayed in Fig. 4.2 and determined by the simulation result in Fig. 4.6. A second scraper mirror guides the beam onto the outcoupling mirror. The beam leaves the cell through a second fused silica window.

The nonlinear crystal is mounted on a copper holder. It is connected to a copper cooling plate which is mounted on the side of the main clamp. Heat from the crystal is then distributed over the whole setup and can be transported away by a pre-installed water cooling system in the bottom of the main clamp.

A more detailed view of the optical components is shown in Fig. 4.10 where the outer pressure cell components are suppressed for a better view of the optical setup. All optical components are mounted on a base plate of stainless steel. The plate has an u-shaped profile for enhanced stability. The base plate is screwed into the main clamp and fixed by guide rails.

The left side of Fig. 4.10 shows the incoupling process of the beam into the Herriott pattern in greater detail. The scraper mirror has a diameter of 6.35 mm. It is as small as possible to prevent clipping of the beam in further passes while still collecting the whole laser beam. The scraper is glued onto an aluminium adapter. The adapter is mounted into a 1/2" mirror mount for adjustment. The scraper is in front of the first curved mirror which is of 2" diameter and can be adjusted by a 2-axis mirror mount.

The mirror sits on a precision linear stage which allows lateral adjustment in a range of 6 mm. The stage itself can be mounted on the base plate at three different positions, expanding the movement range to 18 mm. The scraper for outcoupling of the beam sits on the right side of the curved mirror. It is adjustable in the same way as the scraper for the incoming beam by means of an adapter and a mirror mount.

Fig. 4.10 also allows a more detailed view of the copper crystal mount. The crystal

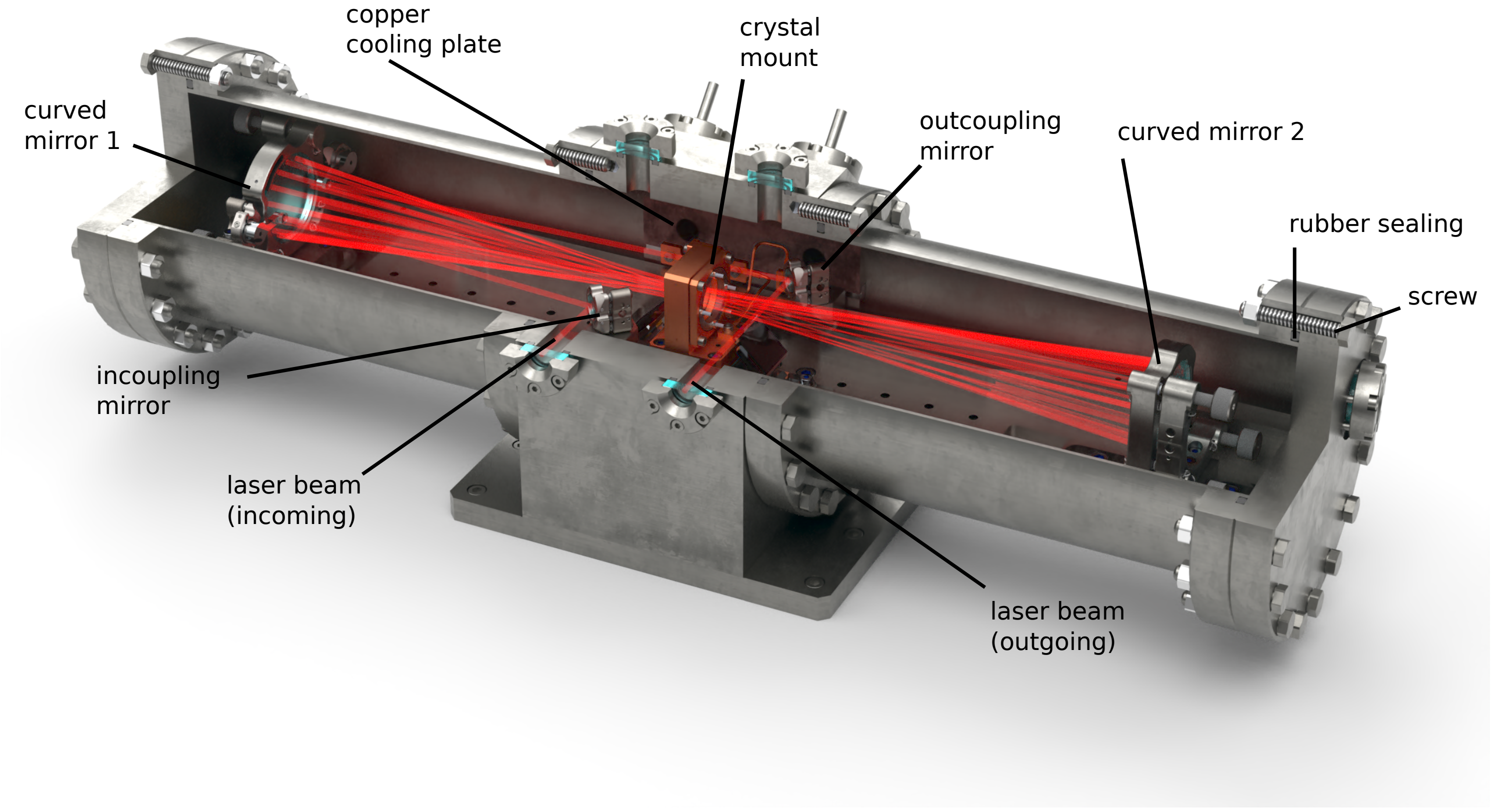

Figure 4.9: Cut through the pressure cell with visible beam path. The beam is coupled in via a mirror, advances between two curved mirrors through the crystal and is then coupled out. A copper cooling plate transfers heat from the crystal to the whole cell. The cut also shows the end flange mounting mechanism via rubber sealing and screws.

mount can be adapted to incorporate crystal material thicknesses from 1 mm to 4 mm as the cell is designed to offer an adaptable scheme of spectral broadening and thus, varying propagation lengths in the nonlinear material. The nonlinear crystal is mounted with an steel clamp for improved thermal stability in the outer crystal mount. The crystal end plate fixes the steel clamp in the outer holder. The screws of the crystal end plate are fixing copper strands onto the crystal mount. These strands guide the heat towards the cooling plate connection which is mounted into the copper cooling plate shown in Fig. 4.9.

The main crystal mount is bolted onto another linear precision stage with a movement range of 6 mm. The range is again extended to 18 mm as the stage can be mounted at different positions of the base plate. The second curved mirror is also mounted on a movable post, albeit not on a linear precision stage. Fine tuning of the setup is done with the linear precision stages of the other curved mirror and the crystal mount.

In front of the crystal mount is a maintenance mirror. It can be seen from above by looking into the maintenance window in Fig. 4.8. It lies at an angle of 45 degrees such that the second curved mirror is visible. The same arrangement is placed on the other side of the crystal mount to allow a view of all optical components in the multipass cell. The setup drawn in Fig. 4.8, Fig. 4.9 and Fig. 4.10 is currently being produced. The installed FROG system allows measurement of the pulse compression and spectral broadening that are planned with this system.

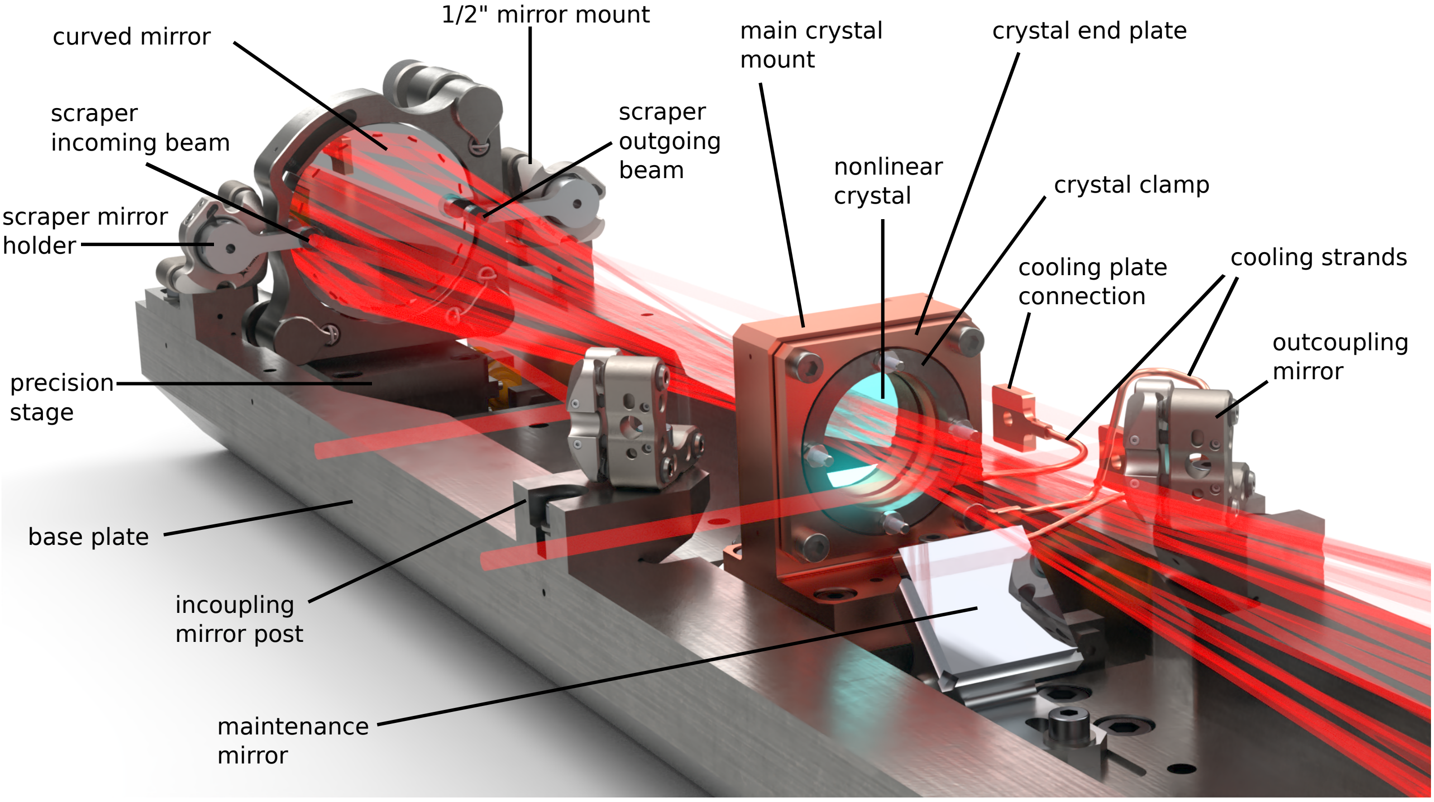

Figure 4.10: Inner part of the multipass cell. The optical components are mounted on a stainless steel base plate. Two scraper mirrors for coupling the beam in and out of the Herriott-type multipass are mounted on aluminium holders which can be adjusted via mirror mounts. The curved mirror and crystal mount are mounted on movable precision stages. The crystal is mounted in a copper mount which is thermalized by copper cooling strands. The maintenance mirror enables seeing the whole cell through the maintenance window in Fig. 4.8.

5 Conclusion

This work in the framework of a frequency comb in the XUV has presented a pulse characterization system for the driving pulses that generate the XUV light. Moreover, a novel design for temporal compression of these ultrashort laser pulses was developed.

The pulse characterization system implemented two versions of autocorrelation and the more advanced FROG. Intensity-based autocorrelation gave a first estimate of the pulse length of about 220 fs. The setup for intensity-based FROG allowed fast recording of traces, decreasing the recording time by a factor of over 20 compared to a previous setup. The optomechanical alignment possibilities of the setup, especially parallel alignment of the beams that generate the SHG signal, can be further improved for a more reliable pulse shape retrieval. This will be subject to a consecutive thesis.

Measurements with the setup for interferometric autocorrelation suggests that the pulse has a substantial amount of third-order dispersion of 120 fs^3. The agreement between a theoretically predicted trace and the experimental result is good. The interferometric FROG trace has a promising symmetry and is thus a good candidate for further evaluation by implementation of a retrieval algorithm that is able to retrieve pulse shapes from interferometric FROG traces, such as the COPRA algorithm. Continuous operation of the enhancement cavity with simultaneous measurement of the pulses without changing the optical setup is possible in this setup.

The design of a novel nonlinear pulse compression scheme in a multipass cell by spectral broadening with a KDP crystal with anomalous dispersion was presented in the second part of this thesis. The optical components of the multipass cell are incorporated in a newly designed pressure cell. Compensating the anomalous dispersion of KDP around the central wavelength of 1030 nm with normal dispersion of air or other gases with adjustable pressure in the cell enables a novel scheme for pulse compression. As each pass in the multipass cell is dispersion-compensated, the beam can be coupled out after an arbitrary number of passes. Pressure variation in the cell allows fine-tuning of the dispersion via gas pressure, eliminating the need for chirped mirrors or adjustment of optical components, which further enhances the flexibility of the setup. In this way, the pulse compression factor and the spectral range can be chosen with a certain freedom, which is—to the best of our knowledge—not possible with conventional multipass cell setups to this date. Numerical simulations support this proposal.

In this manner, the peak power can be increased and the pulse duration can be shortened while the spectral range can be increased. These pulses are then sent into enhancement cavities for XUV generation and velocity map imaging. Shorter pulses increase the efficiency of the XUV generation, therefore increasing the power of the generated harmonics. Moreover, shorter pulses with higher peak powers enable harmonics of higher order than produced in this setup to date because the cutoff energy is increased. The accompanying broader spectra, transferred from the nIR to the XUV, allow access to a wider range of transitions on HCIs and other transitions. Especially the broader range of the 7th harmonic is necessary for spectroscopy on thorium. This widens the application range of the XUV frequency comb for quantum logic spectroscopy on HCIs and paths the way to spectroscopy on the ^{229}Th isomer.

A Lists

A.1 List of Figures

A.2 List of Tables

B Acronyms

AC	Autocorrelation
BBO	Beta-Barium Borate
CM	Curved Mirror
CS	Caesium
COPRA	Common Pulse Retrieval Algorithm
EBIT	Electron Beam Ion Trap
FROG	Frequency-Resolved Optical Gating
FS	Fused Silica
FWHM	Full-Width at Half Maximum
GDD	Group Delay Dispersion
GVD	Group Velocity Dispersion
HC-PCF	Hollow Core Photonic Crystal Fiber
HCI	Highly Charged Ions
HHG	High harmonic generation
iAC	interferometric Autocorrelation
iFROG	interferometric Frequency-Resolved Optical Gating
KDP	Kaliumdiphosphat (Potassium Pyrophosphate)
LMA	Large Mode Area
nIR	near Infrared
PCF	Photonic Crystal Fiber
PCGPA	Principal Component Generalized Projects Algorithm
PSD	Power Spectral Density
TOD	Third Order Dispersion
VMI	Velocity Map Imaging
XUV	Extreme Ultraviolet Light
YAG	Yttrium aluminium garnet

C Bibliography

1. Tanabashi, M. *et al.* Review of particle physics. *Physical Review D* **98,** 030001 (2018).
2. Einstein, A. Die Feldgleichungen der Gravitation. *Sitzung der physikalisch-mathematischen Klasse* **25,** 844–847 (1915).
3. Uzan, J.-P. Varying constants, gravitation and cosmology. *Living reviews in relativity* **14,** 1–155 (2011).
4. Webb, J. *et al.* Indications of a spatial variation of the fine structure constant. *Physical Review Letters* **107,** 191101 (2011).
5. Dzuba, V. *et al.* Calculations of the relativistic effects in many-electron atoms and space-time variation of fundamental constants. *Physical Review A* **59,** 230 (1999).
6. Godun, R. *et al.* Frequency ratio of two optical clock transitions in Yb+ 171 and constraints on the time variation of fundamental constants. *Physical review letters* **113,** 210801 (2014).
7. Dijck, E. *Spectroscopy of Trapped 138Ba+ Ions for Atomic Parity Violation and Optical Clocks.* PhD thesis (University of Groningen, 2020).
8. Brewer, S. M. *et al.* Al+ 27 quantum-logic clock with a systematic uncertainty below 10- 18. *Physical review letters* **123,** 033201 (2019).
9. Kozlov, M. *et al.* Highly charged ions: Optical clocks and applications in fundamental physics. *Reviews of Modern Physics* **90,** 045005 (2018).
10. Levine, M. A. *et al.* The electron beam ion trap: A new instrument for atomic physics measurements. *Physica Scripta* **1988,** 157 (1988).
11. Schmöger, L. *et al.* Coulomb crystallization of highly charged ions. *Science* **347,** 1233–1236 (2015).
12. Stark, J. *et al.* An ultralow-noise superconducting radio-frequency ion trap for frequency metrology with highly charged ions. *arXiv preprint arXiv:2102.02793* (2021).

13. Micke, P. *et al.* Coherent laser spectroscopy of highly charged ions using quantum logic. *Nature* **578,** 60–65 (2020).
14. Einstein, A. Strahlungsemission und-absorption nach der Quantentheorie. *Verh. Deutsch. Phys. Gesell.* **18,** 318–323 (1916).
15. Schawlow, A. L. & Townes, C. H. Infrared and optical masers. *Physical Review* **112,** 1940 (1958).
16. Mairnan, T. Stimulated optical radiation in ruby. *Nature* **4736,** 493–494 (1960).
17. Sutter, D. H. *et al. High power and high energy ultrafast disk lasers for industrial applications* in *CLEO: Applications and Technology* (2019), JM3E–2.
18. Holzwarth, R. *et al.* Optical frequency synthesizer for precision spectroscopy. *Physical review letters* **85,** 2264 (2000).
19. Hänsch, T. W. Nobel lecture: passion for precision. *Reviews of Modern Physics* **78,** 1297 (2006).
20. McPherson, A. *et al.* Studies of multiphoton production of vacuum-ultraviolet radiation in the rare gases. *JOSA B* **4,** 595–601 (1987).
21. Gohle, C. *et al.* A frequency comb in the extreme ultraviolet. *Nature* **436,** 234–237 (2005).
22. Pupeza, I. *et al.* Compact high-repetition-rate source of coherent 100 eV radiation. *Nature Photonics* **7,** 608–612 (2013).
23. Carstens, H. *et al.* High-harmonic generation at 250 MHz with photon energies exceeding 100 eV. *Optica* **3,** 366–369 (2016).
24. Porat, G. *et al.* Phase-matched extreme-ultraviolet frequency-comb generation. *Nature Photonics* **12,** 387–391 (2018).
25. Nauta, J. *An extreme-ultraviolet frequency comb enabling frequency metrology with highly charged ions* PhD thesis (Ruprecht-Karls-Universität Heidelberg, 2020).
26. Nauta, J. *et al.* XUV frequency comb production with an astigmatism-compensated enhancement cavity. *Optics Express* **29,** 2624–2636 (2021).
27. Keldysh, L. *et al.* Ionization in the field of a strong electromagnetic wave. *Sov. Phys. JETP* **20,** 1307–1314 (1965).
28. Schulte, J. *et al.* Nonlinear pulse compression in a multi-pass cell. *Optics Letters* **41,** 4511–4514 (2016).

29. Fritsch, K. *et al.* All-solid-state multipass spectral broadening to sub-20 fs. *Optics letters* **43,** 4643–4646 (2018).

30. Weitenberg, J. *et al.* Nonlinear Pulse Compression to Sub-40 fs at 4.5 µJ Pulse Energy by Multi-Pass-Cell Spectral Broadening. *IEEE Journal of Quantum Electronics* **53,** 1–4 (2017).

31. Vicentini, E. *et al.* Nonlinear pulse compression to 22 fs at 15.6 μJ by an all-solid-state multipass approach. *Optics express* **28,** 4541–4549 (2020).

32. Eppink, A. T. & Parker, D. H. Velocity map imaging of ions and electrons using electrostatic lenses: Application in photoelectron and photofragment ion imaging of molecular oxygen. *Review of Scientific Instruments* **68,** 3477–3484 (1997).

33. Nauta, J. *et al.* 100 MHz frequency comb for low-intensity multi-photon studies: intra-cavity velocity-map imaging of xenon. *Optics letters* **45,** 2156–2159 (2020).

34. Seiferle, B. *et al.* Energy of the 229 Th nuclear clock transition. *Nature* **573,** 243–246 (2019).

35. Von der Wense, L. & Zhang, C. Concepts for direct frequency-comb spectroscopy of 229m Th and an internal-conversion-based solid-state nuclear clock. *The European Physical Journal D* **74,** 1–17 (2020).

36. Bilous, P. V. *et al.* Electronic Bridge Excitation in Highly Charged Th 229 Ions. *Physical Review Letters* **124,** 192502 (2020).

37. Maxwell, J. C. A Dynamical Theory of the Electromagnetic Field, Royal Society Transactions, Vol. *CLV, reprinted in Simpson, T., Maxwell* (1865).

38. Of Standards, N. I. & Technology. *speed of light in vacuum* `https://physics.nist.gov/cgi-bin/cuu/Value?c%7Csearch_for=universal_in!` (2021).

39. Diels, J.-C. & Rudolph, W. *Ultrashort laser pulse phenomena* (Elsevier, 2006).

40. Kobayashi, K. & Mito, I. Single frequency and tunable laser diodes. *Journal of Lightwave technology* **6,** 1623–1633 (1988).

41. Keller, U. *et al.* Semiconductor saturable absorber mirrors (SESAM's) for femtosecond to nanosecond pulse generation in solid-state lasers. *IEEE Journal of selected topics in QUANTUM ELECTRONICS* **2,** 435–453 (1996).

42. Salhi, M. *et al.* Theoretical study of the erbium-doped fiber laser passively mode-locked by nonlinear polarization rotation. *Physical Review A* **67,** 013802 (2003).

43. Cundiff, S. T. Phase stabilization of ultrashort optical pulses. *Journal of Physics D: Applied Physics* **35,** R43 (2002).
44. Nussenzveig, H. M. The theory of the rainbow. *Scientific American* **236,** 116–128 (1977).
45. Sellmeier, W. Zur Erklaerung der abnormen Farbenfolge im Spectrum einiger Substanzen. *Annalen der Physik und Chemie* **219,** 272–282 (1871).
46. Eimerl, D. Electro-optic, linear, and nonlinear optical properties of KDP and its isomorphs. *Ferroelectrics* **72,** 95–139 (1987).
47. Saleh, B. E. & Teich, M. C. *Fundamentals of photonics* (John Wiley & Sons, 2019).
48. Kabaciński, P. *et al.* Nonlinear refractive index measurement by SPM-induced phase regression. *Optics express* **27,** 11018–11028 (2019).
49. Chen, C.-M. & Kelley, P. L. Nonlinear pulse compression in optical fibers: scaling laws and numerical analysis. *JOSA B* **19,** 1961–1967 (2002).
50. Stolen, R. H. & Lin, C. Self-phase-modulation in silica optical fibers. *Physical Review A* **17,** 1448 (1978).
51. Agrawal, G. P. *Nonlinear fiber optics* (Springer, 2000).
52. Lewenstein, M. *et al.* Theory of high-harmonic generation by low-frequency laser fields. *Physical Review A* **49,** 2117 (1994).
53. Ishikawa, K. L. High-harmonic generation. *Advances in Solid State Lasers Development and Applications,* 439–465 (2010).
54. Trebino, R. *et al.* Highly reliable measurement of ultrashort laser pulses. *Journal of Applied Physics* **128,** 171103 (2020).
55. Yang, W. *et al.* Spectral phase retrieval from interferometric autocorrelation by a combination of graduated optimization and genetic algorithms. *Optics express* **18,** 15028–15038 (2010).
56. Trebino, R. & Kane, D. J. Using phase retrieval to measure the intensity and phase of ultrashort pulses: frequency-resolved optical gating. *JOSA A* **10,** 1101–1111 (1993).
57. Strickland, D. & Mourou, G. Compression of amplified chirped optical pulses. *Optics communications* **55,** 447–449 (1985).
58. Saraceno, C. J. *et al.* The amazing progress of high-power ultrafast thin-disk lasers. *Journal of the European Optical Society-Rapid Publications* **15,** 1–7 (2019).

59. Negel, J.-P. *et al.* 1.1 kW average output power from a thin-disk multipass amplifier for ultrashort laser pulses. *Optics letters* **38,** 5442–5445 (2013).

60. Kovács, A. *et al.* Dispersion control of a pulse stretcher–compressor system with two-dimensional spectral interferometry. *Applied Physics B* **80,** 165–170 (2005).

61. Lai, M. *et al.* Single-grating laser pulse stretcher and compressor. *Applied optics* **33,** 6985–6987 (1994).

62. Kane, S. & Squier, J. Grism-pair stretcher–compressor system for simultaneous second-and third-order dispersion compensation in chirped-pulse amplification. *JOSA B* **14,** 661–665 (1997).

63. Ackermann, A. *Modellierung und Charakterisierung eines Kompressors für ultrakurze Laserpulse durch Strahlenverfolgung* (2017).

64. Malitson, I. H. Interspecimen comparison of the refractive index of fused silica. *Josa* **55,** 1205–1209 (1965).

65. Zelmon, D. E. *et al.* Refractive-index measurements of undoped yttrium aluminum garnet from 0.4 to 5.0 μm. *Applied optics* **37,** 4933–4935 (1998).

66. Zernike, F. Refractive Indices of Ammonium Dihydrogen Phosphate and Potassium Dihydrogen Phosphate between 2000 Å and 1.5 μ. *J. Opt. Soc. Am.* **54,** 1215–1220. `http://www.osapublishing.org/abstract.cfm?URI=josa-54-10-1215` (Oct. 1964).

67. Südmeyer, T. *et al.* Nonlinear femtosecond pulse compression at high average power levels by use of a large-mode-area holey fiber. *Optics letters* **28,** 1951–1953 (2003).

68. Heckl, O. *et al.* Temporal pulse compression in a xenon-filled Kagome-type hollow-core photonic crystal fiber at high average power. *Optics express* **19,** 19142–19149 (2011).

69. Travers, J. C. *et al.* Ultrafast nonlinear optics in gas-filled hollow-core photonic crystal fibers. *JOSA B* **28,** A11–A26 (2011).

70. Sennaroglu, A. & Fujimoto, J. G. Design criteria for Herriott-type multi-pass cavities for ultrashort pulse lasers. *Optics Express* **11,** 1106–1113 (2003).

71. Szipöcs, R. *et al.* Chirped multilayer coatings for broadband dispersion control in femtosecond lasers. *Optics letters* **19,** 201–203 (1994).

72. Siegman, A. E. *Lasers* (University Science Books, 1986).

73. Keliher, P. N. & Wohlers, C. C. Echelle grating spectrometers in analytical spectrometry. *Analytical Chemistry* **48,** 333A–340a (1976).

74. Jafari, R. *et al.* 100% reliable algorithm for second-harmonic-generation frequency-resolved optical gating. *Optics express* **27,** 2112–2124 (2019).

75. Ackermann, A. *Development and characterization of a femtosecond pulse compressor* (2019).

76. Kleinert, S. *pyfrog* `https://github.com/svenkleinert/pyfrog` (2021).

77. Kane, D. J. Recent progress toward real-time measurement of ultrashort laser pulses. *IEEE Journal of Quantum Electronics* **35,** 421–431 (1999).

78. Stibenz, G. & Steinmeyer, G. Interferometric frequency-resolved optical gating. *Optics express* **13,** 2617–2626 (2005).

79. Geib, N. C. *et al.* Common pulse retrieval algorithm: a fast and universal method to retrieve ultrashort pulses. *Optica* **6,** 495–505 (2019).

80. Gérôme, F. *et al.* Simplified hollow-core photonic crystal fiber. *Optics letters* **35,** 1157–1159 (2010).

81. Emaury, F. *et al.* Efficient spectral broadening in the 100-W average power regime using gas-filled kagome HC-PCF and pulse compression. *Optics Letters* **39,** 6843–6846 (2014).

82. Genty, G. *et al.* Supercontinuum generation in large mode-area microstructured fibers. *Optics Express* **13,** 8625–8633 (2005).

83. Lodewyck, J. *GaussianBeam* `https://sourceforge.net/projects/gaussianbeam/` (2021).

84. Ciddor, P. E. Refractive index of air: new equations for the visible and near infrared. *Applied optics* **35,** 1566–1573 (1996).

85. Zahedpour, S. *et al.* Measurement of the nonlinear refractive index of air constituents at mid-infrared wavelengths. *Optics letters* **40,** 5794–5797 (2015).

86. Mahnke, C. *gnlse: a python script to simulate the propagation of pulses in optical fibers* `https://github.com/xmhk/gnlse` (2021).

87. Nobre, F. *et al.* A generalized nonlinear Schroedinger equation: Classical field-theoretic approach. *EPL (Europhysics Letters)* **97,** 41001 (2012).

88. Dudley, J. M. & Taylor, J. R. *Supercontinuum generation in optical fibers* (Cambridge University Press, 2010).

89. Fibich, G. & Gaeta, A. L. Critical power for self-focusing in bulk media and in hollow waveguides. *Optics letters* **25,** 335–337 (2000).

90. Ganeev, R. *et al.* Characterization of nonlinear optical parameters of KDP, LiNbO3 and BBO crystals. *Optics communications* **229,** 403–412 (2004).

91. Mei, C. & Steinmeyer, G. Space-time focusing and coherence properties of supercontinua in multipass cells. *Physical Review Research* **3,** 013259 (2021).

92. Seidel, M. *et al.* Ultrafast MHz-rate burst-mode pump-probe laser for the FLASH FEL facility based on nonlinear compression of ps-level pulses from an Yb-amplifier chain. *arXiv preprint arXiv:2105.05882* (2021).

93. Beetar, J. E. *et al.* Spectral broadening and pulse compression of a 400 μ J, 20 W Yb: KGW laser using a multi-plate medium. *Applied Physics Letters* **112,** 051102 (2018).

94. Börzsönyi, A. *et al.* Dispersion measurement of inert gases and gas mixtures at 800 nm. *Applied optics* **47,** 4856–4863 (2008).

95. Peck, E. R. & Khanna, B. N. Dispersion of Nitrogen$*$. *J. Opt. Soc. Am.* **56,** 1059–1063. `http://www.osapublishing.org/abstract.cfm?URI=josa-56-8-1059` (Aug. 1966).

96. Mansfield, C. R. & Peck, E. R. Dispersion of helium. *JOSA* **59,** 199–204 (1969).

97. McBain, G. A user's view of the pressure equipment directive. *Measurement and Control* **36,** 300–304 (2003).

D Acknowledgements

It was a real pleasure to conduct my thesis at the Max-Planck-Institute. I learned a lot—and would like to thank all the people who made this a wonderful time.
José, thank you for the possibility to do this thesis in your group. I greatly enjoyed the atmosphere that you create in the whole EBIT-group. Your insights on how to set up something new was very helpful.
Herzlichen Dank an Thomas Pfeifer für die Übernahme der Zweitbetreuung und das gute Arbeitsumfeld am MPI.
Ein ganz dickes Dankeschön geht an Jan-Hendrik. Du hast dir einfach super viel Mühe für mich gegeben - und deine Begeisterung für Laser und vor allem *Sachen bauen* ist mit der Zeit echt ansteckend geworden. Tobias, von dir habe ich sehr viel gelernt und deine analytische Herangehensweise an Probleme ist ganz faszinierend. Ihr wart super!
Für die schöne Arbeitsatmosphäre möchte ich mich auch ganz herzlich beim Rest des XUV-Teams, der ganzen EBIT-Gruppe und beim Studentenbüro bedanken, insbesondere bei Nele und Christian für die Korrekturen. Ganz speziell bei Claudia für die seelischen Streicheleinheiten in den dunklen Corona-Zeiten.
Bei allen Mitarbeitern des MPIK, mit denen ich zusammenarbeiten durfte, möchte ich mich ebenfalls bedanken. Von der Erfahrung vieler Seiten, sei es Konstruktion, Fertigung oder Elektronik, habe ich sehr profitiert. Insbesondere möchte ich Yannick Steinhauser für die Zusammenarbeit und das Erstellen der SolidWorks-Abbildungen in dieser Arbeit danken.
Danke an Julius, Josef, Jan und Tobi für das schnelle und gründliche Korrekturlesen und die tollen Jahre, die ich mit euch im schönen Heidelberg genießen durfte.
Schließlich möchte ich meinen Eltern und Schwestern für einfach alles danken. Ohne euch hätte ich es nicht bis zu diesem Abschluss geschafft. Dange!

E Deposition

Erklärung:

Ich versichere, dass ich diese Arbeit selbstständig verfasst habe und keine anderen als die angegebenen Quellen und Hilfsmittel benutzt habe.

Heidelberg, den 31.10.2021 ....